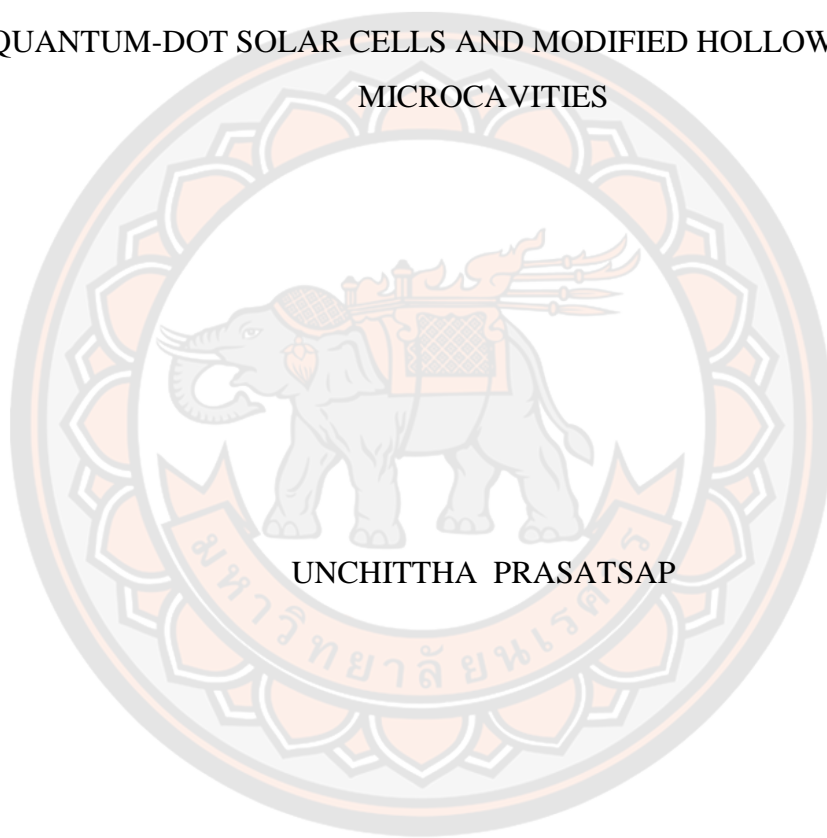




ELECTRICAL CHARACTERIZATIONS AND CIRCUIT MODELS OF HYBRID
QUANTUM-DOT SOLAR CELLS AND MODIFIED HOLLOW OPTICAL
MICROCAVITIES



UNCHITTHA PRASATSAP

A Thesis Submitted to the Graduate School of Naresuan University
in Partial Fulfillment of the Requirements
for the Doctor of Philosophy in (Electrical Engineering)

2021

Copyright by Naresuan University

ELECTRICAL CHARACTERIZATIONS AND CIRCUIT MODELS OF HYBRID
QUANTUM-DOT SOLAR CELLS AND MODIFIED HOLLOW OPTICAL
MICROCAVITIES



A Thesis Submitted to the Graduate School of Naresuan University
in Partial Fulfillment of the Requirements
for the Doctor of Philosophy in (Electrical Engineering)
2021

Copyright by Naresuan University

Thesis entitled "ELECTRICAL CHARACTERIZATIONS AND CIRCUIT MODELS
OF HYBRID QUANTUM-DOT SOLAR CELLS AND MODIFIED HOLLOW
OPTICAL MICROCAVITIES"

By UNCHITTHA PRASATSAP

has been approved by the Graduate School as partial fulfillment of the requirements
for the Doctor of Philosophy in Electrical Engineering of Naresuan University

Oral Defense Committee

..... Chair
(Professor Somsak Panyakeow, Ph.D.)

..... Advisor
(Associate Professor Thawatchai Mayteevarunyoo, Ph.D.)

..... Co Advisor
(Associate Professor Suwit Kiravittaya, Ph.D.)

..... Co Advisor
(Associate Professor Theerachai Bongkarn, Ph.D.)

..... Internal Examiner
(Associate Professor Panus Nattharith, Ph.D.)

Approved

.....
(Associate Professor Krongkarn Chootip, Ph.D.)

Dean of the Graduate School

Title	ELECTRICAL CHARACTERIZATIONS AND CIRCUIT MODELS OF HYBRID QUANTUM-DOT SOLAR CELLS AND MODIFIED HOLLOW OPTICAL MICROCAVITIES
Author	UNCHITTHA PRASATSAP
Advisor	Associate Professor Thawatchai Mayteevarunyoo, Ph.D.
Co-Advisor	Associate Professor Suwit Kiravittaya, Ph.D.
Academic Paper	Associate Professor Theerachai Bongkarn, Ph.D. Ph.D. Dissertation in Electrical Engineering, Naresuan University, 2021
Keywords	Quantum-dot solar cell, DC and AC characteristics, Equivalent circuit model, Whispering gallery modes, Optical microcavities

ABSTRACT

This thesis studies two photonic structures and aims to apply theirs in enhancing the solar cell performance. They are quantum-dot (QD) structure and optical microcavity. The first interesting photonic structure is studied for enhancing the efficiency of the hybrid QD solar cells by the increase of stacked hybrid QD layers and the differently stacking QD sequence. We investigate both DC and AC circuit parameters. The DC circuit parameters are extracted from the fitting of current-voltage characteristics. The parameters are the reverse saturation current, the diode ideality factor, the photocurrent, the series resistance and the shunt resistance. From the analysis, the short-circuit current is always approximate to the photocurrent. The ideality factor of 2 indicates the dominant recombination current within solar cells.

The first experimentation is studied for the increase of stacking hybrid GaSb/GaAs and InAs/GaAs layers (type-A). The increase of photocurrent is observed when the stacked hybrid QD layers increases. In addition, the open-circuit voltage of 3-pairs hybrid QD solar cell also increases. The series resistance increases and the shunt resistance decreases. The solar cell efficiency and the fill factor of the 1-pair of type-A QD sample are higher than those of the 3-pairs sample because increase of stacking layers increase the total layer thickness. The reverse saturation current and

the photocurrent of 3-pairs hybrid QD sample has the less values than those of 1-pair sample. The second experimentation is the study of the different stacking hybrid QD sequence. The DC circuit parameters of two types (type-A and type-B) hybrid QD solar cells are investigated. The reverse saturation current and the photocurrent of the sample with correct stacking sequence have higher values. The correct stacking sequence of hybrid InAs/GaAs and GaSb/GaAs QD (type-B) can result in a better solar cell performance.

AC circuit parameters of hybrid QD solar cells are also studied. They are extracted by fitting the frequency response under the controlled bias condition at maximum power point. The diode capacitance, the diode resistance, the AC series resistance and the AC shunt resistance are obtained. The increase of stacking type-A QD layers (3-pairs) results in higher values of the capacitance and the diode resistance because of the high number density of the buried QDs. Moreover, the increase of stacking layers affects other parameters and the increase of stacking layers is more sensitive with the AC signal.

The second investigated photonic structure is the hollow optical whispering-gallery-mode (WGM) type microcavities. This work focuses on the modified characteristics of hollow optical microcavities by using finite-difference time-domain simulation and photoluminescence (PL) measurement. Designed structure of periodic hole array (hollow cylindrical microcavities) and hollow hyperboloidal microcavities are presented. Structural parameters of the hollow cylinder microcavity are varied. Electric and magnetic field profiles and enhanced resonant modes are presented. The quality factor variation as a function of mode index relates with spatial field mode pattern and the hole array. The resonant frequency depends on both hole radius and waveguide width. The resonant frequency blueshifts with the increasing radius and the reducing width. For the hyperboloidal microcavities, the new shape, which is also called anti-bottle resonator, is designed and fabricated. We present the experimental observation of the resonant modes by PL measurement. Range of effective refractive index approximates 1.15-1.35. Rather low Q factors of about 250-445 of the modes at wavelength range of 530-570 nm are achieved.

ACKNOWLEDGEMENTS

This thesis was successfully accomplished because of the support from people and organizations involved in this research. I would like to thank them very much for this achievement.

I could not have studied in the doctor of philosophy (electrical engineering) without supports and opportunity from the Royal Golden Jubilee (RGJ) Ph.D. program (PHD/0078/2561) and Assoc. Prof. Dr. Suwit Kiravittaya. I am grateful and glad to be a part of the RGJ. Ph.D. program. This program supports scholarship and gives the opportunity to do research at Fudan University under the supervision of Prof. Dr. Yongfeng Mei. I am deeply thankful to Assoc. Prof. Dr. Suwit Kiravittaya. He devotes his valuable time to provide knowledge, assistance and advice in all aspects throughout the period of my Ph.D. program. I am deeply thankful to Prof. Dr. Yongfeng Mei for the supports, experience, wide world view and knowledge throughout the period of my research in Nanomembrane group at Fudan University.

Later, due to the Covid-19 pandemic, I returned to Thailand to conduct research. Meanwhile, Assoc. Prof. Dr. Suwit Kiravittaya has transferred to Chulalongkorn University as a lecturer. In the next management of the RGJ Ph.D. program (PHD/0078/2561), Assoc. Prof. Dr. Thawatchai Mayteevarunyoo will be the new adviser. Dr. Thawatchai's research project, titled "Three-wave Airy waves and solitons in two dimensions," is about Soliton, and I'll be working on it. This research will be conducted in collaboration with Prof. Boris Malomed from Tel Aviv University. I am deeply thankful to Assoc. Prof. Dr. Thawatchai Mayteevarunyoo for knowledge and advice throughout the period of Thawatchai's research project. I am thankful to Prof. Dr. Boris A. Malomed for the advice and knowledge of research with Tel Aviv University.

I am thankful to Assoc. Prof. Dr. Theerachai Bongkarn (co – advisor) for advice and help.

I thank many people who have participated in my research at the Advanced Optical Technology (AOT) laboratory. I thank department of Electrical and Computer Engineering at Naresuan University for support experimental equipment and computers from AOT Lab, EE509 room and EE graduate student office room.

I thank cooperation from Dr. Zon and members in the Semiconductor Device Research Laboratory (SDRL), Department of Electrical Engineering at Chulalongkorn University under the supervision of Prof. Dr. Somsak Panyakeow, Assoc. Prof. Dr. Suwit Kiravittaya and Mr. Supachok Thainoi.

I thank Fudan scholarship and all members of Nanomembrane Group, Department of Materials Science, Fudan University, Shanghai, Republic of China under the supervision of Prof. Dr. Yongfeng Mei and Prof. Dr. Gaoshan Huang. The supports, good experience, good friendship and knowledge from Chunyu You, Kaibo Wu, Shuo Yang, Ye Kong, Yimeng Chen, Yang Wang, Prof. Dr. Gaoshan Huang and Prof. Dr. Yongfeng Mei throughout the period of my research in Nanomembrane group at Fudan University are acknowledged.

I thank cooperation and support from Thailand Science Research and Innovation (TSRI), National Research Council of Thailand (NRCT), National Metal and Materials Technology Center (MTEC), Thai Microelectronics Center (TMEC), National Science and Technology Development Agency (NSTDA), NANOTEC, National Electronics and Computer Technology Center (NECTEC), International School of Engineering (ISE), Faculty of Engineering, Chulalongkorn university and Research Center for Academic Excellent in Applied Physics of Naresuan university.

Above all, I deeply thank my mother and my older brother for love and encouragement. Finally, I thank myself for endeavor and determination to overcome all problems. The value and benefits of this thesis would be dedicated to all the benefactors and people, who are interested. I hope that this research will be useful for both academics and practitioners.

UNCHITTHA PRASATSAP

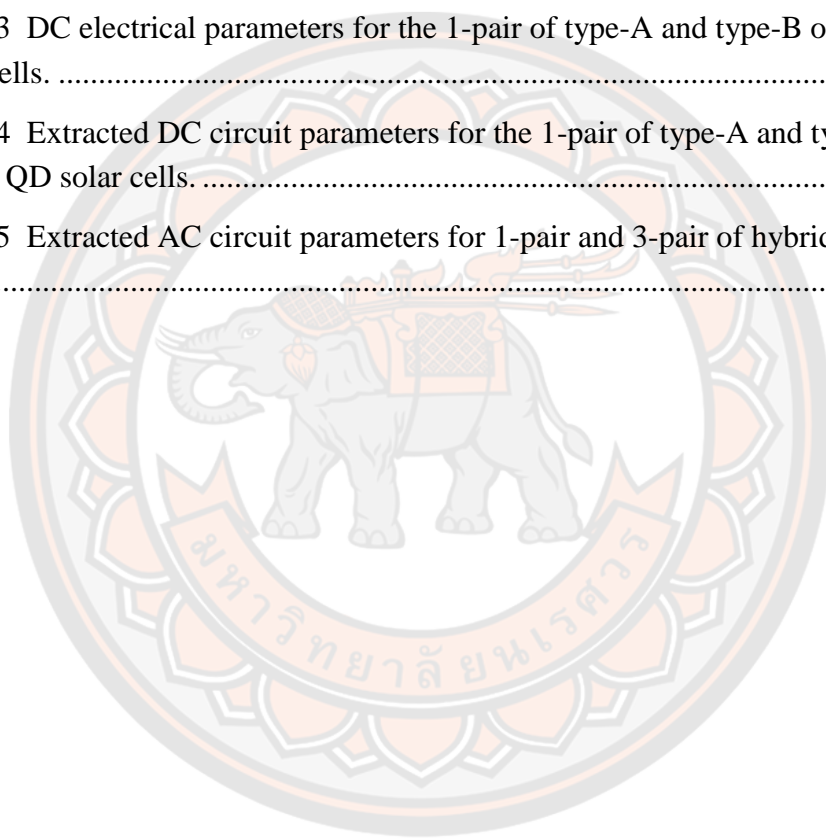
TABLE OF CONTENTS

	Page
ABSTRACT.....	C
ACKNOWLEDGEMENTS.....	E
TABLE OF CONTENTS.....	G
LIST OF TABLES.....	I
LIST OF FIGURE.....	J
CHAPTER I INTRODUCTION.....	1
1.1 Background and Significance of the Study	1
1.2 Purposes of the Study	3
1.3 Scope of the Study	4
1.4 Hypotheses of the Study	4
1.5 Expected Benefits	5
CHAPTER II THEORY AND LITERATURE REVIEW.....	6
2.1 Solar Cells.....	6
2.2 Hybrid Quantum-Dot Solar Cells	9
2.3 The Equivalent Circuit Model of Solar Cell.....	10
2.3.1 DC Equivalent Circuit Model.....	10
2.3.2 AC Equivalent Circuit Model.....	13
2.4 DC Characteristic: Current - Voltage Characteristic	16
2.5 AC Characteristics: Frequency Response.....	16
2.6 Type of Optical Microcavities	19
2.7 Fabrication Technique of Optical Microcavities	23
2.8 Characterization of Optical Microcavities.....	25
CHAPTER III RESEARCH PROCEDURES OF THE STUDY	29
3.1 Structure of Hybrid InAs/GaAs and GaSb/GaAs Quantum-Dot Solar Cells	29
3.2 Sample Characterization.....	32

3.2.1 Current - Voltage Characteristics	32
3.2.2 Frequency responses.....	35
3.3 Method for Optimal DC and AC Parameter Extraction	36
3.3.1 Extracted Method for the DC Circuit Parameters	37
3.3.2 Extracted Method for the AC Circuit Parameters	39
3.4 Hollow Optical Microcavities.....	42
3.4.1 Structure of hollow optical microcavities	42
3.4.2 Finite-difference time-domain (FDTD) simulation.....	45
3.4.3 Fabrication of hollow microcavity by the photonic professional GT DLW system.....	47
CHAPTER IV RESULT AND DISCUSSION.....	52
4.1 DC Circuit Parameters of Type-A and Type-B Hybrid QD Solar Cells	52
4.1.1 Result and discussion of DC Circuit Parameters between 1-Pair and 3-pair of Type-A Hybrid QD Solar Cells	53
4.1.2 Result and discussion of DC Circuit Parameters between Type-A and Type-B Hybrid QD Solar Cells	56
4.2 Result and discussion of AC Circuit Parameters between 1-Pair and 3-pair type-A hybrid QD solar cells	59
4.3 Whispering-gallery mode and optical characteristics of hollow optical microcavities.....	63
4.3.1 Result and discussion about the resonant mode fields of hollow cylindrical optical microcavities by using FDTD simulation	63
4.3.2 Result and discussion about WGM of hollow cylindrical microcavities at various structural parameters.....	66
4.3.3 Result and discussion about an optical microcavity of hollow hyperboloidal microcavities	71
CHAPTER V CONCLUSION.....	73
REFERENCES	76
BIOGRAPHY	84

LIST OF TABLES

	Page
Table 1 DC electrical parameters for the 1-pair and 3-pair of type-A hybrid QD solar cells.	53
Table 2 Extracted DC circuit parameters for the 1-pair and 3-pair of type-A hybrid QD solar cells.....	55
Table 3 DC electrical parameters for the 1-pair of type-A and type-B of hybrid QD solar cells.	56
Table 4 Extracted DC circuit parameters for the 1-pair of type-A and type-B of hybrid QD solar cells.	59
Table 5 Extracted AC circuit parameters for 1-pair and 3-pair of hybrid QD solar cells.	62



LIST OF FIGURE

	Page
Figure 1 Diagram showing the 3 main generations of solar cells.....	6
Figure 2 (a) polycrystalline and (b) monocrystalline Si solar cells (6).....	7
Figure 3 The component diagram of MBE	9
Figure 4 Carrier Injection from InAs/GaAs QDs to GaSb/GaAs QDs (26)	10
Figure 5 Ideal equivalent circuit model	11
Figure 6 Series resistance circuit model	12
Figure 7 Shunt resistance circuit model	13
Figure 8 The series and shunt resistance circuit model	13
Figure 9 The simplified AC equivalent circuit model of a solar cell (35).....	14
Figure 10 The AC equivalent circuit model of a QD sensitized solar cell is proposed by Gonzalez-Pedro et al. (36).....	15
Figure 11 The AC equivalent circuit model of nanoPS and silver nanoparticles in solar cells is presented (40).....	15
Figure 12 (a) The DC current-voltage characteristics of a hybrid QD solar cell are measured and fitted. As well as (b) fitness values are obtained from fitting the curves with different DC circuit models.	16
Figure 13 Measurement setup of impedance spectroscopy in frequency domain (35).....	17
Figure 14 Measurement setup of open circuit voltage decay technique in the time domain (37).....	18
Figure 15 Measurement setup of the capacitance measuring by using triangular wave technique (38).....	19
Figure 16 The scanning electron micrograph (SEM) of on-chip spherical chalcogenide microcavity array (42)	20
Figure 17 The SEM photograph of a toroid microcavity (44).....	21
Figure 18 The structure of a single WGM tubular microcavity showing a periodic hole array (73).....	22

Figure 19 structure and optical characteristics of (a) optical bottle microcavity, (b) acoustic bottle microcavity, and (c) acoustic anti-bottle microcavity (50).....	22
Figure 20 Schematic of the fabrication sets up by using a CO ₂ laser. (53)	23
Figure 21 (a) structural diagram of fabricating process for rolled-up SiO/SiO ₂ tubular microcavity and (b) SEM photograph of tubular microcavity arrays (46).....	24
Figure 22 The SEM photograph of the hourglass-shaped silicon microcavity arrays (54).....	25
Figure 23 Transmission spectra at different axial positions obtain from (a) experimental measurement and (b) FDTD simulation (48).....	26
Figure 24 Schematic of the micro-PL setup (56).....	27
Figure 25 PL spectrum at 8 K of a single SiO _x /Si microtube cavities (57)	28
Figure 26 (a) Schematic and (b) photo of type-A hybrid QD solar cell sample having 1-pair of stacked GaSb/GaAs QD and InAs/GaAs QD layers.....	30
Figure 27 (a) Schematic and (b) photo of type-A hybrid QD solar cell sample having 3 pairs of stacked GaSb/GaAs QD and InAs/GaAs QD layers.	31
Figure 28 (a) Schematic and (b) photo of type-B hybrid QD solar cell sample having 1 pair of InAs/GaAs QD and GaSb/GaAs QD layers.....	32
Figure 29 Experimental setup	33
Figure 30 Measurement circuit of obtaining current - voltage characteristic and the DC equivalent circuit model of hybrid QD solar cell.....	34
Figure 31 Measurement circuit for extracting frequency response and AC equivalent circuit model of hybrid QD solar cell.	36
Figure 32 Diagram showing the procedure for the DC circuit parameter extraction.	37
Figure 33 Diagram showing the procedure for the AC circuit parameter extraction.	40
Figure 34 (a) The 3D structure and (b) the simplified 2D structure of the investigated hollow cylindrical optical microcavity.	43
Figure 35 (a) The 3D structure and (b) the microscope photo of the hollow symmetrical hyperboloid microcavity.	44
Figure 36 Simulation domain for low Q modes. The H _z dipole source and monitoring point are marked as a cross.	45
Figure 37 The photonic professional GT DLW system.....	47

Figure 38 Application of IP-L 780 photoresist.....	47
Figure 39 Oil immersion configuration (69).....	48
Figure 40 The device is inside the 3D printer electronics rack.....	48
Figure 41 The microscope displays lower z-limit reached.	49
Figure 42 The curve of intensity-pixel index represents in display of the interface finder.....	50
Figure 43 User interface of NanoWrite after the printing process started operation.	51
Figure 44 Sample development process includes (a) washing out the residues of the written structure and (b) removing the developer.....	51
Figure 45 Current-voltage characteristic curves of 1-pair and 3-pair type-A hybrid QD samples.....	54
Figure 46 Current-voltage characteristic curves for the 1-pair of type-A and type-B of hybrid QD solar cells.....	57
Figure 47 Waveforms of input and output voltage signals obtain from the oscilloscope at $f = 500$ kHz. The full and dashed lines are the fitted results.....	60
Figure 48 Frequency responses for 1-pair and 3-pair of hybrid QD solar cells biased at maximum power points (marked in Figure 45).	61
Figure 49 The magnetic field profiles H_z of resonant modes are extracted at $m =$ (a) 19, (b) 20, and (c) 21 in simulation domain for low Q factor.....	64
Figure 50 (a) The magnetic field profile H_z , (b) the electric field profiles E_x and (c) E_y are extracted at $m=20$ in simulation domain for single high Q factor.	65
Figure 51 (a) the electric and (b) magnetic field energy density profiles are extracted at $m=20$ in simulation domain for single high Q factor.....	66
Figure 52 Variations of resonant frequency f_c and Q factor as a function of hole radius r	67
Figure 53 Variations of resonant frequency f_c and Q factor as a function of missing hole width w	69
Figure 54 Variations of resonant frequency f_c and Q factor as a function of hole numbers along columns N	70
Figure 55 Variations of resonant frequency f_c and Q factor as a function of hole numbers along rows M	71

Figure 56 PL spectra of (a) the hyperboloidal microcavity sample and (b) the sample with some structural imperfection.72



Abbreviations

DC	=	Direct current
AC	=	Alternating current
FDTD	=	Finite-difference time-domain
QD	=	Quantum dot
InAs	=	Indium arsenide
GaAs	=	Gallium arsenide
GaSb	=	Gallium antimonide
SK mode	=	Stranski-Krastanov mode
AuGa	=	Auric gallium
Ni	=	Nickel
AuZn	=	Auric zinc
MBE	=	Molecular beam epitaxy
PGMEA	=	Glycol 1-monomethyl ether 2-acetate
AR	=	Isopropyl alcohol
IP-L 780	=	Acrylic-based resin
GWL file	=	General writing language file
DLW	=	Direct laser writing
W	=	Watt
KCL	=	Kirchhoff's current law
<i>I-V</i> curve	=	Current-voltage curve
3D, 2D	=	The 3-dimensional and 2-dimensional, respectively
IR ranges	=	Infrared ranges
<i>Q</i> mode	=	Quality mode
PML	=	Perfectly matched layer
WGM mode	=	Whispering gallery mode
LED	=	Light-emitting diodes
min	=	Minute

Abbreviations (CONT.)

QW	=	Quantum well
SNAP	=	Surface nanoscale axial photonics
UV	=	Ultraviolet
PL	=	Photoluminescence
eV	=	Electron volt
Si	=	Silicon
CdTe	=	Cadmium telluride
CdS	=	Cadmium sulfide
CIS	=	Copper indium diselenide
CIGS	=	Copper indium gallium diselenide
TiO ₂	=	Titanium dioxide
NiCr	=	Nickel chromium
Al	=	Aluminium
ECI	=	Electrochemical interface
FRA	=	Frequency response analyzer
SEM	=	Scanning electron micrograph
CO ₂	=	Carbon dioxide
SiO	=	Silicon monoxide
SiO ₂	=	Silicon dioxide
AlAs	=	Aluminum arsenide
ICP-RIE	=	Inductively coupled plasma reactive ion etching
BS	=	Beam-splitter
MOSFET	=	Metal-oxide-semiconductor field-effect transistor
TE	=	Transverse electric
TM	=	Transverse magnetic
Hz	=	Hertz

Abbreviations (CONT.)

$v_{S,DC}$	=	DC biased voltage source
$R_{S,DC}$	=	Series resistor within the DC biased circuit
R_S	=	Series resistance
I_{PH}	=	Photocurrent
R_{SH}	=	Shunt resistance
I_O	=	Reverse saturation current
n	=	Diode ideality factor
I_D	=	p-n junction diode current
V_D	=	Diode voltage
$W(.)$	=	Lambert W function
V_{PV}	=	DC voltage of hybrid QD solar cell
I_{PV}	=	Current of hybrid QD solar cell
T	=	Absolute temperature
k	=	Boltzmann constant ($k = 1.38 \times 10^{-23}$ J/K)
q	=	Electron charge ($q = 1.6 \times 10^{-19}$ C)
$I_{PV,exp}^i$	=	Experimentally measured current
$I_{PV,cal}^i$	=	Calculated current
F_{DC}	=	DC fitness value
$C_{S,AC}$	=	Capacitor within the AC biased circuit
$R_{S,AC}$	=	Resistor within the AC biased circuit
$v_{S,AC}$	=	AC biased voltage
A_{in}	=	Amplitude of input voltage
A_{out}	=	Amplitude of output voltage
v_{PV}	=	AC solar cell voltage
ϕ	=	Phase difference
f	=	Frequency
C_D	=	AC diode capacitance
R_D	=	AC diode resistance

Abbreviations (CONT.)

R_{SH}^{AC}	=	AC shunt resistance
R_S^{AC}	=	AC series resistance
Z_{out}	=	Total impedance of output side
Z_{in}	=	Total impedance of input side
F_{AC}	=	AC fitness value
i	=	Each data point
D	=	Diameter of the structure
L	=	Lateral length
N	=	Total mumble of column holes
M	=	Total mumble of raw holes
a	=	Hole period
p, q and c	=	Positive number of hyperboloid structure
H	=	Height
L_h	=	Spiral line length
$L_{h,t+1}$	=	Spiral line length at time $t+1$
ΔL_h	=	Delta length
$T_{h,t+1}$	=	Spiral line length at time $t+1$
T_h	=	Spiral line length
ΔT	=	Delta time
x_{t+1}	=	Position x at time $t+1$
y_{t+1}	=	Position y at time $t+1$
z_{t+1}	=	Position z at time $t+1$
x_0	=	Initial position x
y_0	=	Initial position y
t	=	Iteration
$T_{h,Line}$	=	Thickness of a spiral line

Abbreviations (CONT.)

D_B	=	Bottom diameter
D_c	=	Central diameter
D_T	=	Top diameter
Z_{out}	=	Total impedance of output side
Z_{in}	=	Total impedance of input side
c	=	Speed of light ($c = 3 \times 10^8$ m/s)
Δf	=	Narrow frequency width
r	=	Hole radius
m	=	Mode index
H_z	=	Perpendicular magnetic field
E_x	=	Electric fields in plane along x
E_y	=	Electric fields in plane along y
Q factor	=	Quality factor
$n_{substrate}$	=	Refractive index of substrate
n_{resin}	=	Refractive index of resin
Δn	=	Refractive index contrast between substrate and resin
I_{SC}	=	Short circuit current
V_{OC}	=	Open circuit voltage
I_{MPP}	=	Maximum power point current
V_{MPP}	=	Maximum power point voltage
P_{MPP}	=	Maximum power point power
FF	=	Fill factor
R^O	=	Static resistance
f_c	=	Resonant frequencies
n_e	=	Effective index of hollow cylindrical optical microcavities
λ	=	Optical wavelength
w	=	Width of missing hole line
n_{eff}	=	Effective refractive index of hyperboloid microcavities

Abbreviations (CONT.)

λ_m	=	Wavelength of interesting mode
λ_{m+1}	=	Wavelength of nearby mode
$\Delta\lambda$	=	Wavelength width between interesting mode and nearby mode
I_{SH}	=	Shunt current
τ	=	Minority carrier lifetime
C_t	=	Transition capacitance
C_d	=	Diffusion capacitance
X_s	=	Reactance
C_μ	=	Chemical capacitance
C_{CE}	=	Interfacial capacitance
R_{CE}	=	Charge transfer resistance
Z_d	=	Diffusion impedance
r_{tr}, r_r	=	Electron transport resistance
r	=	Series resistance of bulk and interconnects
$\Delta\lambda_m$	=	Width of the peak mode

CHAPTER I

INTRODUCTION

1.1 Background and Significance of the Study

Nowadays, photonic devices are variously applied in power manufacturing, data transmissions, optical communications and signal processing, detector, sensors, and light sources. They can be categorized according to their functions (1) such as solar cells, light-emitting diodes, laser diodes and photodetectors. The solar cells can be divided into 3 main generations (2). The first generation of solar cells uses the crystalline wafer based technology such as monocrystalline, polycrystalline and gallium arsenide solar cells. The second generation of solar cells uses thin-film technology, e.g., amorphous silicon and cadmium telluride solar cells. The third generation of solar cells is developed by fabricating from emerging nanomaterials, e.g., quantum dots (QDs), quantum wells (QWs), nanowires and carbon nanotubes solar cells.

The QD solar cells are interesting in this work. The firstly interesting photonic structure can enhance the efficiency of the QD solar cells by using different QD type. The QDs solar cells can adjust the energy band gap (23-25). So the QDs can absorb light with various wavelength ranges. The InAs/GaAs QDs have the confinement of both electrons and holes in the same region. The InAs/GaAs QDs have been used to achieve the enhancement of light emission and absorption (25). So the efficiency of InAs/GaAs QD solar cells are enhanced. For GaSb/GaAs QDs, electrons and holes in GaSb/GaAs QDs are separated. The holes are confined in the the GaSb QDs while the electrons are around (outside the dot). This GaSb/GaAs QD property leads to a long carrier lifetime (26, 58). Typically, GaSb/GaAs QDs have low carrier-recombination rate, emitting and absorbing of low photon energy (30).

The electrical behavior and efficiency of solar cells can be analyzed from different equivalent circuit models and values of extracted parameters. The models of solar cells classified as the DC equivalent circuit model and the AC equivalent circuit model. The DC equivalent circuit models (59 - 64, 75) of solar cells are most widely

considered because of its correctness and simplicity. The DC characteristic of solar cells is the current-voltage characteristic. This current-voltage relation can be expressed by using exponential or Lambert W function (61, 62). The DC equivalent circuit model consists of current source, pn junction diode, shunt resistance and series resistance. The AC equivalent circuit model (34-39) is investigated from measuring of AC characteristics. The AC characteristics of the solar cell can be obtained from various spectroscopic techniques such as impedance spectroscopy in frequency domain (35), transient response by using open circuit voltage decay technique (37) and the capacitance measuring by using triangular wave technique (38). Several techniques have been used to determine the equivalent circuit parameters.

The secondly interesting photonic structure is the optical microcavities. We expect that microcavity array could be applied in improving the efficiently surface coating of solar cells. Optical microcavities can confine light in small volumes at certain wavelengths. The three-dimensional (3D) different shapes of optical microcavities are spherical microcavity (41, 42), toroid microcavity (43-45), tubular microcavity (73, 46-48) and bottle microcavity (49-51). The obtained shapes depend on various fabrication techniques. Relevant techniques for fabricating optical microcavities (52) are melting and splicing optical fibers (49, 53), rolling-up mechanism of semiconductor bilayers (73, 46, 47), lithography and etching technologies (45, 48, 54, 55), surface nanoscale axial photonics (SNAP) technology, ultraviolet (UV)-curable adhesive, self-assembly procedure, etc. Among them, Nanoscribe 3D lithography technology (67-69) can create precise micro-shapes and smooth surface. After the fabrication of optical microcavities, optical characterization of optical microcavities can be investigated from transmission spectrum and photoluminescence (PL) spectroscopy, etc. Transmission measurement (48) reveals the transmission spectrum as function wavelengths by using a light coupling method. The PL spectroscopy (56-57) gives the light intensity as function of emission wavelength (or the energy of emitting photon). Both transmission measurement and PL spectroscopy can reveal resonant modes of the optical microcavity.

In this work, we investigate two types of hybrid QD solar cells. Type-A hybrid QD solar cell is hybrid GaSb/GaAs and InAs/GaAs QD solar cell. Type-B hybrid QD solar cell is hybrid InAs/GaAs and GaSb/GaAs QD solar cell. The various

designed photonic structures of hybrid QD solar cells can enhance their performance. The investigated photonic structures have two comparative structures. The first one is QD structure of hybrid QD solar cells. The QD structure can enhance the solar cell performance by the increase of stacked hybrid QD layers and the correctly stacking QDs sequence. The second photonic structure is optical microcavities. Microcavity array might be applied to improve the efficiency of solar cells even it has not been done in this work.

In the first photonic structures, the performances of solar cells with QD structures will be analyzed and discussed. The DC and AC characteristics and circuit parameters of various hybrid QD solar cells are investigated. The second photonic structures is hollow optical microcavities. The hollow cylindrical and hyperboloidal optical microcavities are presented. The hollow cylindrical microcavities are numerically simulated for the single whispering gallery mode (WGM) by using the finite-difference time-domain (FDTD) method. Fabrication and optical characteristics of hyperboloidal microcavities is discussed.

1.2 Purposes of the Study

1. To study the hybrid QD solar cells and their DC and AC electrical characteristics.
2. To study the QD (the first photonic structure) in enhancing the efficiency of the hybrid QD solar cells by the increase of stacked hybrid QD layers and the correctly stacking QD sequence.
3. To study the optical microcavity (the second photonic structure) by investigating the related simulation, the fabrication and the optical properties.
 - 3.1 To study the numerical simulations of the single WGM enhancement in hollow cylindrical microcavities by using the FDTD method.
 - 3.2 To study the fabrication and optical characteristics of hollow hyperboloidal microcavities.

1.3 Scope of the Study

1. The solar cells with hybrid QD structures are improved by the increase of stacked hybrid QD layers and the correctly stacking QDs sequence. The DC and AC circuit parameters are extracted the different type of different hybrid InAs/GaAs QDs and GaSb/GaAs QDs in each studied case.

1.1 Current-voltage characteristics of the hybrid QD solar cells are measured for DC circuit parameters extraction.

1.2 Frequency responses of the hybrid QD solar cells under controlled bias condition are measured for AC circuit parameters extraction.

2. The optical hollow microcavities are the interesting photonic structure are modified and investigated.

2.1 The single WGMs in hollow cylindrical microcavities are modified by varying the structured parameters in the FDTD simulation. Electric and magnetic field profiles and enhanced resonant modes are investigated.

2.2 The hollow hyperboloid microcavities are fabricated by using 3D Nanoscribe machine. Optical characteristics of hollow hyperboloid microcavities are investigated from PL measurement.

1.4 Hypotheses of the Study

1. The DC circuit parameters of hybrid QD solar cells are the reverse saturation current I_0 , the diode ideality factor n , the photocurrent I_{PH} , the series resistance R_S and the shunt resistance R_{SH} . Increase of stacking layers and the correct stacking sequence of hybrid QD type in QD layers relate and affect the DC circuit parameters and performance of hybrid QD solar cells. Increase of stacking layers, which increases the total layer thickness might result in the increase of series resistance R_S and the reduction of shunt resistance R_{SH} . The correct stacking sequence of hybrid QDs can result in the better performance, the lower series resistance R_S and the higher shunt resistance R_{SH} .

2. The AC circuit parameters of hybrid QD solar cells are the diode capacitance C_D , the diode resistance R_D , the AC series resistance R_S^{AC} and the AC

shunt resistance R_{SH}^{AC} . They are extracted by the fitting the frequency response under the controlled bias condition at the maximum power point. The AC shunt resistance R_{SH}^{AC} , the AC series resistance R_S^{AC} and a capacitance R_D of 3-pair hybrid QD solar cell should have higher values. The extracted AC parameters relate to the device structure.

3. The FDTD simulation is used for theoretical study of single WGM optical microcavity. Structural parameters of hollow cylinder microcavity are varied. The resonant frequency f_c and quality Q factor depend on both the hole radius r and the cavity width w . The number of holes in both vertical and horizontal directions affect Q factor. New shape of optical microcavities is presented. It is the hollow hyperboloid microcavities. This new shape is also named as anti-bottle resonator. The hollow optical microcavities have noticeable resonant modes.

1.5 Expected Benefits

1. This research ameliorates the knowledge and comprehension of the experimental realized novel photonic structures and semiconductor devices with quantum nanostructures. It is believed that the equivalent circuit model can predict many important performance parameters of photonic devices such as QD solar cell and photodetector.

2. The experience and knowledge about fabrication process and WGM improvement of optical microcavities are obtained. In the future, we expect that optical microcavities can be applied in enhancement the efficiencies of solar cells, photodetectors and other photonic devices. Furthermore, WGMs can enhance the detecting in the near-infrared range.

CHAPTER II

THEORY AND LITERATURE REVIEW

2.1 Solar Cells

Solar cells are divided into 3 main generations (see Figure 1) (2, 3). The third generation of solar cells is considered from differently fabricated technologies. Nowadays, the solar cells have been used extensively. However, many types of solar cells are still under development and research.

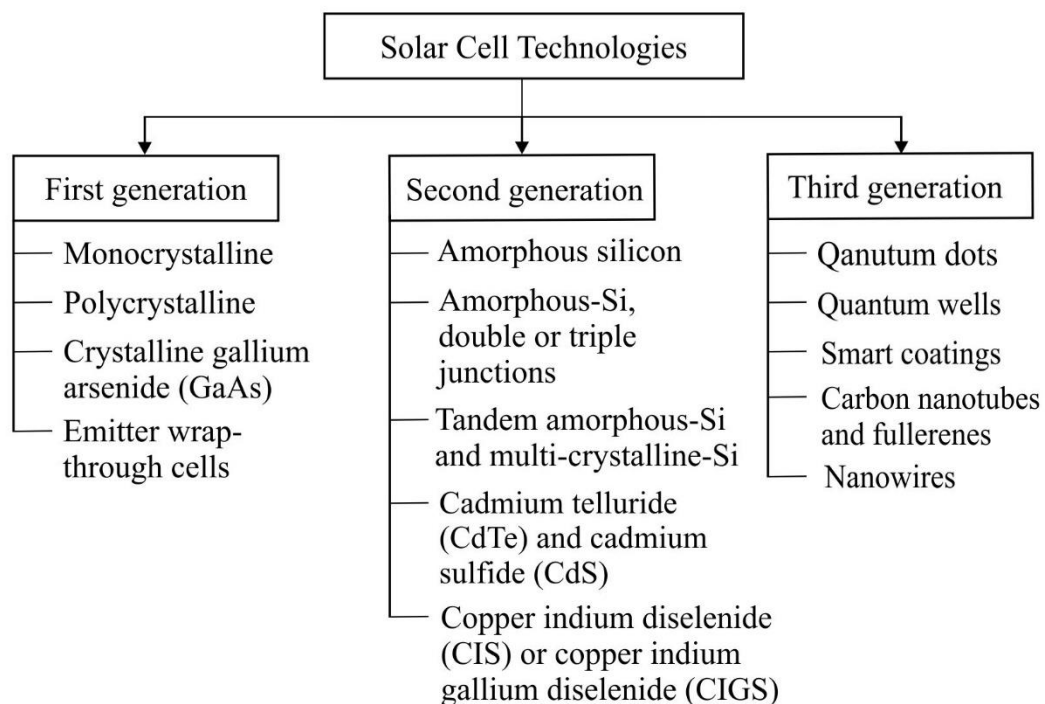


Figure 1 Diagram showing the 3 main generations of solar cells.

The first generation of solar cells as shown in Figure 2 uses the wafer-based crystalline technology. Silicon (Si) is the main material for realizing the solar cells, e.g., monocrystalline silicon, polycrystalline silicon and emitter wrap-through solar cells. This technology provides high-efficiency solar cells. Therefore, the first generation of solar cells has still been applied widely. For example, the

monocrystalline Si solar cell is the most generally utilized in the market (~80%). The monocrystalline Si solar cell is made of crystalline Si p-n junctions. A single crystal Si is grown by using the Czochralski method (4). Using a polycrystalline solar cell (instead of the single crystal) can reduce the cost of manufacture. In some studies, the polycrystalline solar cell has fewer defects than metal contamination than the monocrystalline cell (5). The GaAs-based solar cells are developed for high conversion efficiency (typically higher than the crystalline Si). Moreover, GaAs solar cells have an advantage that they can be very thin (a few microns) and have high resistance to heat and radiation damage (2). Emitter wrap-through cells do not have the front contacts, so light radiation can be fully absorbed at the top surface of the solar cells (7).

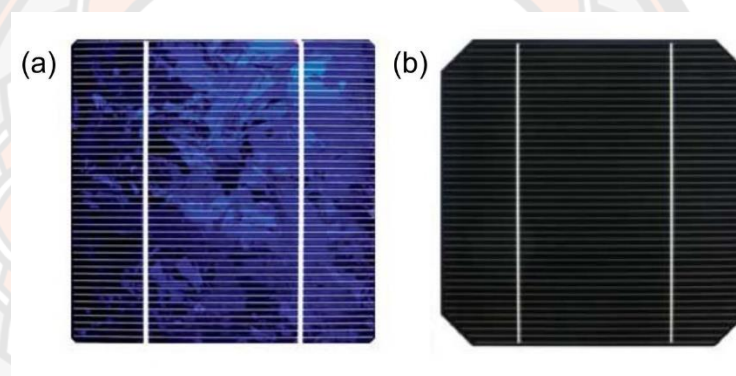


Figure 2 (a) polycrystalline and (b) monocrystalline Si solar cells (6)

The second generation of solar cells is fabricated from thin-film technologies such as amorphous Si, cadmium telluride (CdTe), cadmium sulfide (CdS), tandem amorphous-Si and multi-crystalline-Si. For demonstration, the electronic properties of larger band gap in amorphous Si solar cells are observed. They can efficiently absorb light in the visible spectrum range (8). Tandem amorphous-Si and multi-crystalline-Si solar cells (9) consist of multi-layers. The efficiency depends on the structure and thickness of each layer. The obtained efficiency is higher than of amorphous Si solar cells, which is about 9%. Researches of CdTe (12) and CdS solar cells (2, 10) show that the solar cells can be fabricated from CdS core or copper sulfide shell nanowire by using a solution-based cation exchange reaction at a low temperature. The energy conversion efficiency is more than that of planar solar cells. Copper indium diselenide

(CIS) (11) or copper indium gallium diselenide (CIGS) solar cells use more effective materials, but the fabrication process becomes more difficult and complicated.

The third generation of solar cells is still under development and research. Integrations of nanomaterials such as quantum wells (QWs), carbon nanotubes, nanowires or QD into solar cells are examples of this development. For instance, QD solar cells (13-14) can enhance absorption via multiple energy levels of light. They can absorb light in the infrared range. The different volume and size of QD solar cells affect the light absorption properties. The QD solar cells are developed by various methods and contain many different layers. The different dimensions of QDs can be applied to adapt their band gap and absorption light. The energy of band gap is inversely proportional to the size of QDs (15). In QW solar cells (16), a potential well has only discrete energy values. The QW solar cells are typically fabricated from semiconductor heterojunctions. For instance, GaAs is sandwiched between two layers of a semiconductor material with a wide band gap, e.g. AlGaAs.

Smart coating is a method that selects materials from their electro-optical characteristics in order to enhance the system efficiency by using the light control factors of the materials. For example, Huang et al. (17) fabricate the solution type photovoltaic electrochromic device, which includes an electrochromic solution disposed between a transparent nonconductive substrate and a semi-transparent Si thin film substrate of solar cell. When the system is illuminated by sunlight, the Si thin film solar cell is persuaded to a redox reaction of the electrochromic solution. When the sunlight declines, the solution type photovoltaic electrochromic device restores its transparency because of the self-bleaching property.

At present, the limited raw materials and high production costs induce the increasing demand of replacement. Carbon nanotubes (Graphene) and fullerene solar cells can be transparent conducting films with high flexibility (18). Nanowires (19-21) solar cells are designed by using one dimensional nanostructure as the building block. This nanostructure exhibits the unique chemical and physical properties.

2.2 Hybrid Quantum-Dot Solar Cells

The QD solar cells are initially realized based on the intermediate band concept (22, 23) as well as the energy-band-adjustability of the nanostructures. The efficiency of QD solar cell depends also on the QD size (23-25). This QD size effect is determined by the effectively enhanced bandgap and the absorption wavelength range. The InAs/GaAs and GaSb/GaAs QDs can be grown from the self-assembled growth in Stranski-Krastanov (SK) mode by using molecular beam epitaxy (MBE) (26, 27, 28). The schematic of MBE is shown in Figure 3.

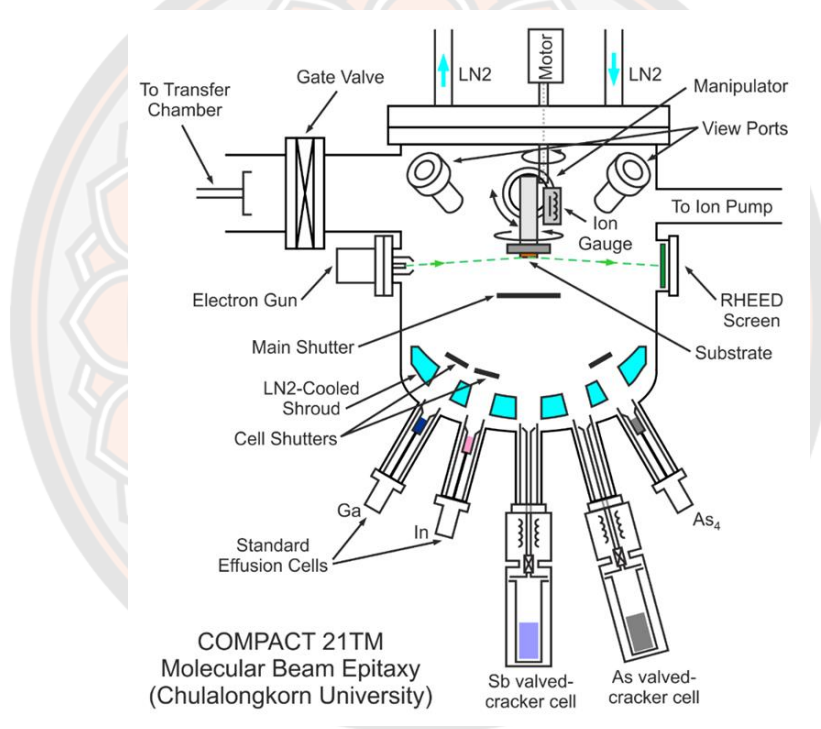


Figure 3 The component diagram of MBE

Considering the type of heterojunction, the alignment of the straddling gap exhibits in InAs/GaAs QD layer. The InAs QDs as shown in Figure 4 confine both electrons and holes in the dot (29). Regularly, carrier recombination and absorption of InAs/GaAs QD layer occur at high rate. The increasing of stacked QD layer number can enhance the light absorption in QDs (23, 24). For GaSb/GaAs QDs, the staggered gap in GaSb/GaAs QDs (30, 28, 31) exhibits spatial separating of the electrons and

holes. In other words, the confined holes in the GaSb QDs while the electrons are surrounding in GaAs capping layer as schematically shown in Figure 4.

The small overlapping of carrier wave function in the staggered gap band leads to a long carrier lifetime (32, 33). Advantages of InAs/GaAs QDs and GaSb/GaAs QDs are the powerful light absorption and the long carrier lifetime of QDs, respectively. Both advantages can be integrated into the hybrid QD solar cell (26, 33).

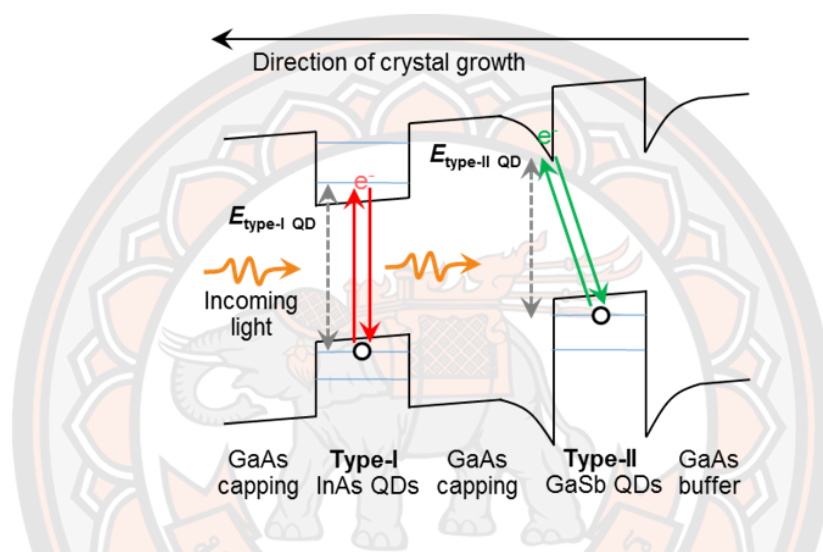


Figure 4 Carrier Injection from InAs/GaAs QDs to GaSb/GaAs QDs (26)

2.3 The Equivalent Circuit Model of Solar Cell

The equivalent circuit models of hybrid QD solar cells are the DC equivalent circuit model and the AC equivalent circuit model.

2.3.1 DC Equivalent Circuit Model

The DC circuit models of hybrid QD solar cells are depicted in Figures 5-8. The models (59-64, 75) are developed as follows:

The ideal circuit model for solar cell in Figure 5 consists of the parallel connection between a diode D and a photocurrent source I_{PH} . In the fact that the pn-junction absorbs the incident light. After that, the electron-hole pairs are generated in or near the depletion region. A part of the emerging photocurrent I_{PH} can flow to an

external circuit as $-I_{PV}$. The voltage V_{PV} is the junction voltage of solar cell. The current I_{PV} is the junction current of solar cell.

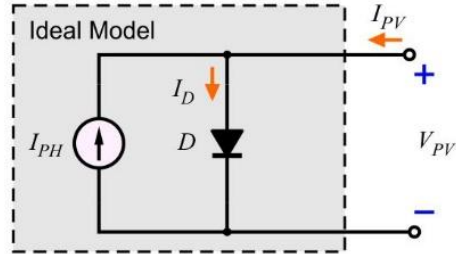


Figure 5 Ideal equivalent circuit model

The ideal circuit model of solar cell has only p-n junction. This model is parallel connection of a diode and a photocurrent source. The solar cell current I_{PV} equals subtraction of the photocurrent I_{PH} with the pn-junction current I_D . So $I_{PV} = -I_{PH} + I_D$. The pn-junction diode current I_D can be described by using the Shockley equation $I_D = I_o(\exp(qV_{PV}/nkT) - 1)$. This ideal equivalent circuit model has 3 extracted parameters. They are the ideality factor n , the photocurrent I_{PH} and the reverse saturation current I_o . The current-voltage characteristics of ideal equivalent circuit model can relate as shown in Equation (2.1).

$$I_{PV} = -I_{PH} + I_o \left(\exp\left(\frac{qV_{PV}}{nkT}\right) - 1 \right) \quad (2.1)$$

where I_{PV} represents the solar cell current (A), I_{PH} represents the photocurrent (A), I_o represents the reverse saturation current (A), V_{PV} represents the solar cell voltage (V), k represents Boltzmann constant ($k = 1.3807 \times 10^{-23}$ J/K), q represents amplitude of electron charge ($q = 1.60 \times 10^{-19}$ C), and T represents the temperature of solar cell (K).

The series resistance circuit model includes a series resistance R_S in this circuit (as shown in Figure 6). When in the depletion region has occurrence of the electron-hole pairs, electrons flow through the pn junction to the external circuit. A series resistance R_S in this model represents the contact resistance. The series resistance circuit model has 4 extracted parameters. They are the ideality factor n , the

photocurrent I_{PH} , reverse saturation current I_o and the series resistance R_S . The current-voltage characteristics of the series resistance circuit model can be presented in Equation (2.2).

$$I_{PV} = -I_{PH} + I_S \left[\exp\left(\frac{q(V_{PV} + R_S I_{PV})}{akT}\right) - 1 \right] \quad (2.2)$$

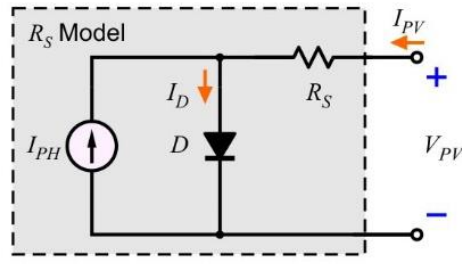


Figure 6 Series resistance circuit model

The shunt resistance circuit model is shown in Figure 7. The only shunt resistance R_{SH} is added into this model while the series resistance R_S is omitted. Part of the electrical current will flow through the pn junction to the external circuit, but a small fraction of the electron-hole pairs can flow through some defects. The included shunt resistance R_{SH} reflects these effects. The high leakage current, which flows through defects, is represented by a low value of the shunt resistance. It is called the shunt current I_{SH} . The shunt resistance circuit model has 4 extracted parameters. They are the ideality factor n , the photocurrent I_{PH} , the reverse saturation current I_o and shunt resistance R_{SH} . The I - V characteristics of the shunt resistance circuit model can be represented by Equation (2.3).

$$I_{PV} = -I_{PH} + I_o \left(\exp\left(\frac{qV_{PV}}{nkT}\right) - 1 \right) + \frac{V_{PV}}{R_{SH}} \quad (2.3)$$

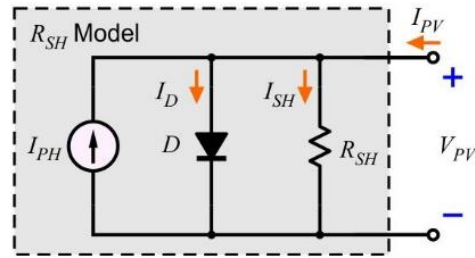


Figure 7 Shunt resistance circuit model

The series and shunt resistance circuit model is shown in Figure 8. Both series resistance R_S and shunt resistance R_{SH} are considered in this circuit model. The contact resistance and leakage current are simultaneously considered. The series and shunt resistance circuit model has 5 extracted parameters. They are the photocurrent I_{PH} , the ideality factor n , the reverse saturation current I_o , the series resistance R_S and the shunt resistance R_{SH} . The current-voltage characteristics of the series and shunt resistance circuit model can be related and shown in Equation (2.4).

$$I_{PV} = -I_{PH} + I_S \left[\exp \left(\frac{q(V_{PV} + R_S I_{PV})}{akT} \right) - 1 \right] - \frac{V_{PV} + R_S I_{PV}}{R_{SH}} \quad (2.4)$$

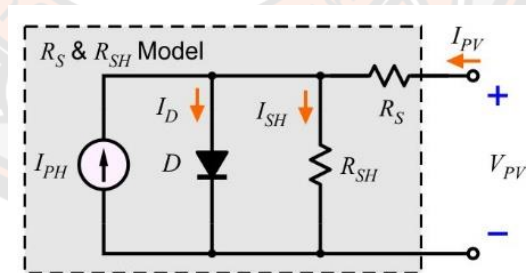


Figure 8 The series and shunt resistance circuit model

2.3.2 AC Equivalent Circuit Model

For AC circuit model, several techniques are used to determine the AC circuit parameters of solar cells. In references (34-39), models have been proposed and studied techniques for the AC circuit parameter extraction as follows.

In the paper of Suresh (35), impedance spectroscopic curve in frequency domain is used for the determination of AC circuit parameters in a back-surface reflector field solar cell. The parameters are the short-circuit current I_{SC} , the series resistance of bulk and interconnects r , the AC resistance R_d , the parallel resistance R_p , the diffusion capacitance C_d and the transition capacitance C_T . The AC equivalent circuit model is illustrated in Figure 9. They found that the diffusion capacitance C_d has a maximum value at open circuit voltage. The AC diode resistance R_d is an essential parameter of the solar cell power system and indicates the cell stability.

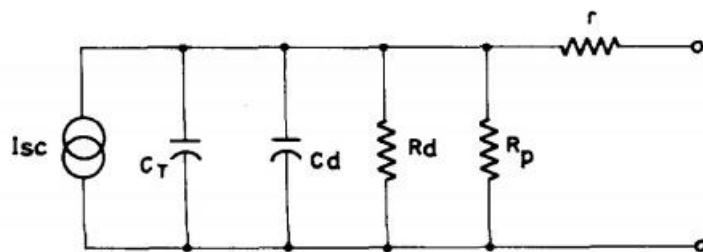


Figure 9 The simplified AC equivalent circuit model of a solar cell (35).

González-Pedro et al. (36) have used the impedance spectroscopy to analyze QD sensitized solar cell characterization. The AC equivalent circuit model of a QD sensitized solar cell is presented in Figure 10. The extracted parameters are $R_S, r_{tr}, r_r, C_\mu, R_{CE}$ and C_{CE} . (Z_d is neglect.) A series resistance R_S occurs in the transparent conducting oxide. The electron transport resistance r_{tr}, r_r and the chemical capacitance C_μ appear in the TiO_2 . The r_r is an inverse ratio to both the electron density in TiO_2 and the recombination rate. C_μ indicates the trapping of electrons in the bandgap of the TiO_2 . The number of electron transport resistance r_{tr}, r_r and the chemical capacitance C_μ depend on the TiO_2 layer thickness. The interfacial capacitance C_{CE} and charge transfer resistance R_{CE} occur in the counter electrode. Z_d represents the diffusion impedance. These parameters relate to the carrier transport, charge transfer and recombination of the solar cell.

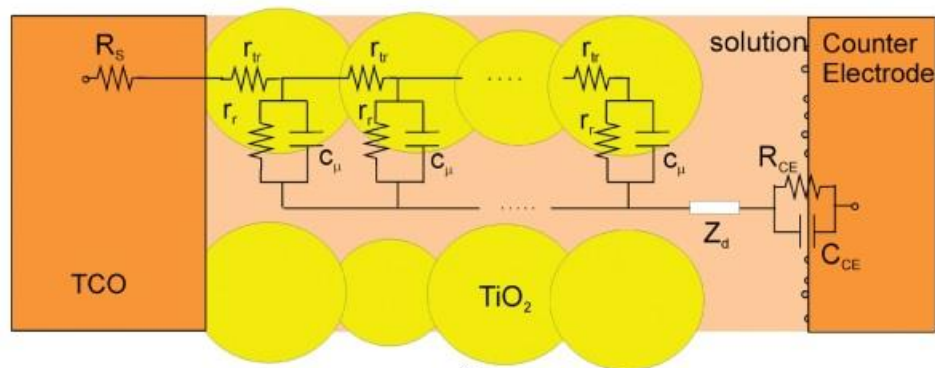


Figure 10 The AC equivalent circuit model of a QD sensitized solar cell is proposed by González-Pedro et al. (36).

Ramadan and Martín-Palma (40) use a Nyquist plot (or a frequency response plot) and corresponding impedance for curve fitting and parameter extractions from the investigated solar cells. Samples of nanostructured porous Si (nanoPS) and silver nanoparticles within solar cells have the AC equivalent circuit model as shown in Figure 11. This AC circuit model consists of a series resistance R_s and capacitors C_1 . The first interface consists of a resistances R_1 in Al/active layer. The second interface consists of a constant phase element Q and resistances R_2 in active layer/ TiO_2 . The final interface consists of capacitors C_3 and resistances R_3 in TiO_2/NiCr layer. The resistances relate to the carrier transport. The capacitance relates to the accumulation and distribution of carriers. Moreover, characteristic capacitance C is associated with the presence of defects.

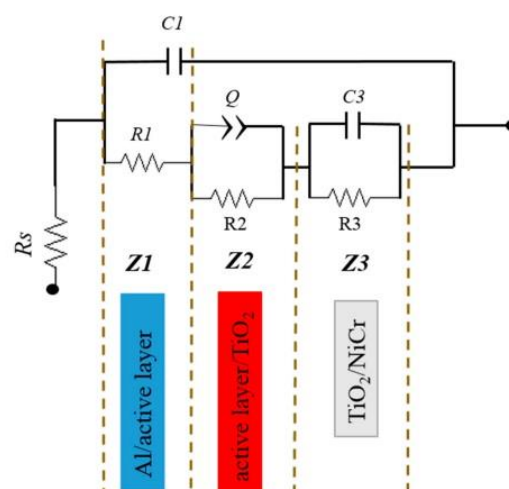


Figure 11 The AC equivalent circuit model of nanoPS and silver nanoparticles in solar cells is presented (40).

2.4 DC Characteristic: Current - Voltage Characteristic

Current and voltage of the solar cell are measured when light is illuminated on the measured cell. The current - voltage characteristic can be obtained as shown as an example in Figure 12(a). We (63) found that fitness values is minimum as in Figure 12(b), when the series and shunt resistance model is used in the fitting of current-voltage curve (See Chapter 3 for more details of the fitting procedure and the definition of the fitness value). So the series and shunt resistance model is the best for DC parameter extraction.

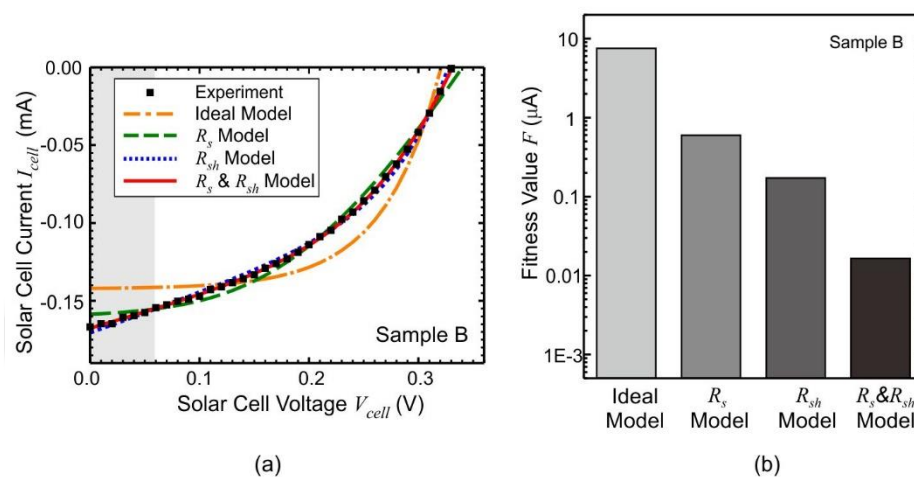


Figure 12 (a) The DC current-voltage characteristics of a hybrid QD solar cell are measured and fitted. As well as (b) fitness values are obtained from fitting the curves with different DC circuit models.

2.5 AC Characteristics: Frequency Response

AC Characteristics are of interest. They can be measured by (a) impedance spectroscopy in frequency domain, (b) transient response by using open circuit voltage decay technique and (c) the capacitance measuring by using triangular wave technique. These measurements for AC characteristics are described in the next paragraphs.

(a) Impedance Spectroscopy in Frequency Domain

Suresh (35) measured impedance spectroscopy in frequency domain. The measuring is set in the dark at room temperature. Resistance R_s - reactance $j X_s$ curves are obtained in impedance spectroscopy as various voltages. These R_s - $j X_s$ curves look like semicircle curves. The AC equivalent circuit model in Figure 9 consists of parallel connection of an AC diode resistance R_d and a capacitance C_d . The parallel resistance R_p has very high value, so it can be neglected. Measurement setup of impedance spectroscopy is shown in Figure 13. This system comprises of electrochemical interface (ECI), a frequency response analyzer (FRA), solar cell and computer. DC current and voltage of input can be injected into the electrochemical interface. The FRA sends the needed AC signal over the DC voltage through an electrochemical interface. Current i and voltage v are measured by FRA. After that, the impedance values of solar cell are calculated by FRA at the frequency range (from 63.1 kHz to 10 Hz). Finally, the results are sent to the computer.

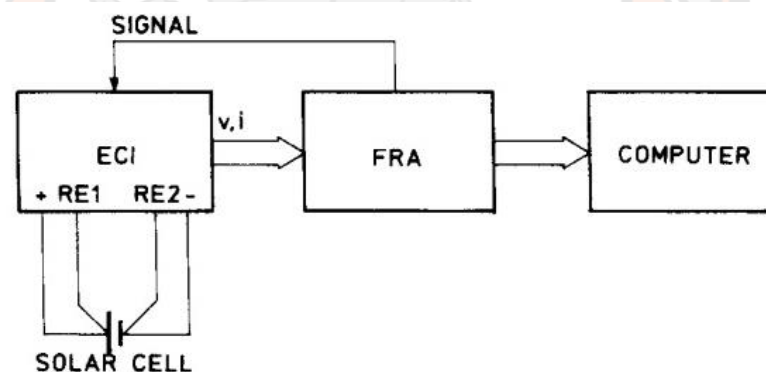


Figure 13 Measurement setup of impedance spectroscopy in frequency domain (35).

(b) Transient Response in Time Domain

Deshmukh et al. (37) have measured the transient response by using the decay technique of open circuit voltage V_{OC} in the time domain. Measurement setup in Figure 14 comprises of a digital storage oscilloscope, a constant current source, a solar cell sample, a switch, a reverse blocking diode and a personal computer. The constant current source is set at short circuit current I_{SC} . The current is abruptly

terminated by controlling of MOSFET switch because the results must be obtained at the accurately minimum voltage decay. The applied MOSFET switch helps to block the voltage across the solar cell and abstain from its discharge through the shunt switch. So a signal diode (1N4148) is used because of it small reverse recovery time of 4 ns. The digital storage oscilloscope is used for measuring of voltage decay and finally the measured data is sent to the computer. Transient response by using V_{OC} decay technique provides the solar cell voltage as a function of time. The total resistance of the cell is the shunted connection between the shunt resistance R_{SH} and the AC resistance R_d . The AC resistance R_d of the solar cell is calculated by using $R_d = 1/(dI/dV)$. In more detail, the slope (dI/dV) of the current-voltage characteristic is calculated by using the Savitzky-Golay algorithm. The solar cell capacitance is calculated from $C = 1/(dV/dt)_{V=V_b}$ by using this transient response.

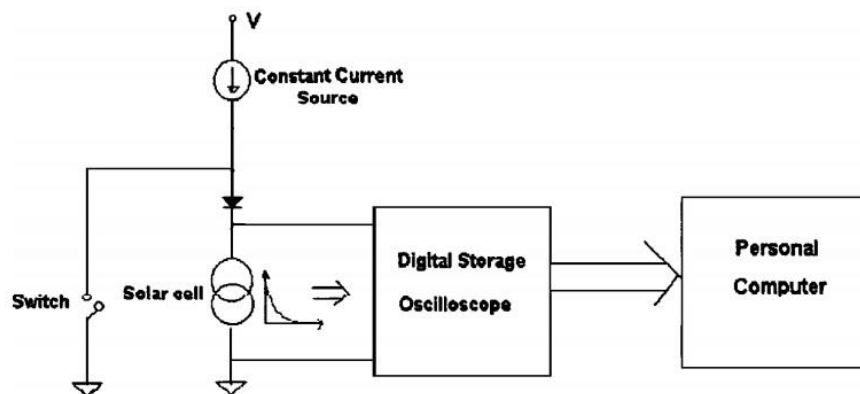


Figure 14 Measurement setup of open circuit voltage decay technique in the time domain (37).

(c) The Capacitance Measuring by using Triangular Wave Technique

Mandal and Nagaraju (38) use triangular wave technique at different temperature under dark condition. It is a frequency domain technique. The measurement setup is presented in Figure 15. Various periodical triangular voltages of input signal can be set from a waveform generator. The signal frequency is adjusted. The AC current amplitude of the solar cell is recorded as a function of time. The solar cell capacitance is calculated from the parallel connection of the transition capacitance C_t and the diffusion capacitance C_d . The transition capacitance is

calculated from $C_t = |dQ/dV_{PV}|$ where V_{PV} is the solar cell voltage. The diffusion capacitance is calculated from $C_d = (\tau/2V_T n)I_d$, where I_d is the diode current under dark condition, n is the diode ideality factor and τ is the minority carrier lifetime.

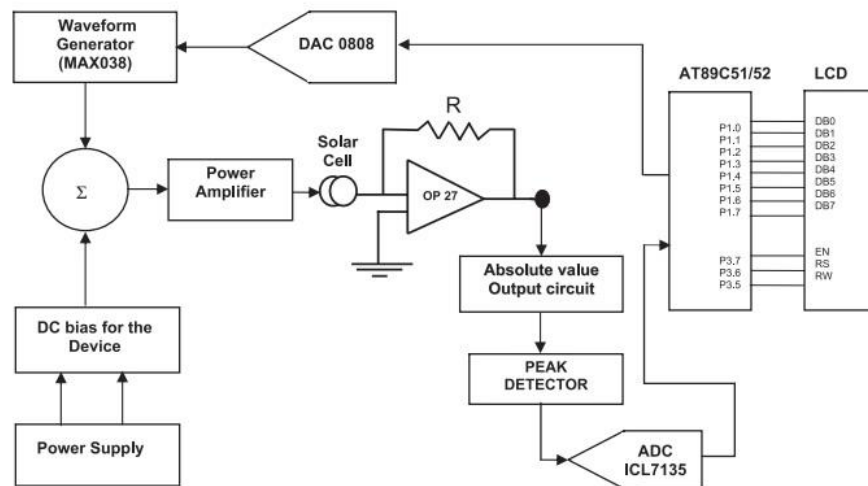


Figure 15 Measurement setup of the capacitance measuring by using triangular wave technique (38).

2.6 Type of Optical Microcavities

Types of optical microcavities are categorized according to their shapes. They are such as spherical microcavity, toroidal microcavity, tubular microcavity and bottle microcavity.

(a) Spherical Microcavities

The optical spherical microcavities are designed in the shape of sphere as shown in Figure 16. Han et al. (41) have developed a numerical simulation by using scattering theory to derive an exact quasi-analytic solution. The scattering spectra for the transverse electric (TE) and transverse magnetic (TM) mode and individual first-order scattering coefficients present the results of the resonance spectrum for a distorted spherical microcavity. At some locations, the Q factor at some individual scattering coefficients is obtained. Aktas et al. (42) have simulated and fabricated the on-chip spherical chalcogenide microcavity array. The materials are a chalcogenide

glass core and thermoplastic polymer polyethersulfone cladding. The transmission spectra of these cavities generally exhibit a high Q factor.

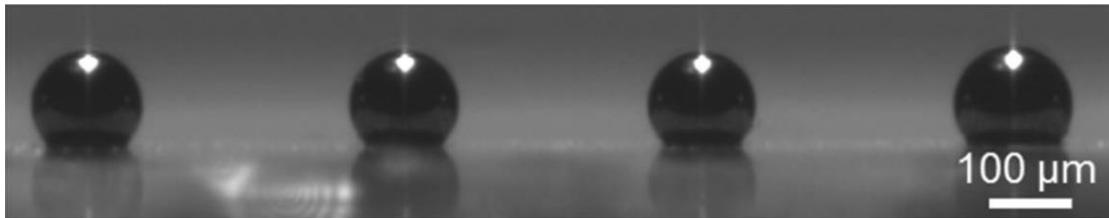


Figure 16 The scanning electron micrograph (SEM) of on-chip spherical chalcogenide microcavity array (42)

(b) Toroidal Microcavities

The shape of optical toroidal microcavity (or microdisk microcavity) is shown in Figure 17. This shape looks like a flat disk with a smooth edge. The D represents a principal diameter and d represents a minor diameter. In 2003, Kippenberg et al. (45) have fabricated silica disk microcavities by using standard lithographic techniques. The spectrum and WGM resonant modes are obtained from transmission spectrum measurement. High Q factor of 2×10^4 obtains at the wedged shaped edge. This may isolate modes from the perimeter of disk microcavities. So this causes scattering loss reduction. In 2004, Kippenberg et al. (43) have reported the successful fabrication of silica disk microcavities. The WGM resonator mode and ultrahigh Q factors are achieved by measuring the parametric oscillation spectrum and the coupling-gap dependence of the parametric threshold. In September 2004, Kippenberg et al. (44) have reported the fabrication of the on-a-chip toroidal microcavities. The coupling and optical properties of ultrahigh Q factor are investigated by single mode Raman lasing or PL spectroscopy in a waveguide coupled WGM mode microcavity. The theoretical and experimental results of the Q factor, mode volume and waveguide loading are compared and discussed.

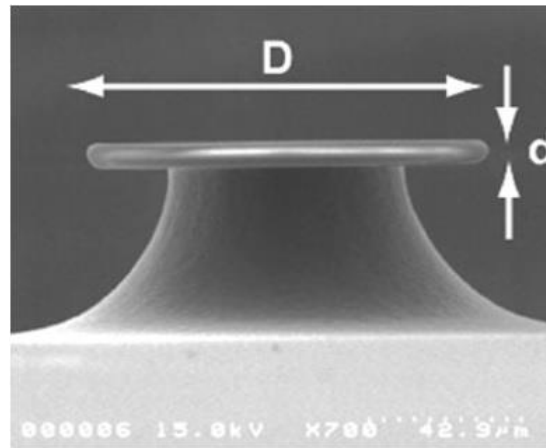


Figure 17 The SEM photograph of a toroid microcavity (44)

(c) Tubular Microcavities

The basic shape of tubular microcavity is shown in Figure 21 (b). It is designed to have a cylinder structure. Huang et al. (46) have fabricated the rolled-up SiO/SiO₂ tubular microcavity. The experimental and FDTD simulation for the optical resonant mode locations as a function of the distance confirm its optical properties. The low Q factor of about 100 is obtained for that work. Kipp et al. (47) have presented a InGaAs/GaAs tubular microcavity. The tube structure is rolled into a U-shape pattern. It consists of the microtube bridge and its bearing at both edge sides. The high Q factor of 3200 is for the mode at 1.204 eV. Later, Tian et al. (73) have reported the realization of single WGM in diamond tubular microcavity. The tube structure is designed with periodic hole arrays as shown in Figure 18. For the relevant calculation, the 3-dimensional (3D) structure is simplified by flattening into 2-dimensional (2D). This structure on 2D plane is a rectangle. The interior of the rectangle has a circle hole array. Recently, Wang et al. (48) have achieved a single WGM mode in mesh-structured tubular microcavity. The 3D structure is simplified by design in 2D. This structure in 2D plane is a rectangle. The interior of the considered rectangle has a square hole array. The results of simulated transmission spectra are confirmed by the measurement of experiential transmission spectra.

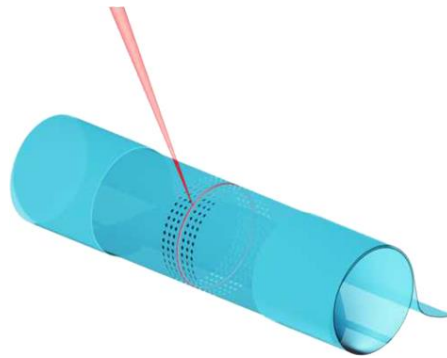


Figure 18 The structure of a single WGM tubular microcavity showing a periodic hole array (73)

(d) Bottle Microcavities

Sumetsky et al. (51) have reported the fabrication of hollow spherical microcavities by using stretching force in 2010. The two ends of microcapillaries are adjacent to the piezoelectric transducer (PZT) stages. The measured Q factor of resonant mode is obtained and it exceeds 10^6 . Afterwards, this structure is also named that optical bottle microcavities. In 2012, Ding et al. (49) have reported the fabrication of optical bottle microcavities from a standard telecom optical fiber. On the surface of the bottle microcavity, inscribed microgroove scars are created by focused ion beam milling process. Appropriate scaring position affects the selection of high Q WGM. Later, Sumetsky (50) has proposed an optical bottle microcavity as well as an anti-bottle microcavity. He has developed the simulations for the theory of slow acoustic modes being similar to the surface nanoscale axial photonics (SNAP) theory. It is found that the optical and acoustic resonant modes can be observed in bottle microcavity. But anti-bottle microcavity obtains only an acoustic mode as shown in Figure 19.

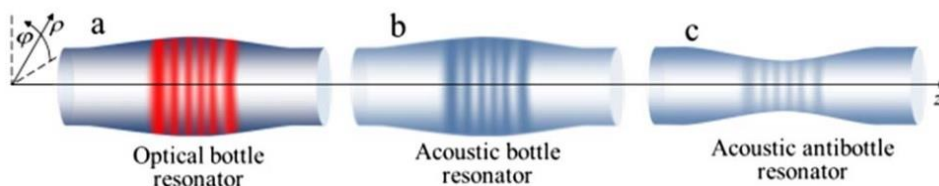


Figure 19 structure and optical characteristics of (a) optical bottle microcavity, (b) acoustic bottle microcavity, and (c) acoustic anti-bottle microcavity (50)

2.7 Fabrication Technique of Optical Microcavities

Optical microcavities can be fabricated by various techniques, e.g., melting and splicing of optical fibers, rolling-up mechanism of semiconductor bilayers, lithography and etching technologies, SNAP technology, UV-curable adhesive, self-assembly procedure, etc. In this section, a few techniques are reviewed.

(a) Melting and Splicing of Optical Fibers

Optical bottle microcavities can be fabricated from optical fibers. As the simplest techniques, the optical fiber at two sides is melted by using fire flame, fusion splicer or CO₂ laser for melting the optical fiber. Thus the center position between the two sides obtains a thick region. For demonstration, optical bottle microcavities (49) are fabricated from a standard optical fiber (Corning SMF28) by using both simultaneous softening and compressing of a fusion splicer. Ward et al. (53) have reported the fabrication of microcavities from optical fibers by using a CO₂ laser. A schematic of the fabrication sets up as shown in Figure 20. The dashed lines represent control lines or data transfer.

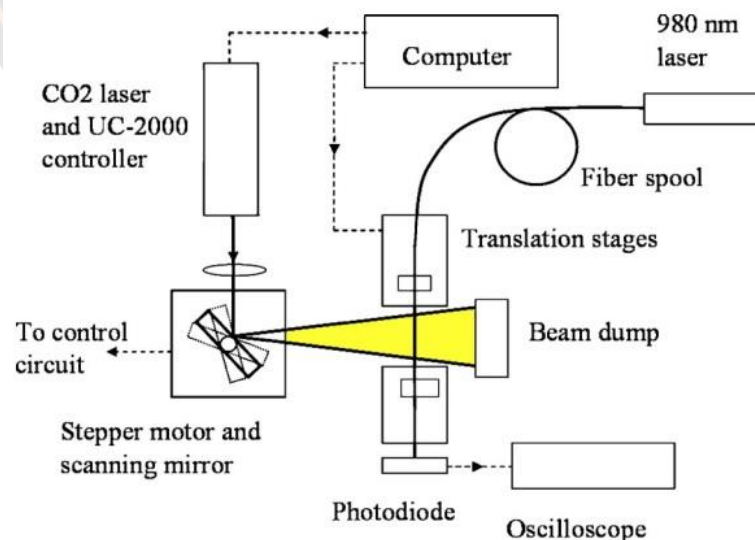


Figure 20 Schematic of the fabrication sets up by using a CO₂ laser. (53)

(b) Rolling-Up Mechanism of Semiconductor Bilayers

The fabricating process of rolled-up SiO/SiO₂ tubular microcavity (shown in Figure 21) (46) starts from the preparation of square or circular photoresist layer on Si wafer. The different sizes of square or circle can be defined by a standard photolithography. After e-beam evaporation, employing angled deposition can provide the SiO/SiO₂ bilayer on photoresist layer. The photoresist layer was selectively removed by using acetone. Then the active layer was released, and the intrinsic stress gradient occurs in the SiO/SiO₂ bilayer. The releasing of SiO/SiO₂ bilayer produces self-assembled rolling up mechanism. The structural shape is transformed into a tube. The rolled-up InGaAs/GaAs tubular microcavities (47) start from a shallow wet-chemical etching process into the In_{0.2}Ga_{0.8}As layer. Then, the edge is deeply etched to the AlAs sacrificial layer. Finally, the highly selective HF solution is applied to undercut the strained In_{0.2}Ga_{0.8}As layer. The strained mesa occurs. The self-rolling process occurs and the micro-tubular structure is accomplished. Diamond mesostructured microcavities (73) can also be fabricated by using this rolling-up mechanism.

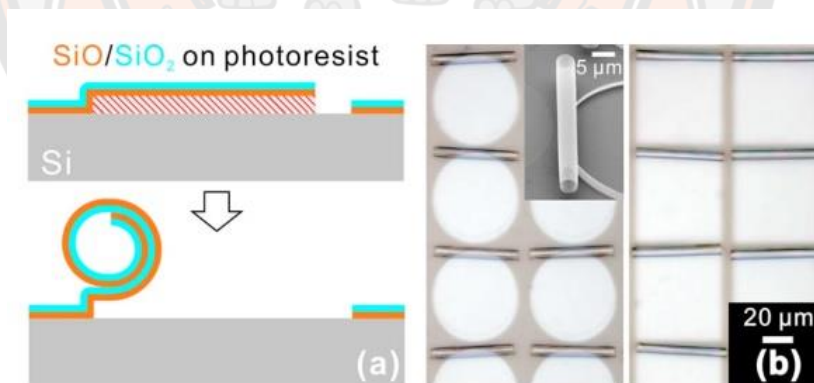


Figure 21 (a) structural diagram of fabricating process for rolled-up SiO/SiO₂ tubular microcavity and (b) SEM photograph of tubular microcavity arrays (46).

(c) Lithography and Etching Technologies

Lithography and etching technologies are used in fabrication microcavities such as optical lithography, etching technology (wet oxide and a dry etching), the standard i-line stepper lithography, single-step inductively coupled plasma reactive ion etching and the Nanoscribe 3D lithography system. For a research example, silica microdisk cavities (45) were produced by using optical lithography, wet oxide and dry etching technologies. Silicon wafer uses the standard lithography technology with circular photoresist pads. Then wet oxide etching is applied. The shape of obtained sample is a circular disk. This silica disk is then removed from the Si substrate by an isotropic dry etching. The hourglass-shaped Si microcavity arrays (shown in Figure 22) (54, 55) can be fabricated by using the standard i-line stepper lithography and ICP-RIE process. The mesh-structured microcavity (48) can also be fabricated by the Nanoscribe 3D lithography system. This new technology can create precise shapes and smooth surfaces. The detailed fabrication process by using this 3D Nanoscribe machine will be presented in chapter 3.

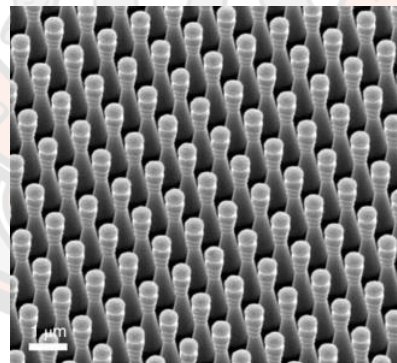


Figure 22 The SEM photograph of the hourglass-shaped silicon microcavity arrays (54)

2.8 Characterization of Optical Microcavities

Characterization of optical microcavities can be done in transmission mode or emission mode via PL spectroscopy. The details of each measurement are described in the next paragraphs.

(a) Transmission Spectrum

Transmission spectrum measurement (48) produces a transmission spectrum as a function of wavelengths by using a light coupling method. In the first process, the tapered optical fiber is prepared (by heating and stretching with 2 stepper motors on 2 ends). The tapered optical fiber is nearly vertically placed and the microcavity is in a 3D micro-locating system. The partial light can interact and couple with the sample through its evanescent field. This exhibits characteristic of optical microcavity. The light guided through the fiber is transformed to an electrical signal by a photodetector. The signal is recorded by a data acquisition card connected to a computer. Typical results of transmission spectra are shown in Figure 23. The WGMs of microcavities are observed as a series of discrete Lorentzian-shaped dips in transmission spectra. Both transmission spectra from experimental measurement and FDTD simulation are consistent and this confirms the correctness of the result.

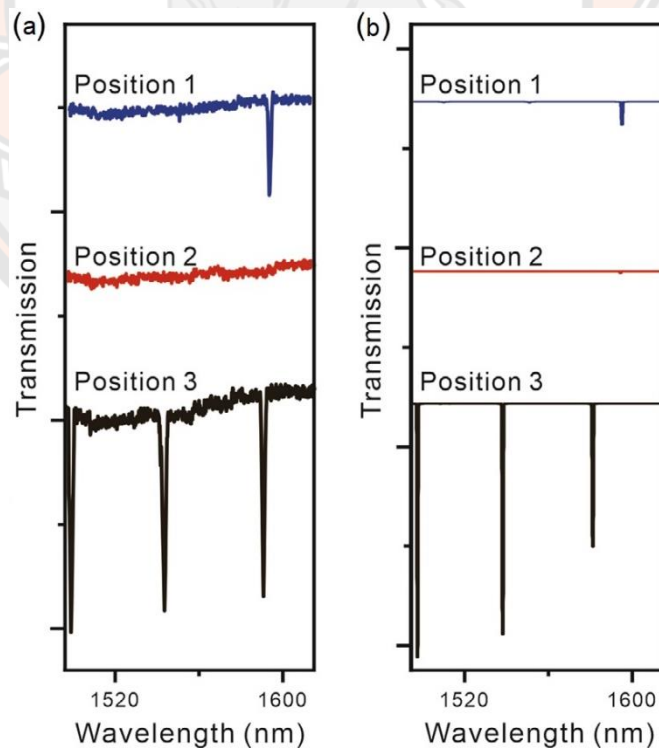


Figure 23 Transmission spectra at different axial positions obtain from (a) experimental measurement and (b) FDTD simulation (48).

(b) Photoluminescence (PL) measurements

Photoluminescence measurements of optical microcavities can reveal optical resonant modes (46). A micro-PL setup (56) as shown in Figure 24 consists of an xy -stage, a microscope, a 532-nm laser, a cooled Si detector, a cooled InGaAs detector, a variable laser attenuator and an optical fiber. The sample is placed in the cryostat on the xy stage. The 532-nm Nd:YVO₄ laser emits excitation light through the variable attenuator. The light goes through the microscope objective. The PL is excited and the PL light is filtered from the laser light by using a dichroic beam-splitter (BS). The emitted PL light can then be dispersed by a monochromator. A LN₂-cooled Si-CCD detector or a LN₂-cooled InGaAs array detector is used to detect the PL light, which transmitted through the optical fiber.

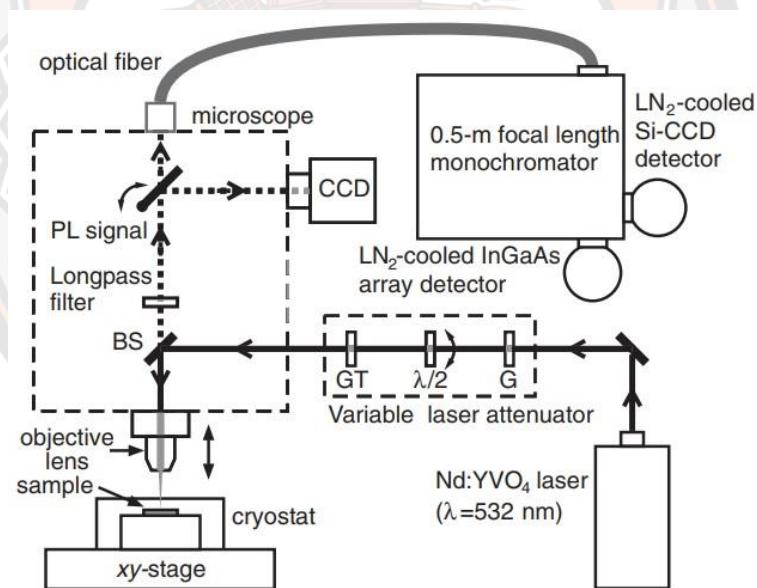


Figure 24 Schematic of the micro-PL setup (56)

Songmuang et al. (57) have used this micro-PL setup for the PL measurement. The result is reported in Figure 25. In that work, PL spectra at 8 K from SiO_x/Si microtube cavities with the diameters of 1.04 μm and 2.2 μm are studied. The PL spectra show the light intensity as a function of the energy of emitting photons from the microtubes. These SiO_x/Si microtube cavities obviously contain resonant modes.

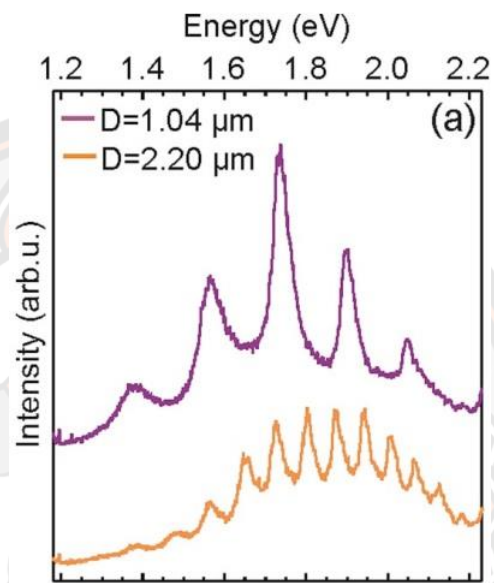


Figure 25 PL spectrum at 8 K of a single SiO_x/Si microtube cavities (57)

CHAPTER III

RESEARCH PROCEDURES OF THE STUDY

These QD structures and optical microcavity are our interesting photonic structures. Investigation of these structures might be used to improve the efficiency of hybrid QD solar cells. In this work, the investigated hybrid QD solar cells have 3 structures (i.e., 3 samples). The sample characteristic measurement and the circuit parameter extraction method for DC and AC circuit parameters are presented for the investigated QD structures. Finally, the photonic structures of hollow cylindrical and hyperboloidal optical microcavities are presented. Procedures of the FDTD simulation and fabrication technique for optical microcavities are described.

3.1 Structure of Hybrid InAs/GaAs and GaSb/GaAs Quantum-Dot Solar Cells

The variously designed QD structures in hybrid InAs/GaAs and GaSb/GaAs QD solar cells are our first interesting photonic structures. Investigated structures of hybrid InAs/GaAs and GaSb/GaAs QD solar cells are 1-pair of type-A QD solar cell, 3-pair of type-A QD solar cell and 1-pair of type-B QD solar cell (26, 58). The structures of hybrid QD solar cells are shown in Figures 26-28. All investigated hybrid QD solar cells were fabricated by using MBE growth technique. Details of the sample fabrication have been presented elsewhere (26, 58).

(a) Structure for 1-Pair of Type-A Hybrid QD Solar Cell

The structure and photo of 1-pair type-A hybrid QD solar cell are shown in Figure 26. It is one pair of GaSb/GaAs QD and InAs/GaAs QD layers. First, a p-type GaAs (001) substrate surface is prepared by thermal desorption of oxide layer. A buffer layer is grown and it is a 300-nm-thick GaAs layer. After that the QDs are grown in the SK mode of epitaxial growth by the mechanism of strain relaxation. Type-A hybrid QDs are from the deposition of the self-assembled InAs QDs on the buffer layer. Then 150-nm-thick GaAs is grown to cover InAs QDs as the capping layer. Next, the first GaAs capping layer is overgrown with a layer of self-assembled

GaSb QDs and then 150-nm-thick GaAs is grown to cover the GaSb QDs and it acts as the second capping layer. This structure is a pair of type-A hybrid QDs. For the top/contact layer, the n-GaAs is grown for 300 nm thick. Finally, the formation of AuGa/Ni and AuZn contacts are fabricated by metal evaporation in a separated thermal evaporator.

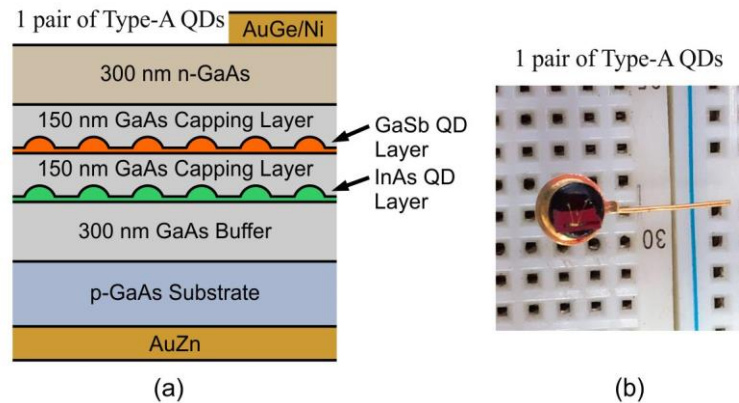


Figure 26 (a) Schematic and (b) photo of type-A hybrid QD solar cell sample having 1-pair of stacked GaSb/GaAs QD and InAs/GaAs QD layers.

(b) Structure for 3-pair of Type-A Hybrid QD Solar Cell

The schematic and photo of 3-pair type-A hybrid QD solar cell are shown in Figure 27. The structure has 3 pairs of type-A hybrid QDs grown by stacking 3 pairs of GaSb/GaAs QD and InAs/GaAs QD layers. A p-type GaAs (001) substrate is first prepared. A 300-nm-thick GaAs buffer layer is grown. Then 3 pairs of type-A hybrid QDs are deposited in MBE. As the next layer, an n-GaAs (300-nm-thick) is grown. Finally, front and back contacts are fabricated by the evaporation of AuGa/Ni and AuZn.

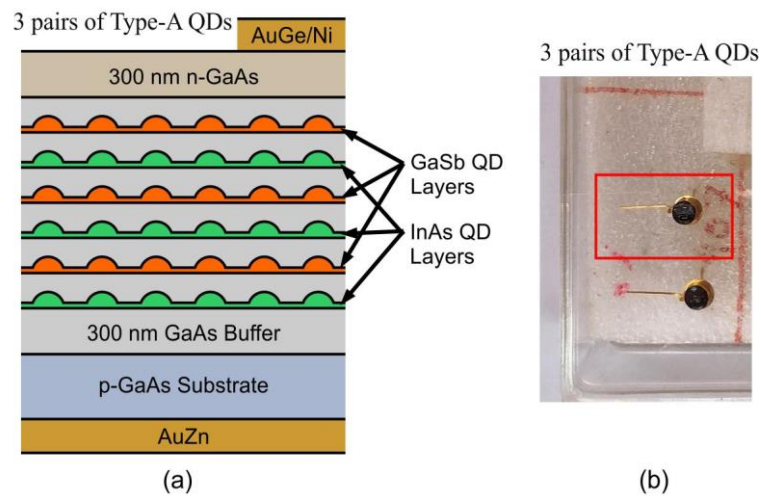


Figure 27 (a) Schematic and (b) photo of type-A hybrid QD solar cell sample having 3 pairs of stacked GaSb/GaAs QD and InAs/GaAs QD layers.

(c) Structure for 1-Pair of Type-B Hybrid Quantum-Dot Solar Cell

The schematic and photo of 1-pair type-B hybrid QD solar cell are shown in Figure 28. The structure was grown on a p-type GaAs (001) substrate and 300-nm-thick n-GaAs layer. A 300-nm-thick GaAs is grown as the buffer layer. After that, the QDs are grown in the SK mode of epitaxial growth by the mechanism of strain relaxation. Type-B QDs are from the deposition of the self-assembled GaSb QDs. Then 150-nm-thick GaAs is grown to cover GaSb QDs as it is the capping layer. Next, the GaAs capping layer is overgrown with a layer of self-assembled InAs QDs and then a 150-nm-thick GaAs is grown to cover InAs QDs as the second GaAs capping layer. This structure is 1-pair type-B hybrid QDs. The top/contact layer is the n-GaAs. Finally, the formation of AuGa/Ni and AuZn contacts is fabricated by the similar metal evaporation.

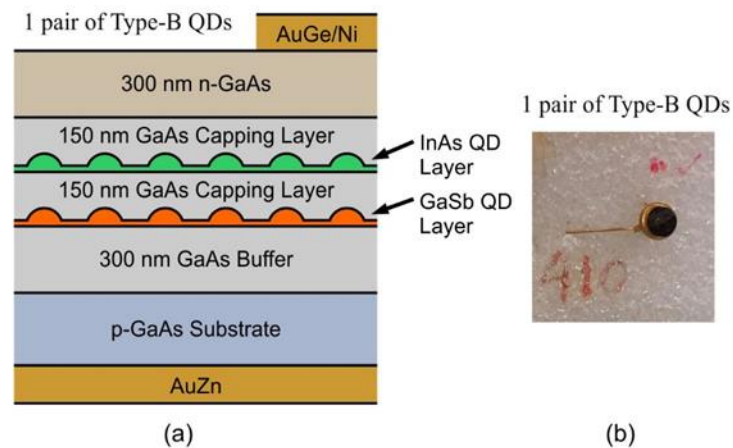


Figure 28 (a) Schematic and (b) photo of type-B hybrid QD solar cell sample having 1 pair of InAs/GaAs QD and GaSb/GaAs QD layers.

3.2 Sample Characterization

Two characterization methods are applied in this work. The first method is the current-voltage characteristic or DC characteristic. The second characterization method is the frequency response or AC characteristic. The details of the measurement setup and the applied AC and DC equivalent circuit models are described as follows.

3.2.1 Current - Voltage Characteristics

(a) Measurement for current - voltage characteristics

The experimental setup of current-voltage characteristic measurement is shown in Figure 29. Equipment of experimental setup includes:

1. Agilent E3633A and Agilent E3642A DC power supplies as voltage sources
2. Keithley 6485 picoammeter as an ammeter
3. Agilent 34401A Digital multimeter as a voltmeter
4. Discrete resistor R , which is connected to the sample
5. Tungsten lamp for illuminating light on the sample
6. The sample, which is the hybrid QD solar cell (in the box).

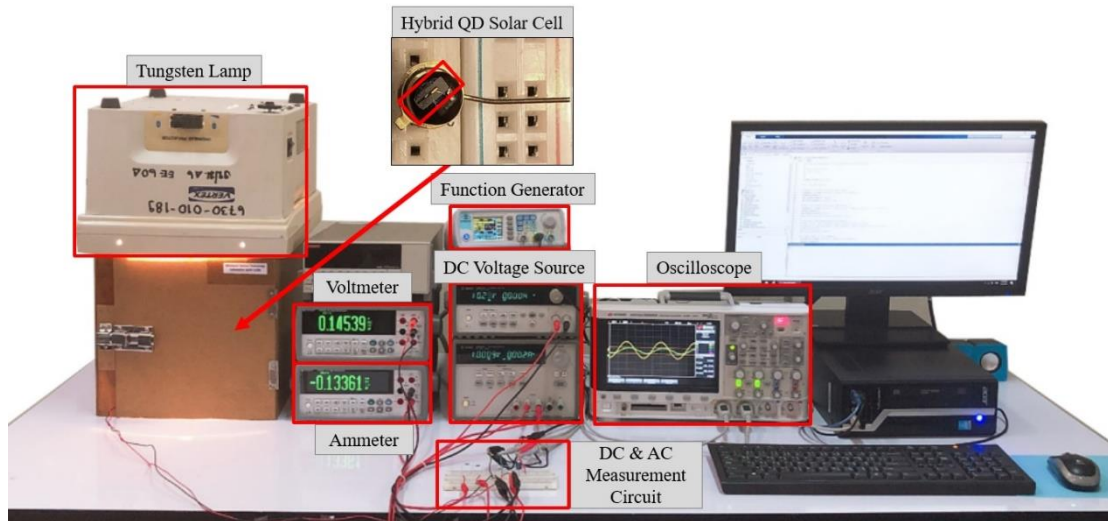


Figure 29 Experimental setup

The measurement circuit and DC equivalent circuit model of the QD solar cell are shown in Figure 30. The measurement circuit for DC characteristic is the series-connection between DC biased circuit and hybrid QD solar cell. The dashed-box in Figure 30 represents DC biased circuit. It is a series-connection between DC biased voltage source $v_{S,DC}$ and a series resistor $R_{S,DC}$. The resistor $R_{S,DC}$ value is fixed at $1 \text{ k}\Omega \pm 1\%$. The DC biased voltage source $v_{S,DC}$ is the series-connection between Agilent E3633A and Agilent E3642A DC power supplies. The connection is done in order to be able to vary the DC biased voltage $v_{S,DC}$ from -10 to 10 V without any interruption of the measurement. The Keithley 6485 picoammeter acts as an ammeter and uses for current measurement. The Agilent 34401A digital multimeter acts as a voltmeter and is used for voltage measurement. For illuminating the sample, the light from 300-W tungsten lamp is stably applied to the sample in the box.

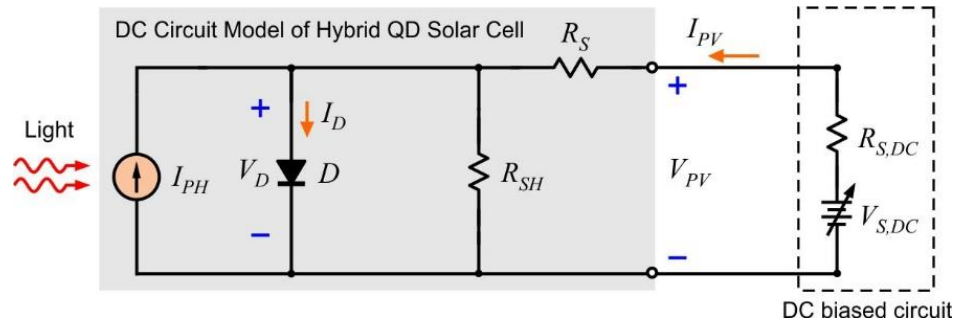


Figure 30 Measurement circuit of obtaining current - voltage characteristic and the DC equivalent circuit model of hybrid QD solar cell.

(b) DC equivalent circuit model of hybrid QD solar cell

The DC equivalent circuit of hybrid QD solar cell (59-64, 4.1) is shown in the shaded area of Figure 30. The diode D represents the p-n junction. The photocurrent source I_{PH} is shunted with the p-n junction diode D and the shunt resistance R_{SH} . Next, the series resistance R_S is series-connected with this circuit. This R_S represents the contact resistance and the resistance of semiconductor materials. The DC equivalent circuit of hybrid QD solar cell can be explained as follows. When the incident light is absorbed in the p-n junction, electron-hole pairs are produced. Then potential difference is created across the p-n junction. A Phenomenon of photovoltaic effect appears when charge carriers flow through the p-n junction to the external circuit. The result of this incidence is the observable photocurrent I_{PH} . Photo-generated carriers should mostly flow to the external circuit. However, a small portion of the photo-generated carriers can flow into some defects. These effects can be represented by the shunt resistance R_{SH} . In fact, hybrid QD solar cell also has a resistance in semiconductor materials as well as a contact resistance. These resistances are represented by the series resistance R_S .

3.2.2 Frequency responses

(a) Measurement of frequency responses

The experimental setup for the frequency response measurement is shown in Figure 29. Equipment for this experimental setup includes:

1. Agilent E3633A and Agilent E3642A DC power supplies as voltage sources.
2. Keithley 6485 picoammeter as an ammeter.
3. Agilent 34401A Digital multimeter as a voltmeter.
4. Function generator (sinusoidal waveform generator) as an AC voltage source.
5. Oscilloscope (Agilent MSO-X 2004A) is used to measure the AC voltage signals.
6. Discrete resistors and capacitor for connecting to the sample
7. Tungsten lamp for illuminating light on the sample.
8. The sample, which is the hybrid QD solar cell (in the box).

The measurement circuit and the setup for the frequency response (AC characteristic) measurement are shown in Figure 31 (64). The measurement circuit for AC characteristic is the parallel-connection of the AC biased circuit, the DC biased circuit and the hybrid QD solar cell. Circuit elements in the dotted rectangle represent the DC biased circuit. This DC biased circuit is similar to the previously mentioned circuit. The dotted rectangle in Figure 31 marks the AC biased circuit. The AC biased voltage source $v_{S,AC}$ is series-connected with a capacitor $C_{S,AC}$ and a resistor $R_{S,AC}$ within the AC biased circuit. For determination of these circuit parameters, fixed values of $R_{S,AC}$ and $C_{S,AC}$ (500- Ω and 470 μ F) are applied. The amplitude of AC voltage source (from the function generator) is fixed at 0.25 V and AC voltage source is sinusoidal voltage while the frequency is varied between 1 kHz - 1 MHz. A multichannel oscilloscope (Agilent MSO-X 2004A) is used to measure the AC voltage signals as time function. Channel 1 of Agilent MSO-X 2004A oscilloscope measures AC biased voltage $v_{S,AC}$. The AC signal is set as AC sinusoidal voltage $v_{S,AC} = A_{in} \sin(2\pi ft)$. The amplitude of input voltage A_{in} is fixed as 0.25 V. The second channel of the oscilloscope measures the solar-cell voltage v_{PV} . The voltage signal of

hybrid QD solar cell v_{PV} is in the form of $v_{PV} = A_{out} \sin(2\pi ft + \phi)$, where A_{out} is the amplitude of output voltage, ϕ is the phase difference and f is the frequency.

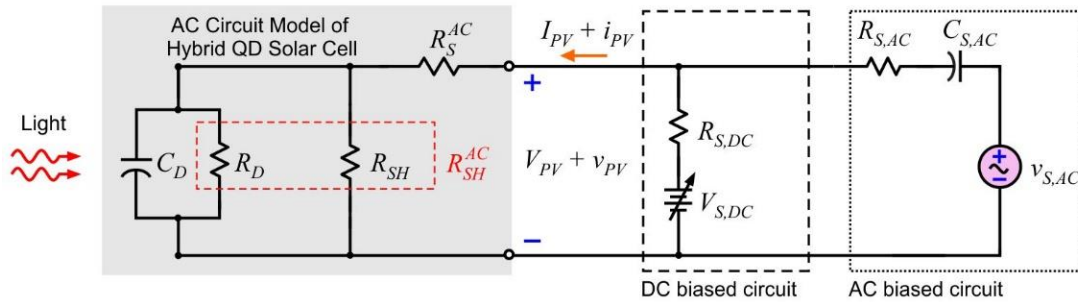


Figure 31 Measurement circuit for extracting frequency response and AC equivalent circuit model of hybrid QD solar cell.

(b) AC equivalent circuit model of hybrid QD solar cell

AC equivalent circuit of hybrid QD solar cell is presented in shaded area of Figure 31. The AC analysis is considered for obtaining this circuit. For steady state light illumination, the photocurrent source I_{PH} becomes an open circuit. The p-n junction diode D is replaced with the AC diode capacitance of hybrid QD solar cell C_D paralleled with the AC diode resistance R_D . The DC biased source $V_{S,DC}$ and the capacitance of AC biased source $C_{S,AC}$ become short circuit. Therefore, the AC equivalent circuit of hybrid QD solar cell composes of the parallel connection between the AC diode capacitance C_D , the AC diode resistance R_D and the AC shunt resistance R_{SH}^{AC} . The AC series resistance R_S^{AC} is series-connected with this AC circuit.

3.3 Method for Optimal DC and AC Parameter Extraction

After the measurement of the hybrid QD solar cells, the results of current-voltage characteristics and frequency responses are obtained. Those measurement results are brought to extract DC and AC parameters. These below paragraphs explicate method for optimal DC and AC parameter extraction.

3.3.1 Extracted Method for the DC Circuit Parameters

In order to extract the DC circuit parameters from the applied DC equivalent circuit model and the current-voltage characteristics. We use *lsqcurvefit* function in MATLAB optimization toolbox to find the solution (65). The *lsqcurvefit* function is used by base on Levenberg-Marquardt algorithm and trust region reflective method. Extracted procedure (shown in Figure 32) for the DC circuit parameters is as follows.

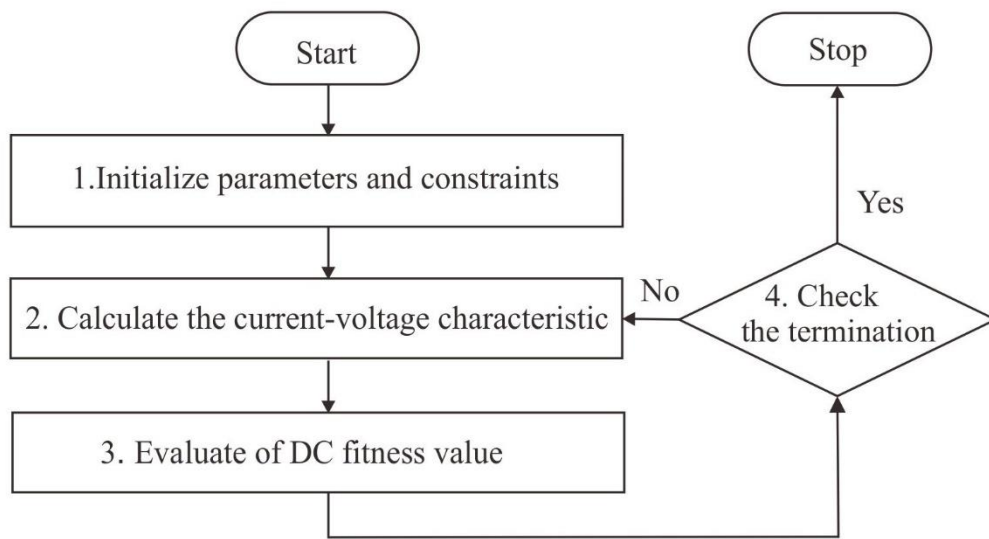


Figure 32 Diagram showing the procedure for the DC circuit parameter extraction.

1. Initialize parameters and constraints

Initial values of the reverse saturation current I_o , the diode ideality factor n , the photocurrent I_{PH} , the DC series resistance R_S and the DC shunt resistance R_{SH} are set. Constraints of these 5 fitting parameters are as follows:

$10 \text{ nA} \leq I_o \leq 1 \text{ mA}$, $1 \leq n \leq 2$, $10 \text{ nA} \leq I_{PH} \leq 1 \text{ mA}$, $0 \leq R_S \leq 5 \text{ k}\Omega$, and $100 \Omega \leq R_{SH} \leq 0.1 \text{ M}\Omega$.

2. Calculate the current-voltage characteristic from the set parameters

The DC equivalent circuit of hybrid QD solar cell is shown in Figure 30 The p-n junction diode current I_D can be calculated from $I_D = I_o (\exp(qV_D / nkT) - 1)$ of the Shockley diode equation. The current-voltage characteristics of hybrid QD solar cell

can relate with Equation (2.4). Since the current I_{PV} and the voltage V_{PV} of hybrid QD solar cell are related in a complicated function as shown in Equation (2.4). This work uses Lambert W function in writing the closed-form solution. The new equations of solar cell current are rearranged as follows:

From DC equivalent circuit model in Figure 30 is used Kirchhoff's current law (KCL).

$$-I_{PV} - I_{PH} + I_o (e^{(V_{PV} - R_S I_{PV}) / nV_T} - 1) + \frac{V_{PV} - R_S I_{PV}}{R_{SH}} = 0$$

The equation is new rearranged.

$$I_{PV} = \frac{I_o e^{V_{PV} / nV_T}}{(1 + R_S / R_{SH})} (e^{(-R_S I_{PV}) / nV_T}) + \frac{V_{PV} - R_{SH} (I_{PV} + I_o)}{R_{SH} + R_S} = 0$$

$$I_{PV} - \frac{V_{PV} - R_{SH} (I_{PV} + I_o)}{R_{SH} + R_S} = \left(\frac{I_o}{1 + R_S / R_{SH}} e^{V_{PV} / nV_T} \right) (e^{(-R_S I_{PV}) / nV_T})$$

The above equation is multiplied with $(R_S / nV_T) e^{R_S / nV_T \left(I_{PV} - \frac{V_{PV} - R_{SH} (I_{PV} + I_o)}{R_{SH} + R_S} \right)}$.

$$\begin{aligned} & \frac{R_S}{nV_T} \left[I_{PV} - \frac{V_{PV} - R_{SH} (I_{PV} + I_o)}{R_{SH} + R_S} \right] \exp \left[\frac{R_S}{nV_T} \left(I_{PV} - \frac{V_{PV} - R_{SH} (I_{PV} + I_o)}{R_{SH} + R_S} \right) \right] \\ &= \frac{R_{SH} I_o / nV_T}{1 + R_S / R_{SH}} \exp \left(\frac{V_{PV}}{nV_T} \right) \exp \left(\frac{-R_S}{nV_T} \right) \left(\frac{V_{PV} - R_{SH} (I_{PV} + I_o)}{R_{SH} + R_S} \right) \end{aligned}$$

The Lambert W function is used in rearrangement for new equation. It is defined by $W(x) \exp(W(x)) = x$. Thus the current-voltage characteristics (61, 62) of the hybrid QD solar cell can be expressed by Equation (3.1).

$$\begin{aligned} I_{PV} = & \frac{1}{R_S} \frac{nkT}{q} W \left(\frac{q}{nkT} \frac{I_o R_S}{(1 + R_S / R_{SH})} \exp \left(\frac{q}{nkT} \frac{V_{PV} + R_S (I_o + I_{PH})}{(1 + R_S / R_{SH})} \right) \right), \\ & + \frac{V_{PV} / R_{SH} - (I_o + I_{PH})}{1 + R_S / R_{SH}} \end{aligned} \quad (3.1)$$

3. Evaluate of DC fitness value

The DC fitness value F_{DC} for DC parameter extraction is obtained from the objective function. This function of DC fitness value is the sum of square error between experimentally measured current $I_{PV,exp}^i$ and calculated current $I_{PV,cal}^i$ of hybrid QD solar cell for each data point I ($i = 1, 2, \dots, N$, where N represents the total number of I - V data points). The DC fitness value can be calculated from Equation (3.2). The current-voltage characteristic is fitted by using the *lsqcurvefit* function in MATLAB optimization toolbox to minimize this fitness value.

$$F_{DC} = \min \sum_{i=1}^N \left(I_{PV,exp}^i - I_{PV,cal}^i \right)^2 \quad (3.2)$$

4. Check for the termination and stop the fitting process

When DC fitness value reaches the minimal value, the process of I - V curve fitting is stopped. The extracted parameters from this I - V curve fitting are the diode ideality factor n , the reverse saturation current I_0 , the photocurrent I_{PH} , the DC shunt resistance R_{SH} and the DC series resistance R_S .

3.3.2 Extracted Method for the AC Circuit Parameters

In order to extract the AC circuit parameters from frequency responses and AC circuit of hybrid QD solar cell. This thesis uses the *lsqcurvefit* function in MATLAB optimization toolbox for searching the solution. The procedure (shown in Figure 33) for the AC circuit parameter extraction is as follows.

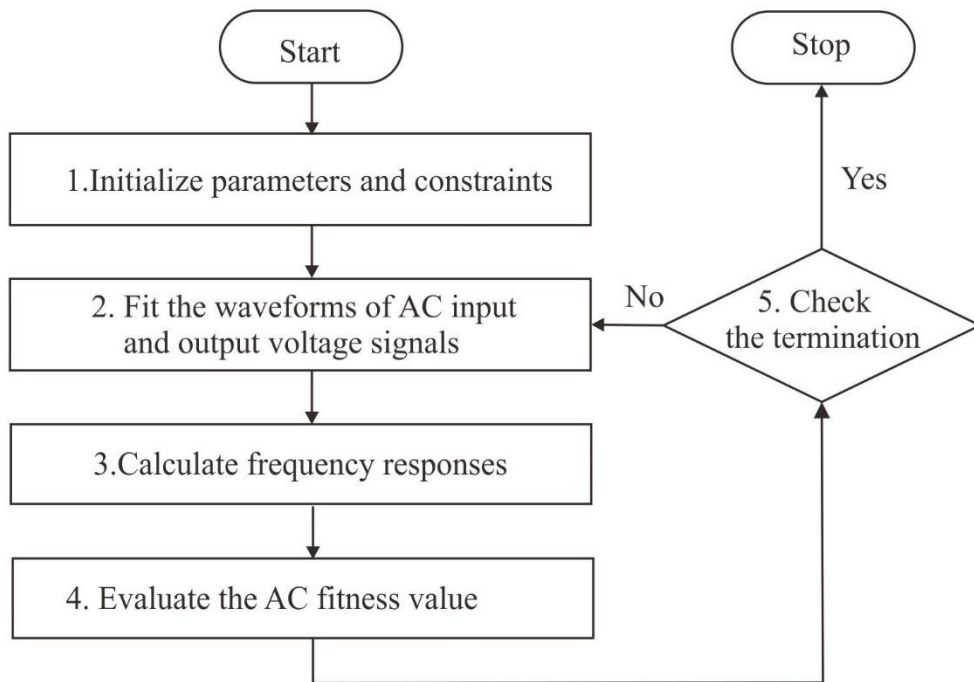


Figure 33 Diagram showing the procedure for the AC circuit parameter extraction.

1. Initialize parameters and constraints

The initial values and constraints of the series capacitance C_D , the AC shunt resistance R_{SH}^{AC} , the AC series resistance R_S^{AC} and the AC diode resistance R_D are set for the fitting.

2. Fit the waveforms of AC input and output voltage signals

The AC voltage signals are measured in frequency range f between 1 kHz and 1 MHz. Waveforms of AC input and output voltage signals are recorded and fitted. The output voltage amplitude A_{out} , the input voltage amplitude A_{in} and the phase difference ϕ are extracted.

The extracted parameter of input voltage signal is the input voltage amplitude A_{in} . It is obtained from the fitting the recorded data with Equation (3.3)

$$v_{S,AC} = A_{in} \sin(2\pi ft) \quad (3.3)$$

The extracted parameters of output voltage signal are the output voltage amplitude A_{out} and the phase difference ϕ . They are obtained from the fitting with Equation (3.4)

$$v_{PV} = A_{out} \sin(2\pi ft + \phi), \quad (3.4)$$

where A_{out} is the amplitude of output voltage, ϕ is the phase difference and f is the signal frequency.

3. Calculate frequency responses of hybrid QD solar cells

The frequency response curve is the amplitude ratio A_{out}/A_{in} (in the unit of dB) versus frequency f (Hz) in log scale. The AC parameters are extracted from the fitting of this frequency response. From the AC equivalent circuit, the amplitude ratio A_{out}/A_{in} (dB) is calculated from the AC circuit by the voltage divider rule:

$$\frac{A_{in}}{A_{out}} = \left| \frac{Z_{in}}{Z_{in} + Z_{out}} \right|,$$

where $Z_{in} = \left(\frac{R_{SH}^{AC}}{1 + 2\pi j f C_D R_{SH}^{AC}} \right) + R_S^{AC}$ and $Z_{out} = R_{S,AC}$

Note that the Z_{in} is the total impedance of input side. It is first calculated from parallel connection of the AC shunt resistance R_{SH}^{AC} and the AC diode capacitance C_D . Then result is serially connected with the AC series resistance R_S^{AC} . The AC shunt resistance R_{SH}^{AC} is the parallel connection of the AC diode resistance R_D and the DC shunt resistance R_{SH} . The Z_{out} is total impedance of output side. Since it has only $R_{S,AC}$, the Z_{out} is equal to $R_{S,AC}$. Thus the amplitude ratio A_{out}/A_{in} (dB) can be expressed as Equation. (3.5)

$$\frac{A_{in}}{A_{out}} \text{ (in dB)} = 20 \log \left| \frac{\left(\frac{R_{SH}^{AC}}{1 + 2\pi j f C_D R_{SH}^{AC}} \right) + R_S^{AC}}{R_{S,AC} + \left(\frac{R_{SH}^{AC}}{1 + 2\pi j f C_D R_{SH}^{AC}} \right) + R_S^{AC}} \right|. \quad (3.5)$$

4. Evaluate the AC fitness value

The objective function of AC fitness F_{AC} value is the sum of square error between experimentally measured amplitude ratio $A_{out,exp}/A_{in,exp}$ and calculated amplitude ratio $A_{out,cal}/A_{in,cal}$ for each data point i ($i = 1, 2, \dots, M$, where M is the total number of data points). Evaluation of AC fitness value can be calculated from

Equation (3.6). The frequency response is fitted by using the *lsqcurvefit* function in the MATLAB optimization toolbox (65).

$$F_{AC} = \min \sum_{i=1}^M \left(\frac{A_{in,exp}}{A_{out,exp}} (\text{in dB}) - \frac{A_{in,cal}}{A_{out,cal}} (\text{in dB}) \right)^2 \quad (3.6)$$

5. Check for the termination and stop the fitting process

After the AC fitness value reaches a minimal value, the fitting process of frequency response curve is stopped. The AC extracted parameters from this fitting are the AC diode capacitance C_D , the AC shunt resistance R_{SH}^{AC} , the AC series resistance R_S^{AC} and the AC diode resistance R_D .

3.4 Hollow Optical Microcavities

The secondly interesting photonic structure is the optical microcavity. The structure could be utilized for the surface coating on a solar cell in order to enhance its efficiency. The hollow cylindrical and hyperboloidal optical microcavities are the designed structures. Procedures of the FDTD simulation and fabrication technique for optical microcavities are explained in detail in this chapter.

3.4.1 Structure of hollow optical microcavities

The photonic structures of hollow optical microcavities are studied in this work. The designed structures are hollow cylindrical microcavities and hollow hyperboloidal microcavities. The structure details are as follows:

(a) Hollow cylindrical microcavities

The firstly designed structure of optical microcavity is a hollow cylindrical microcavity. The 3D structure of the investigated hollow cylindrical microcavity is shown in Figure 34 (a). The 3-dimensional (3D) of hollow cylindrical structure is simplified by design and analysis in planar domain (or 2D) with finite-difference time-domain (FDTD) simulation. The simplified 2D domain of hollow cylindrical structure is shown in Figure 34 (b). Designed parameters of the hollow cylindrical

optical microcavity are the hole radius r , the hole period a , the waveguide width or the width of missing hole line w , the number of column holes N along x -direction and the number of row holes M along y -direction. Cylindrical diameter D in 3D transforms to lateral length L in 2D structure. This length in planar domain is calculated from the circumference of 3D cross-section ($L = \pi D$). Thus, the product of the hole period a and the number of hole column N is the lateral length L . This hole period a is the distance between the center point of first hole to center point of next/nearby hole. Dashed squares in the figure represent the unit cell size ($a \times a$) of square hole array. In a typical design, the width of missing hole line w equals hole period a . The hole radius r is fixed at $0.25a$. The numbers of hole columns N and rows M are designed to be 20 and 3, respectively. Simulation resolution is fixed at $a/32$. Red arrows in both figures represent propagation directions of the considered wave.

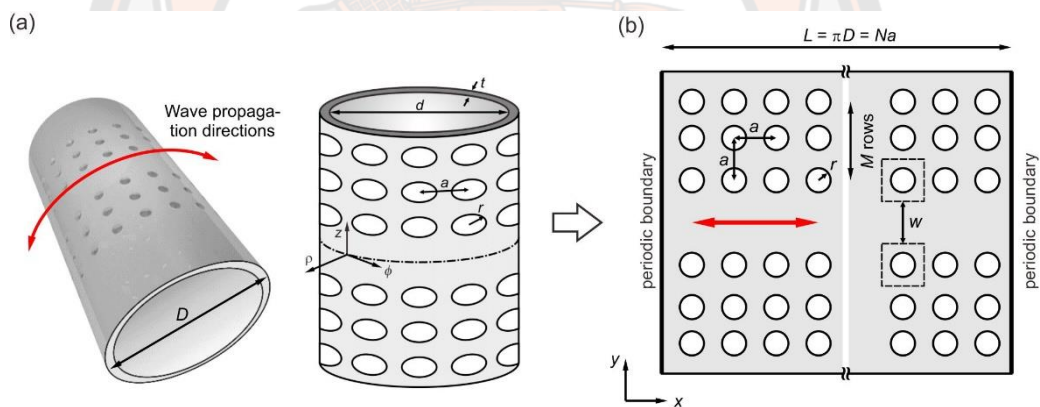


Figure 34 (a) The 3D structure and (b) the simplified 2D structure of the investigated hollow cylindrical optical microcavity.

(b) Hollow hyperboloidal microcavities

The second designed structures of optical microcavities are hollow hyperboloid microcavities. This new shape is also named as anti-bottle resonator. The hollow hyperboloidal structure is designed by using Describe 2.1 software (66-68) (shown in Figure 35). Spiral surface of hyperboloid structures are fabricated from the adapted hyperboloidal helicoid equation as Equation (3.7). The base hyperboloidal helicoid equation is taken from (66). The equation for this point-by-point structural fabrication can be rewritten as

$$\begin{aligned}
x_{t+1} &= p \sqrt{\frac{L_{h,t+1}^2}{q^2} + (1 \cdot T_{h,t+1})} \cdot \cos \frac{L_{h,t+1}}{c} + \Delta x \\
y_{t+1} &= p \sqrt{\frac{L_{h,t+1}^2}{q^2} + (1 \cdot T_{h,t+1})} \cdot \sin \frac{L_{h,t+1}}{c} + \Delta y \\
z_{t+1} &= c \cdot \Delta L_h
\end{aligned} \tag{3.7}$$

The height H (see Figure 35 (b)) is the quotient of spiral line length per positive number c (L_h / c). The spiral line length L_h is set from $-\frac{L_h}{2}$ to $\frac{L_h}{2}$ because our design has center at position (0,0). The spiral line length at time $t+1$ is the sum between $L_{h,t}$ and ΔL ($L_{h,t+1} = L_{h,t} + \Delta L$). Thickness of hollow hyperboloid microcavity $T_{h,t+1}$ at time $t+1$ is the sum between $T_{h,t}$ and ΔT ($T_{h,t+1} = T_{h,t} + \Delta T$). The x_{t+1} , y_{t+1} and z_{t+1} are position x , position y and position z at time $t+1$, respectively. x_0 and y_0 are initial positions. In order to set only positive position value. H is height. t is iteration. L_h is the length of spiral line. The ΔL_h is the difference value between spiral line length $L_{h,t+1}$ at time $t+1$ and spiral line length $L_{h,t}$ at time t . p , q and c are positive numbers. T_h , $T_{h,\min}$, $T_{h,\max}$ and $T_{h,Line}$ are thickness, the thickness value at lower boundary (inner radius), thickness value at upper boundary (outer radius) of hyperboloidal microcavities, respectively. For the sake of clarity, we typically set the thickness of a spiral line $T_{h,Line}$ to $0.15 \mu\text{m}$.

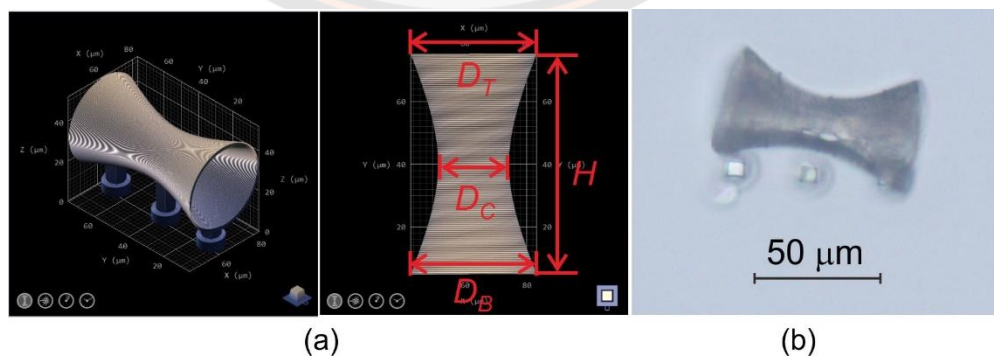


Figure 35 (a) The 3D structure and (b) the microscope photo of the hollow symmetrical hyperboloid microcavity.

The designed structure and microscope photo of symmetrical hyperboloid microcavity are shown in Figures 3.10 (a) and (b), respectively. A symmetrical hyperboloidal microcavity has the bottom diameter D_b of 40 μm , the central diameter D_c of 20 μm and the top diameter D_t of 40 μm . The thickness T_h and the height H are designed to be 1.2 and 70 μm .

3.4.2 Finite-difference time-domain (FDTD) simulation

Finite-difference time-domain (FDTD) (70) simulation is done by using MEEP software package (71). MEEP is an open-source software package developed at MIT to model electromagnetic systems. A normalized unit is used throughout this work (72).

Since the dimensional system of hollow cylindrical optical microcavity is reduced from 3D to 2D, the propagation directions and corresponding wave fields become planar (They are confined in 2D plane). Radiative loss is neglected when both refractive index is a high value and the curvature is small. The material parameters have been selected according to the experimental work (73). The index of cavity can be presented by an effective index for this 2D simulation. The effective index is set to 2.0 and the index of air hole is set at 1.0. The hole period a is the natural length. The characteristic frequency unit of c/a presents frequency scale where $c = 3 \times 10^8$ m/s. Typical hole period a is set at 320 to 400 nm and typical resonant wavelength is between visible and near-IR ranges (73).

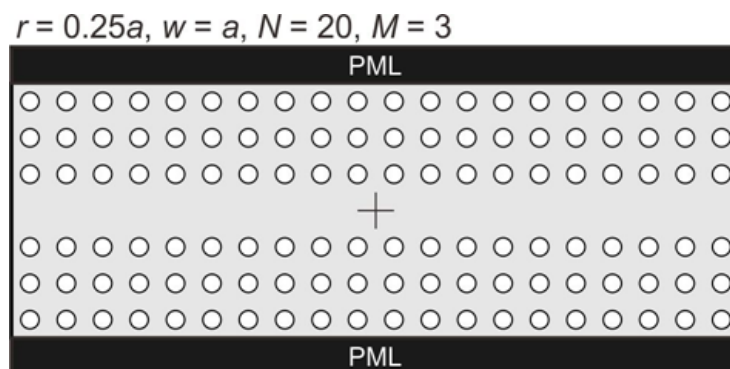


Figure 36 Simulation domain for low Q modes. The Hz dipole source and monitoring point are marked as a cross.

The initial structure of the simulation domain is shown in Figure 36. The H_z dipole source and monitoring point are marked as a cross in this figure. A perfectly matched layer (PML) of the thickness is applied to be an artificial absorbing layer to simulate problems in FDTD simulation. The absorbing boundary condition is used for escaping waves while the periodic boundary condition is used for the confining waves. A Gaussian pulse at single frequency with narrow frequency width Δf is used to excite the optical field. The frequency width Δf is equal to $0.01 (c/a)$ and its center is set at about the single mode resonant frequency f_c .

Typical structural parameters are shown in Figure 36. The hole radius r is set at $0.25a$. The hole numbers along column N and hole numbers along row M are set 20 and 3, respectively. The mode index m is set to 20. Only a polarized mode (74) is interesting in thin wall of the hollow cavity. The polarized mode with the perpendicular magnetic field H_z , electric fields E_x and E_y in plane along x and y direction is considered. After the simulation, the resonant mode fields of hollow cylindrical optical microcavities are extracted. The perpendicular magnetic field H_z , electric fields E_x and E_y are obtained after the significant pulse decays. The field profiles are recorded and then the simulation stops. The structural parameters are varied in each FDTD simulation. After that, the single resonant frequency f_c and the Q factor are extracted by using harmonic inversion routine implemented in MEEP.

3.4.3 Fabrication of hollow microcavity by the photonic professional GT DLW system

The photonic professional GT DLW system (67-69) and Describe 2.1 software are used for 3D constructing in complex nanometric structures. The components of the photonic professional GT DLW system are shown in Figure 37.

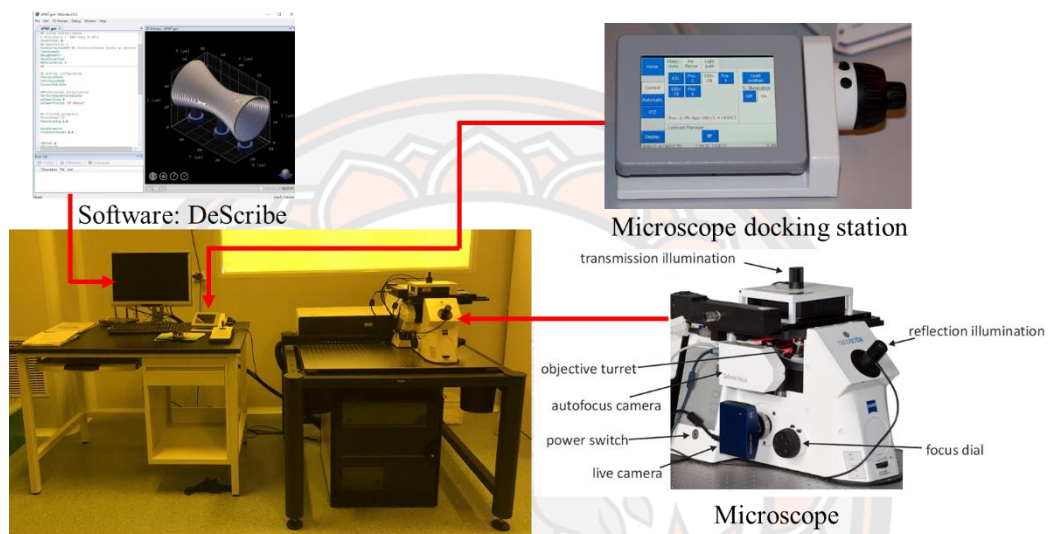


Figure 37 The photonic professional GT DLW system

The first step is the sample preparation as shown in Figure 38. The photoresist (Nanoscribe IP-L 780) is applied on the bottom side and center of the substrate by using an oil immersion configuration (shown in Figure 39). An oil immersion lens is used. Aberrations for oil immersion configuration increase with depth. The height of structure has less than 170 μm .

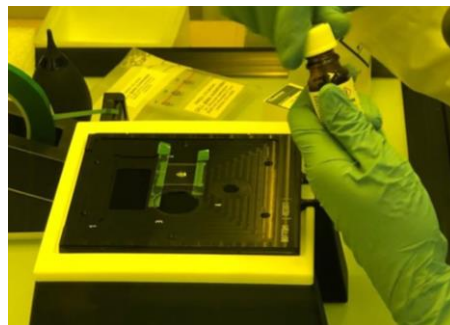


Figure 38 Application of IP-L 780 photoresist.

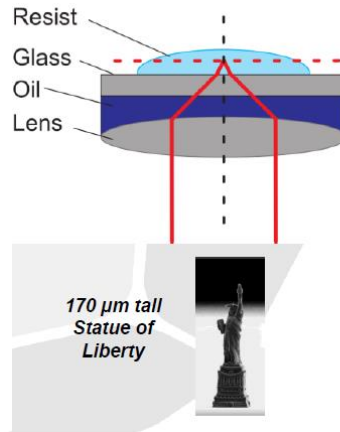


Figure 39 Oil immersion configuration (69).

2. The second step is the power-up procedure (Figure 40). The controller is switched on. The computer is turned on before turning on other components. The laser controller is then switched on. The laser is automatically controlled by NanoWrite software. The galvo scanner power supply is switched on. The galvo calibration uses 3 minutes for self-calibration. The microscope power supply unit is then turned on. The z-drive of the microscope is checked at the lowermost position. “lower z-limit reached” message in Figure 41 will appear on the screen of the microscope controller. The NanoWrite program in computer is then ready for any operation.

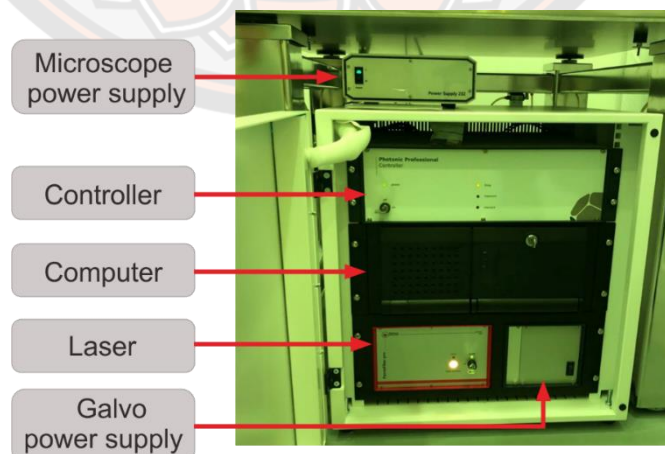


Figure 40 The device is inside the 3D printer electronics rack.



Figure 41 The microscope displays lower z-limit reached.

3. The third step is the loading of sample on the sample holder. In the NanoWrite program, the message “Exchange Holder button” appears. The user interface of NanoWrite is then clicked. After that, the holder exchange procedure starts. Z-drive will move to a save position. The first sequence of exchange holder is centered at the sample position. The objective lens reaches the lower z -drive limit afterwards. The piezo servos will be switched off when the exchange holder dialog is opened. Loading of the sample holder is now permitted. A sample holder is inserted. The sample holder must be flushed with the piezo frame. When the sample holder is loaded, user interface is chosen to be at the appropriate sample holder in the exchange holder dialog. After that, the desired sample position of the sample holder is selected in NanoWrite.

4. Next steps are approaching the sample, finding the interface and loading a print job. The sample approach is confirmed in NanoWrite. Sample approach can be started. After the printer drives the objective up along the z direction towards the substrate until it finds the interface.

A sophisticated definite focus system in this printer can automatically detect most interfaces. The automated interface detection requires a sufficient refractive index contrast $\Delta n = n_{\text{substrate}} - n_{\text{resin}}$ at 835 nm (the wavelength of the clear focus with LED illumination). The blue curve of intensity-pixel index in Figure 42 represents the interface finder. The signal curve is a combination of the grating curve part and bent curve part. The bent curve part intensity is obtained from the LED illumination. The interface position depends on the z -drive height. If the objective moves closer to the

substrate. The grating signal occurs at the right of this curve. When the z height is moved, the height increases. Grating signal leads to the left of this curve. The grating position along the x direction relates with distance between objective to interface.

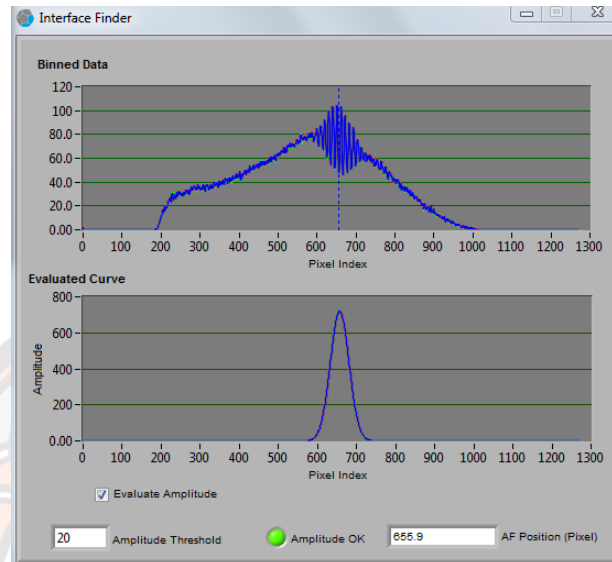


Figure 42 The curve of intensity-pixel index represents in display of the interface finder.

Then user of NanoWrite should click “Load Job button”. It will allow the user to choose the GWL file from the popup window. This GWL file of printed structure is from the design within Describe 2.1 software.

5. The printing process and unloading the sample holder. After clicking the Start Job bottom. The printing process starts. The operation is shown as shown in Figure 43. A pulsed laser beam (780 nm, 80 MHz) is focused in the resist to define the structure by creating chemically modified volume pixel point-by-point. The piezoscanning mode and continuous mode are applied because of the required high precision. A surface of the hyperboloidal microcavity is fabricated by moving the laser beam in helicoid shape (3D spiral lines). This fabricated structure has a smooth surface. After the print job finishes, the display Exchange Holder bottom in NanoWrite is then clicked to unload the sample holder. The objective lens is driven to the lower z -drive limit and the piezo servos are switched off. Then the operator must carefully pull out the sample holder.

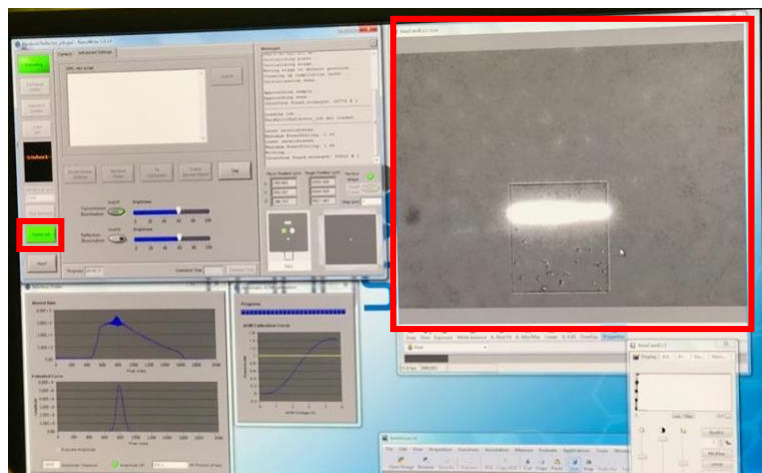


Figure 43 User interface of NanoWrite after the printing process started operation.

6. Finally, a structure is submerged in the developer (glycol 1-monomethyl ether 2-acetate: PGMEA) for 30 minutes in order to remove the residue resin of the printed structure. After that, the structure is submerged in isopropyl alcohol for 15 minutes in order to remove the developer. The substrate is taken out and gently blown by using an air ball blower.

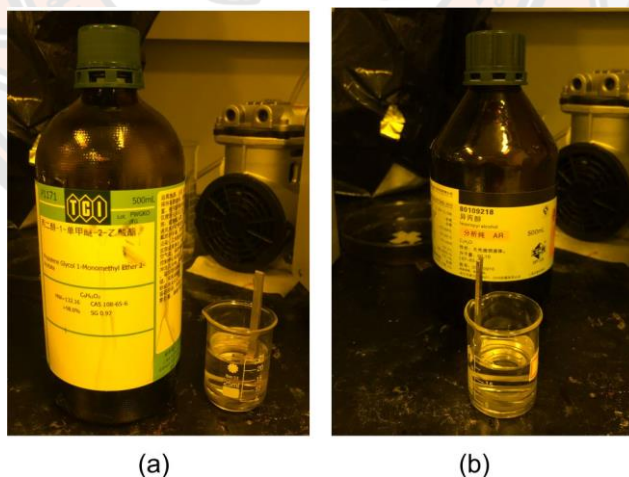


Figure 44 Sample development process includes (a) washing out the residues of the written structure and (b) removing the developer.

CHAPTER IV

RESULT AND DISCUSSION

The results from the attempt to improve hybrid QD solar cells by the integration of QDs (as the first investigated photonic structure) are discussed via the DC and AC circuit parameters and electrical properties of type-A and type-B QD solar cells. The type-A hybrid QD solar cell is the hybrid GaSb/GaAs and InAs/GaAs QD solar cell. The type-B hybrid QD solar cell is the hybrid InAs/GaAs and GaSb/GaAs QD solar cell. The change of the layer numbers as well as the switching of the layer sequence influence the solar cell performance. Comparative discussions of extracted DC circuit parameters are divided into 2 parts. One is between 1-pair and 3-pair of type-A hybrid QD solar cells. Another is between 1-pair of type-A and type-B hybrid QD solar cells. The comparative discussion of the DC circuit parameter values in the differently stacking sequence of QD layers will be done. The discussion of AC circuit parameters from 1-pair and 3-pair of type-A hybrid QD solar cells will be presented. After that, the second interesting topic is the investigation of optical microcavities. The resonant mode fields and WGM in hollow cylindrical microcavities simulated with various structural parameters are discussed. The final results are the observation of resonant modes in novel hollow hyperboloidal microcavities.

4.1 DC Circuit Parameters of Type-A and Type-B Hybrid QD Solar Cells

The results of improving in the first photonic structures by the increase of stacked hybrid QD layers and the differently stacking QD sequence are discussed via DC circuit parameters and electrical properties as follows.

4.1.1 Result and discussion of DC Circuit Parameters between 1-Pair and 3-pair of Type-A Hybrid QD Solar Cells

The measurement results of current-voltage characteristics are shown in Figure 45. Table 1 shows the extracted basic DC electrical parameters. They are the short circuit current I_{SC} , the open circuit voltage V_{OC} , the maximum power point current I_{MPP} , the maximum power point voltage V_{MPP} , the maximum power point power P_{MPP} and the fill factor FF . All indicates the quality of the hybrid QD solar cell. Note that the fill factor FF is calculated by the ratio of the maximum power point power per power at both the open circuit voltage and short circuit current

$$\left(\frac{P_{MPP}}{P_T} = \frac{I_{MPP} \times V_{MPP}}{I_{SC} \times V_{OC}} \right).$$

Table 1 DC electrical parameters for the 1-pair and 3-pair of type-A hybrid QD solar cells.

Parameters	1-pair of type-A	3-pair of type-A
	hybrid QD sample	hybrid QD sample
I_{SC} (mA)	0.325	0.176
V_{OC} (V)	0.289	0.315
I_{MPP} (mA)	0.222	0.097
V_{MPP} (V)	0.170	0.187
P_{MPP} (μ W)	377	181
FF	0.400	0.327

The short circuit current I_{SC} , the maximum power point current I_{MPP} and the maximum power point power P_{MPP} of 1-pair type-A hybrid QD sample are higher than those of the 3-pair hybrid QD sample. The differences can be explained by the fact that the photo-generated current in 3-pair hybrid QD sample is less. The defects might appear within crystal of the device as shown in the transmission electron

microscopy image of this sample (26, 58). The generated carriers would be trapped. The dark current seems to be increased, thus the photo-generated current and the short circuit current reduce. These causes the degradation of short circuit current I_{SC} and the maximum power value P_{MPP} . Therefore the fill factor FF of the 3-pair hybrid QD sample is reduced. However, the open circuit voltage V_{OC} and the maximum power point voltage V_{MPP} of 3-pair type-A hybrid QD sample have more than those of 1-pair hybrid QD sample. A higher open circuit voltage V_{OC} of hybrid QD solar cells occurs from an improvement by increasing the number of stacked InAs/GaAs and GaSb/GaAs QD pairs. Electron-hole pairs in hybrid QD solar cell are increased. The open circuit voltage V_{OC} value is also increased.

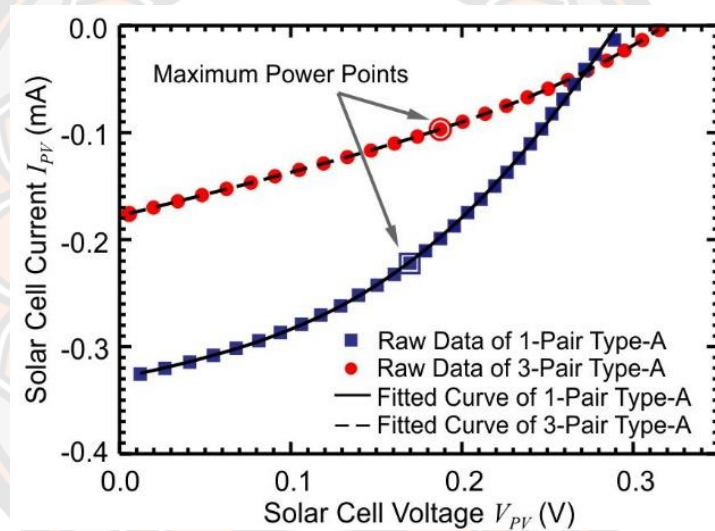


Figure 45 Current-voltage characteristic curves of 1-pair and 3-pair type-A hybrid QD samples.

The current-voltage characteristics of 1-pair and 3-pair for type-A hybrid QD samples are shown in Figure 45. Blue squares represent the measured current-voltage data of 1-pair type-A hybrid QD solar cell. The type-A sample is 1-pair hybrid GaSb/GaAs QD and InAs/GaAs QD solar cell. Red circles represent the measured current-voltage data of 3-pair type-A QD solar cell. The solid and dashed lines are fitting results with the Equation (3.1) of current-voltage characteristics and DC equivalent circuit model (See Figure 3.5). Maximum power points of each sample are marked. Table 2 shows the list of extracted DC circuit parameters. From the fitting,

we found that the diode ideality factors n of both samples are always equal 2 (as it is the upper bound of this fitting). This means that the recombination current of hybrid QD solar cells is the dominant current (64, 75).

The reverse saturation current I_o and the photocurrent I_{PH} of 3-pair hybrid QD sample are lower than the values of 1-pair hybrid QD sample. The photocurrent I_{PH} has the values of 0.354 and 0.205 mA for the 1-pair and 3-pair type-A QD samples, respectively. The photocurrents I_{PH} of the both samples are approximately equal to the short circuit current I_{SC} (see Tables 1 and 2). The DC shunt resistance ($R_{SH} = 2.21 \text{ k}\Omega$) of 3-pair hybrid QD sample has less value than of 1-pair hybrid QD sample ($R_{SH} = 3.75 \text{ k}\Omega$). This R_{SH} might lead to an increased open-circuit voltage V_{OC} (75).

The DC series resistance R_S is always lower than the DC shunt resistance. On the contrary, the DC series resistance of 3-pair type-A QD sample ($R_S = 335 \text{ }\Omega$) has higher value than of 1-pair for type-A QD sample ($R_S = 241 \text{ }\Omega$). This DC series resistance R_S in the DC circuit model represents the contact resistance. The observed low DC series resistance is consistent with the higher FF of hybrid QD solar cell. The fill factors of 1-pair and 3-pairs have the values of 0.4 and 0.327, respectively. Consequently, the 1-pair type-A QD sample has better solar cell performance than the 3-pair of type-A QD sample.

Table 2 Extracted DC circuit parameters for the 1-pair and 3-pair of type-A hybrid QD solar cells.

Parameters	1-pair of type-A	3-pair of type-A
	QD sample	QD sample
I_{PH} (mA)	0.354	0.205
n	2	2
I_o (μA)	1.009	0.130
R_S (Ω)	241	335
R_{SH} (k Ω)	3.75	2.21

4.1.2 Result and discussion of DC Circuit Parameters between Type-A and Type-B Hybrid QD Solar Cells

The measurement results of current-voltage characteristics are shown in Figure 46. Both samples are illuminated with light intensity as 1 sun at room temperature. DC electrical parameters for the 1-pair of type-A and type-B of hybrid QD solar cells are listed in Table 3. The type-B sample is 1-pair hybrid InAs/GaAs QD and GaSb/GaAs QD solar cell. The type-A sample is 1-pair hybrid GaSb/GaAs QD and InAs/GaAs QD solar cell. From this result, we found that 1-pair type-A hybrid QD sample has lower short circuit current I_{SC} and lower open circuit voltage V_{OC} values. The I_{SC} and V_{OC} of type-A hybrid QD sample are equal to 0.11 mA and 0.27 V, respectively. I_{SC} and V_{OC} of type-B hybrid QD sample are equal to 0.17 mA and 0.34 V, respectively.

Table 3 DC electrical parameters for the 1-pair of type-A and type-B of hybrid QD solar cells.

Parameters	1-pair of type-A QD sample	1-pair of type-B QD sample
I_{SC} (mA)	0.11	0.17
V_{OC} (V)	0.27	0.34
I_{MPP} (mA)	0.027	0.085
V_{MPP} (V)	0.15	0.22
P_{MPP} (μ W)	4.02	18.78
FF	0.39	0.49

The type-B hybrid QD sample has the higher short circuit current I_{SC} value since the stacking sequence in hybrid QD layers is suitable for the light absorption. When light is illuminated in structure of type-B hybrid QD sample, carrier recombination and absorption rate of electron-hole pairs increase. The straddling gap alignment influences the confinement of electron-hole pairs in of InAs/GaAs QDs

(23, 24, 29). The alignment of staggered gap is considered (28, 30, 31). After electron-hole pairs flow into GaSb/GaAs QD layer, the confinement of holes occurs in the GaSb while the electrons are surrounding in the GaAs. The alignment of staggered gap leads to long carrier lifetime. Consequently, the carriers have more possibility to escape the QD. The short circuit current I_{SC} of the type-B hybrid QD sample is thus increased (26, 58, 33).

Moreover, the correct stacking sequence in structure of type-B hybrid QD sample positively affects the maximum power point power ($P_{MPP} = 18.78 \mu\text{W}$) and the fill factor ($FF = 0.49$) values. Thus, I_{MPP} , V_{MPP} , P_{MPP} and FF of 1-pair type-B hybrid QD sample have higher values than those of 1-pair type-A hybrid QD sample. The maximum power point power P_{MPP} and the fill factor FF of type-A hybrid QD sample are approximately $4.02 \mu\text{W}$ and 0.39, respectively.

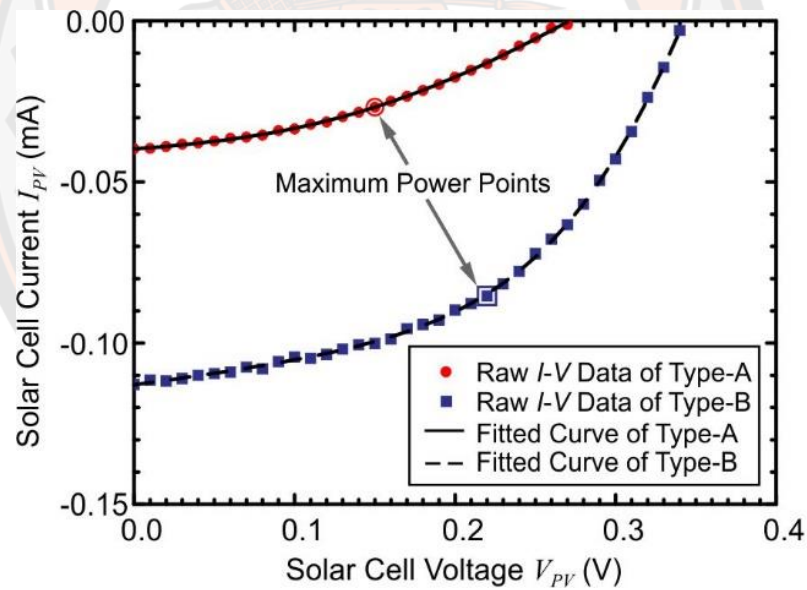


Figure 46 Current-voltage characteristic curves for the 1-pair of type-A and type-B of hybrid QD solar cells.

The current-voltage characteristics of the 1-pair for type-A and type-B hybrid QD solar cells are shown in Figure 46. Red circles represent the measured current-voltage data of 1-pair for type-A hybrid QD solar cell. Blue squares represent the measured current-voltage data of 1-pair for type-B hybrid QD solar. Maximum power points of each sample are marked in Figure 46. The solid and dashed lines are fitting with the current-voltage characteristics and DC equivalent circuit model.

The extracted DC circuit parameters are shown in Table 4. From the fitting, we found that the diode ideality factors n of both samples are always equal 2 (as it is the upper bound of the fitting). This means that the recombination current of hybrid QD solar cells is the dominant current (75, 23). The reverse saturation current I_o and the photocurrent I_{PH} of 1-pair for type-B hybrid QD sample have the higher values than those of 1-pair type-A hybrid QD sample. The photocurrent I_{PH} of the both samples are equal to the short circuit current I_{SC} (See Tables 3 and 4). The photocurrent I_{PH} has the values of 0.115 and 0.176 mA of type-A and type-B hybrid QD samples, respectively.

The DC shunt resistance ($R_{SH} = 4.820 \text{ k}\Omega$) of type-B hybrid QD sample has less value than that of type-A hybrid QD sample ($R_{SH} = 15.36 \text{ k}\Omega$). The DC series resistance R_S is always lower than the DC shunt resistance R_{SH} . On the contrary, the DC series resistance of type-B hybrid QD sample ($R_S = 0.249 \text{ k}\Omega$) has a higher value than of type-A hybrid QD sample ($R_S = 0.321 \text{ k}\Omega$). The higher contact resistance and the high leakage current of type-A QD sample lead to the low fill factor of the hybrid QD solar cell. This effect is from the incorrectly stacking sequence of QD layers. The fill factors of type-A and type-B hybrid QD sample have the values of 0.39 and 0.49, respectively. Consequently, the correct stacking sequence of QD layers in type-B hybrid QD sample can provide better solar cell performance than the 1-pair of type-A QD sample.

Table 4 Extracted DC circuit parameters for the 1-pair of type-A and type-B of hybrid QD solar cells.

Parameters	1-pair of type-A	1-pair of type-B
	QD sample	QD sample
I_{PH} (mA)	0.115	0.176
n	2	2
I_o (μ A)	0.124	0.180
R_S (k Ω)	0.321	0.249
R_{SH} (k Ω)	15.36	4.820

4.2 Result and discussion of AC Circuit Parameters between 1-Pair and 3-pair type-A hybrid QD solar cells

The AC voltage signals are measured at the signal frequency f between 1 kHz and 1 MHz. Examples of AC input and output voltage signals at $f = 500$ kHz are shown in Figure 47. The AC input $V_{S,AC}$ and output V_{PV} voltage signals are plotted with green squares and red circles, respectively. The solid line is the fitting with $v_{S,AC} = A_{in} \sin(2\pi ft)$ and dashed line is the fitting with $v_{PV} = A_{out} \sin(2\pi ft + \phi)$, where A_{out} is the amplitude of output voltage, f is the frequency, and ϕ is the phase difference. After fitting, the output voltage amplitude A_{out} , the input voltage amplitude A_{in} and the phase difference ϕ are extracted.

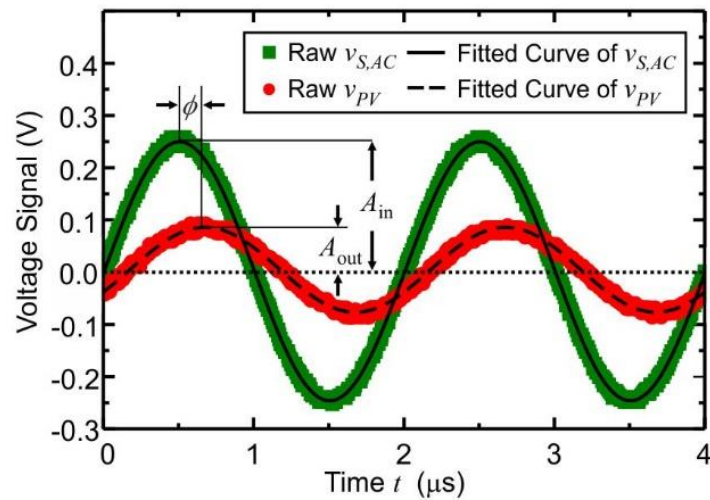


Figure 47 Waveforms of input and output voltage signals obtain from the oscilloscope at $f = 500$ kHz. The full and dashed lines are the fitted results.

The obtained amplitude ratio of output voltage amplitude A_{out} per input voltage amplitude (A_{out}/A_{in}) from the 1-pair and 3-pair hybrid QD samples are plotted with blue squares and red circles in Figure 48. The results are frequency responses. Vertical axis represents the amplitude ratio A_{out}/A_{in} . Horizontal axis represents the frequency f . The frequency responses of 1-pair and 3-pair hybrid QD samples are shown in Figure 48. The solid and dashed lines are the fitting with the AC equivalent circuit model. The responses of both samples decrease with the frequency. The 1-pair hybrid QD sample has broader frequency response than that of the 3-pair hybrid QD sample. The AC series resistance R_s^{AC} , the AC diode capacitance C_D and the AC shunt resistance R_{SH}^{AC} are extracted from fitting of frequency response curves.

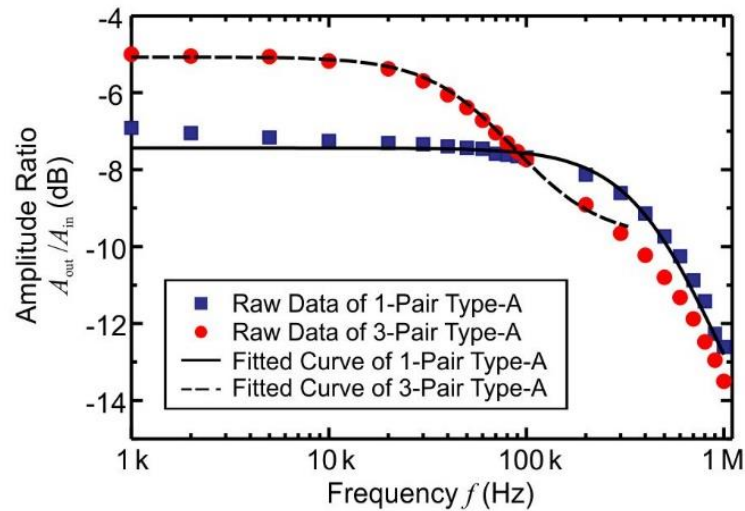


Figure 48 Frequency responses for 1-pair and 3-pair of hybrid QD solar cells biased at maximum power points (marked in Figure 45).

The extracted AC circuit parameters of hybrid QD solar cells are listed in Table 5. The diode capacitance of 3-pair hybrid QD sample ($C_D = 5.47$ nF) has higher value than that of the 1-pair hybrid QD sample ($C_D = 1.33$ nF) since the buried QDs in the 3-pair hybrid QD sample have high volume density.

In addition, the cutoff frequency of 1-pair hybrid QD sample has a higher value than that of 3-pair hybrid QD sample. The cutoff frequency is typically inversely proportional with the diode capacitance C_D of hybrid QD solar cell. The low value of cutoff frequency implies that the diode capacitance C_D of solar cell is high. Thus 1-pair hybrid QD sample has wider frequency bandwidth than that of 3-pair hybrid QD sample.

Table 5 Extracted AC circuit parameters for 1-pair and 3-pair of hybrid QD solar cells.

Parameters	1-pair of type-A	3-pair of type-A
	hybrid QD sample	hybrid QD sample
C_D (nF)	1.33	5.47
R_S^{AC} (Ω)	81	315
R_D (k Ω)	0.583	3.77
R_{SH}^{AC} (k Ω)	0.504	1.39

The extracted values of AC series resistance of 3-pair hybrid QD sample is higher than that of 1-pair hybrid QD sample. The DC series resistance has a higher value than that of AC series resistance when AC series resistance R_S^{AC} and DC series resistance R_S are considered. In fact, the DC series resistance R_S is the summation of AC series resistance R_S^{AC} and static resistance R^O ($R_S = R_S^{AC} + R^O$). The static resistance ($R^O = 160 \Omega$) of 1-pair hybrid QD sample has a higher value than that of 3-pair hybrid QD sample ($R^O = 20 \Omega$). The static resistance R^O in both samples does not respond to AC signal.

The AC shunt resistance of 3-pair hybrid QD sample ($R_{SH}^{AC} = 1.39 \text{ k}\Omega$) has higher value than that of 1-pair hybrid QD sample ($R_{SH}^{AC} = 504 \Omega$). The AC shunt resistances R_{SH}^{AC} are always higher value than the AC series resistances R_S^{AC} since the AC shunt resistance R_{SH}^{AC} is parallel between AC diode resistance R_D of solar cell and DC shunt resistance R_{SH} . These parameters are shown in red dashed frame in Figure 31 of the AC equivalent circuit model. The AC diode resistance R_D of 1-pair hybrid QD sample ($R_S^{AC} = 81 \Omega$) is lower than that of 3-pair hybrid QD sample ($R_S^{AC} = 315 \Omega$). When the current flows through the sample, a small portion of the photo-generated carriers might flow through some defects. This can affect the value of DC shunt resistance R_{SH} .

The low DC shunt resistance R_{SH} implies that the more leakage current flows through the DC shunt resistor since a high number of defects is observed in this sample (23, 24). The AC diode resistance R_D tends in the same direction with AC shunt resistance R_{SH}^{AC} . The AC diode resistance R_D of 3-pair hybrid QD sample ($R_D = 3.77 \text{ k}\Omega$) has higher value than that of 1-pair hybrid QD sample ($R_D = 0.583 \text{ k}\Omega$). The R_D relates to the leakage current as well (29). The DC leakage current flows through the DC shunt resistor. The leakage current causes the reduced solar cell current as $|I_{PV}| = I_{PH} - I_D - V_D / R_{SH}$ where $I_D = I_o \left(\exp(qV_D / nkT) - 1 \right)$. The quantity of defects in the grown structure influences the values of these resistances.

4.3 Whispering-gallery mode and optical characteristics of hollow optical microcavities

The second interesting photonic structure in this thesis is the optical microcavities. They are ultimately aimed to improve the efficiency of solar cells. Three results from optical microcavities are discussed. They are the resonant mode fields of hollow cylindrical optical microcavities by using FDTD simulation, the WGM in hollow cylindrical microcavities at various structural parameters, and the PL of hollow hyperboloidal microcavities.

4.3.1 Result and discussion about the resonant mode fields of hollow cylindrical optical microcavities by using FDTD simulation

The magnetic field profiles H_z of resonant mode for the mode index $m = 19, 20, \text{ and } 21$ are shown in Figures 49 (a), (b), and (c), respectively by using the FDTD simulation with the symmetric domain. Initial simulation domain is designed as shown in Figure 36. The hole radius r is set at $0.25a$. The hole numbers along column N and hole numbers along row M are set 20 and 3, respectively. The results of varied mode index m found that when the mode index m are set at 19, 20, and 21. The Q factor values are obtained at 214, 407 and 1531, respectively. And the resonant frequencies f_c are achieved at $0.49234(c/a)$, $0.51602(c/a)$ and $0.54111(c/a)$,

respectively. The color scale shows the magnetic field H_z from negative H_z (dark red) to zero (white) to positive H_z (dark blue).

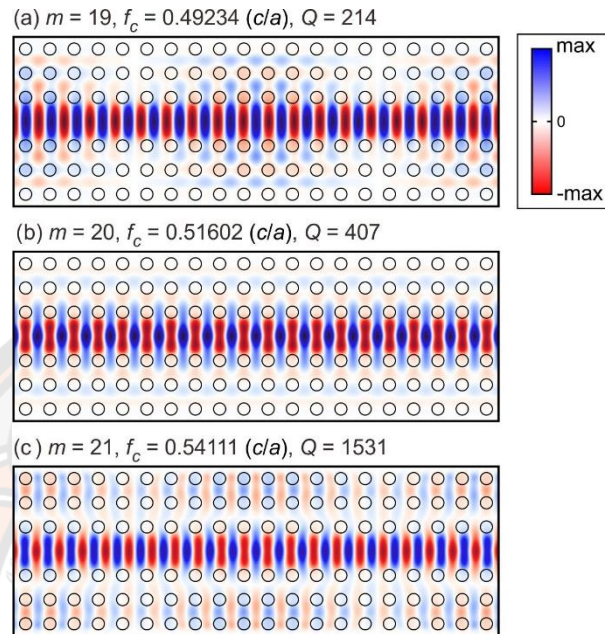


Figure 49 The magnetic field profiles H_z of resonant modes are extracted at $m =$ (a) 19, (b) 20, and (c) 21 in simulation domain for low Q factor.

The relation of varied mode index m with Q factor values and varied mode index m can be explained by the fact that a resonant frequencies f_c in these modes can be calculated from $f_c = m/n_e N$, where n_e is the effective index. The relation of this equation is equivalent to the well-known $L = m\lambda/n_e$, where λ is the optical wavelength in vacuum. Optical leakage of each mode in other microcavities can be characterized by its Q factor, but this microcavity does not show a clear trend of the Q factor variation as a function of mode index m .

On the other hand, typical WGM microcavities have a clear trend of the Q factor variation such as microdisks (76). It relates with the variation of spatial mode field pattern and the array of holes. Whereas only at $m = N$ can appear the matching between the hole period and the field wavelength, the other modes are considered to a different scattering loss at the hole edge. For the case of mode index m is equal to 20.

The hole numbers along column N in this FDTD simulation is set at 20 ($m = N$). Lossy field profile occurs from the large overlap between the magnetic field H_z and the patterned holes. The obtained Q factor value is low ($Q \sim 407$).

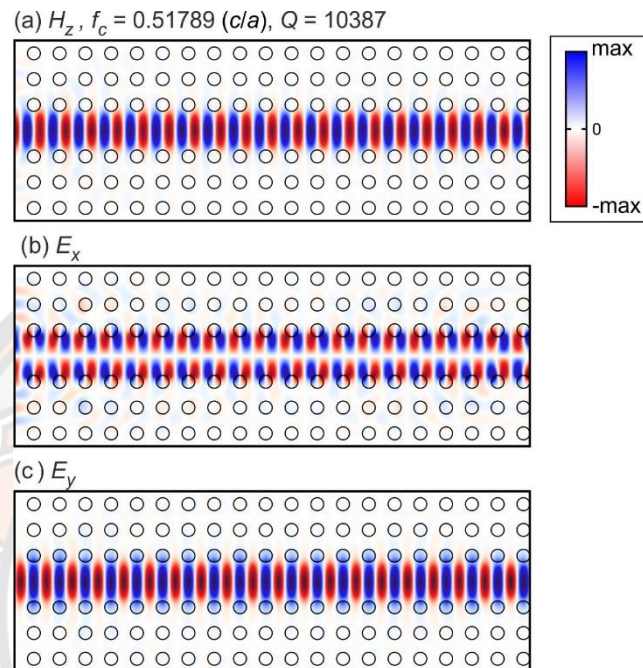


Figure 50 (a) The magnetic field profile H_z , (b) the electric field profiles E_x and (c) E_y are extracted at $m=20$ in simulation domain for single high Q factor.

The asymmetric simulation domain is initially designed as in Figure 36. The hole radius r is set at $0.25a$. The hole numbers along column N and hole numbers along row M are set at 20 and 3, respectively. The mode index $m = 20$ matches the hole number along the

column N . Other parameters are not changed. The excitation source and the boundary location are simultaneously changed in order to obtain the enhancement of the single WGM mode. The magnetic field profiles H_z , electric field profiles in x -direction E_x and electric field profiles in y -direction E_y of the enhanced mode are shown in Figures 50 (a), (b), and (c), respectively. These obtained electric and magnetic fields can be related to others by using classical/conventional Maxwell's equations (70, 72). The Q factor value of 10387 is obtained and the resonant frequency f_c of $0.51789(c/a)$ is achieved.

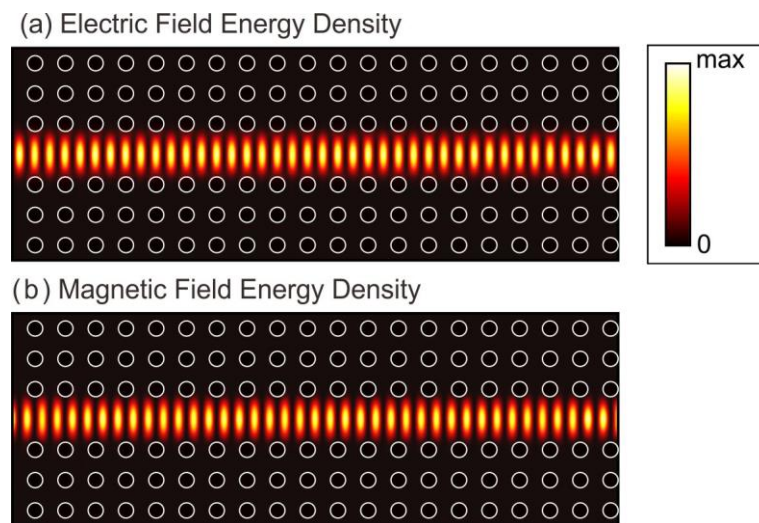


Figure 51 (a) the electric and (b) magnetic field energy density profiles are extracted at $m=20$ in simulation domain for single high Q factor.

The electric and magnetic field energy densities can be simulated as shown in Figures 5.1(a) and (b). The temporal oscillations are observed in these field energy densities. The color scale shows from zero (black) to maximum value (white). This profile of electric energy density is compared the results in reference (73). The profile of electric energy density in Figure 5.1(a) is qualitatively similar to the field profile shown in that reference. However, the field profile of that reference is calculated by using the finite element method (77). Thus, the field results from our FDTD simulation are correctly calculated and our field results are consistent with other calculation methods.

4.3.2 Result and discussion about WGM of hollow cylindrical microcavities at various structural parameters

The various structural parameters of hollow cylindrical microcavities are simulated in the FDTD method. The structural parameters are the hole radius r , the missing hole width or the waveguide width w , the hole number along columns N and hole number along rows M . The resonant frequency f_c and the Q factor are extracted

after the simulations with various structural parameters. The results are discussed below.

(a) Effect of varying the hole radius r to the resonant frequency f_c and the Q factor values

The varying results of the hole radius r affect the resonant frequency f_c and the Q factor values as shown in Figure 52. Red circles represent the variation of the Q factor as a function of hole radius r . Blue squares represent the variation of the resonant frequency f_c as a function of hole radius r . The frequency f_c of 0.5142, 0.5147, 0.5152, 0.5158, 0.5163, 0.5168, 0.5174 and 0.5179 (c/a) are accomplished at normalized hole radius r/a of 0.18, 0.19, 0.2, 0.21, 0.22, 0.23, 0.24 and 0.25, respectively. When the hole radius r increases, the resonant frequency increases linearly. The extracted positive slope of this resonant frequency f_c - hole radius r relation is $(0.05305 \pm 1.93 \times 10^{-4})c$. The tendency in this results is named a blueshift.

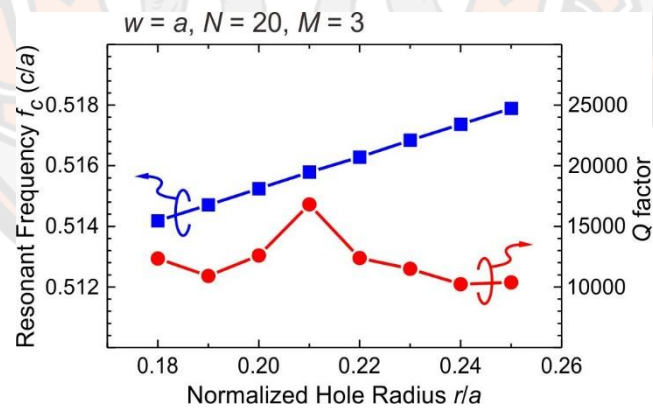


Figure 52 Variations of resonant frequency f_c and Q factor as a function of hole radius r .

This result can be described by the diminishing of the effective width of the field and/or the reduction of effective index of the hole array. An increasing of hole radius r causes the reduction of the waveguiding area. This is similar to the decreasing of the width w . The confined field profile in the resonance cavity is reduced as

increasing in the hole radius r . This is similar to a reduction of the effective index and it results in the blueshift of the resonant frequency. An analogy to the electronic wavefunction in finite square well in Quantum Mechanics can be done (70, 79). The high electron confinement energy will reduce the well width. Furthermore, the increasing of the barrier height can enhance this frequency, which is proportional to the photon energy.

When results of the Q factor- the hole radius r relation are considered. The Q factor values of 12347, 10902, 12609, 16820, 12394, 11508, 10232 and 10387 are achieved at normalized hole radius r/a of 0.18, 0.19, 0.2, 0.21, 0.22, 0.23, 0.24 and 0.25, respectively. The hole radius at $0.21a$ is interesting because this setting can obtain a high Q value of 10387. The optimization of Q factor value can do by simultaneously varying of several parameters. Thus the optimum configuration of simultaneously several parameters might obtain the well field profile and high Q factor. However, the Q factor optimization of simultaneously several parameters is not the scope of this work.

(b) Effect of varying the missing hole width w to the resonant frequency f_c and the Q factor values

The change of width of missing hole line w affects the resonant frequency f_c and the Q factor values as shown in Figure 53. Red circles represent the variation of the Q factor as a function of width of missing hole line w . Blue squares represent the variation of the resonant frequency f_c as a function of width of missing hole line w .

The relation between resonant frequency f_c and the width w is considered. The frequency f_c of 0.5187, 0.5183, 0.5179, 0.5175, 0.5171 and 0.5168 (c/a) is accomplished at normalized width w/a of 0.96, 0.98, 1.00, 1.02, 1.04 and 1.06, respectively. When the width of missing hole line w increases, the resonant frequency decreases linearly. The extracted negative slope of this resonant frequency f_c - width w relation is $(-0.01978 \pm 2.33 \times 10^{-4})c$. The tendency in this results is named a redshift (78). A redshift or a negative blueshift is as simultaneous reduction of the frequency and photon energy. On the other hand, the wavelength increases.

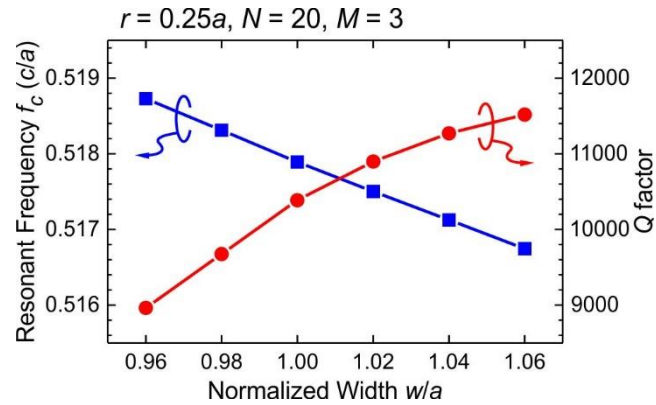


Figure 53 Variations of resonant frequency f_c and Q factor as a function of missing hole width w .

When the relation between the Q factor and width w is considered, the Q factor values of 8965, 9674, 10387, 1089, 11272 and 11517 are obtained at normalized width w/a of 0.96, 0.98, 1.00, 1.02, 1.04 and 1.06, respectively. This result can be explained by the widening of the field width. When width of missing hole line w increases, the Q factor increases. Therefore, the varying of this parameter can enhance the Q factor. Nevertheless, appearance of higher order mode along vertical direction and narrowing of the adjacent modes might have to be considered.

(c) Effect of varying hole number along columns N to the resonant frequency f_c and the Q factor values

The variation of the hole numbers along column N affects the resonant frequency f_c and the Q factor values as shown in Figure 54. Red circles represent the variation of the Q factor as a function of the hole numbers along column N . Blue squares represent the variation of the resonant frequency f_c as a function of the hole number along column N . The results found that when the hole number along column N increases, the resonant frequency f_c remains constant. A resonant frequency f_c approximates $0.5179(c/a)$. The obtained variation occurs from the numerical uncertainty. This result is correct according to the conventional theory (73).

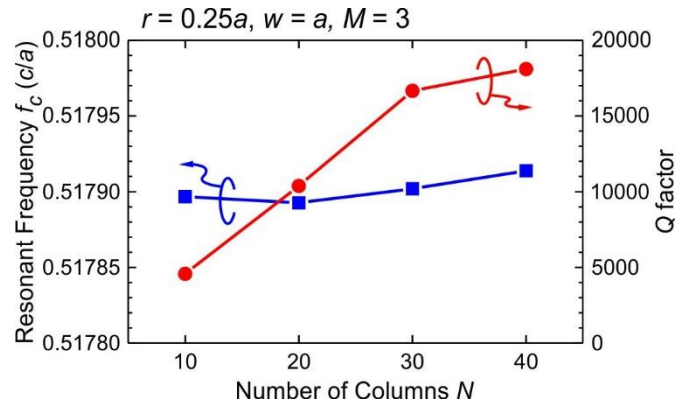


Figure 54 Variations of resonant frequency f_c and Q factor as a function of hole numbers along columns N .

When the variation of Q factor is considered, the Q factor values of 4572, 10387, 16657 and 18097 are obtained at $N = 10, 20, 30$ and 40 , where N is the number of columns along x -direction. In the Q factor - N curve, we observe a high Q factor when N is set at 40. The Q factor is equal to 18097. It seems that the direction of Q factor value is trending upward when the hole numbers along column N further increases. However, if numbers along column N is further large. The simulation must use a larger domain. This tendency might be explained that the dynamic of field profile is enhanced in a larger confined structure.

(d) Effect of varying hole number along rows M to the resonant frequency f_c and the Q factor values

The variation of the hole number along rows M affects the resonant frequency f_c and the Q factor values as shown in Figure 55. Red circles represent the variation of the Q factor as a function of the hole numbers along row M . Blue squares represent the variation of the resonant frequency f_c as a function of the hole numbers along row M . This result explains that the level of lateral confinement is indicated by the number of rows. This is similar to electronic QW, it can see as the barrier layer. The relation between f_c and N is as follows. When the hole number along column N increases, the resonant frequency f_c remains constant (Small variation is due to the numerical uncertainty). A resonant frequency f_c approximates $0.5179(c/a)$.

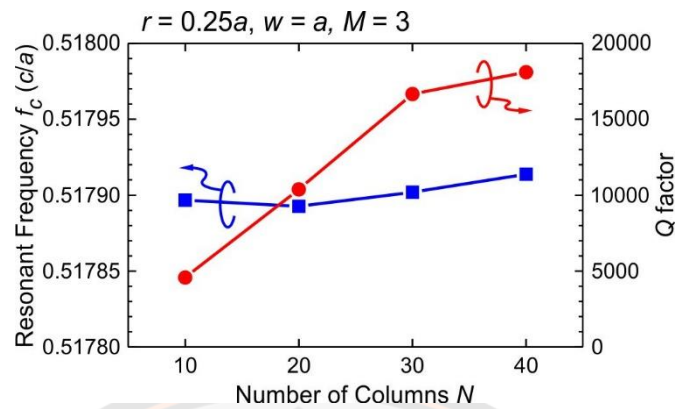


Figure 55 Variations of resonant frequency f_c and Q factor as a function of hole numbers along rows M .

When the Q factor variation due to the change of M is considered, the Q factor values of 3896, 9015, 10387, 11585 and 14607 are obtained at $M = 1-5$. At the lower boundary ($M = 1$), we observe a low Q factor value of 3896. For the 5 rows of hole numbers ($M = 5$), a high Q factor value of 14607 is obtained. Therefore, the hole numbers M along y -direction can affect the Q factor value. Note that the strain-driven self-rolling process, which is used to fabricate this hollow cylindrical microcavity, is influenced by this parameter. In other words, the changing of the hole numbers affects the fabrication process. A nanomembranes with a large hole numbers might have reduced intrinsic strain and they might not roll as desired.

4.3.3 Result and discussion about an optical microcavity of hollow hyperboloidal microcavities

The PL measurement for the optical characteristics of hollow hyperboloidal microcavities is performed. An excitation laser with the emission of 514.53 nm is applied. The laser power is set at 15 mW by using LabSpec software. A microscope objective lens has a 50x magnification. The laser focuses on the center of the samples.

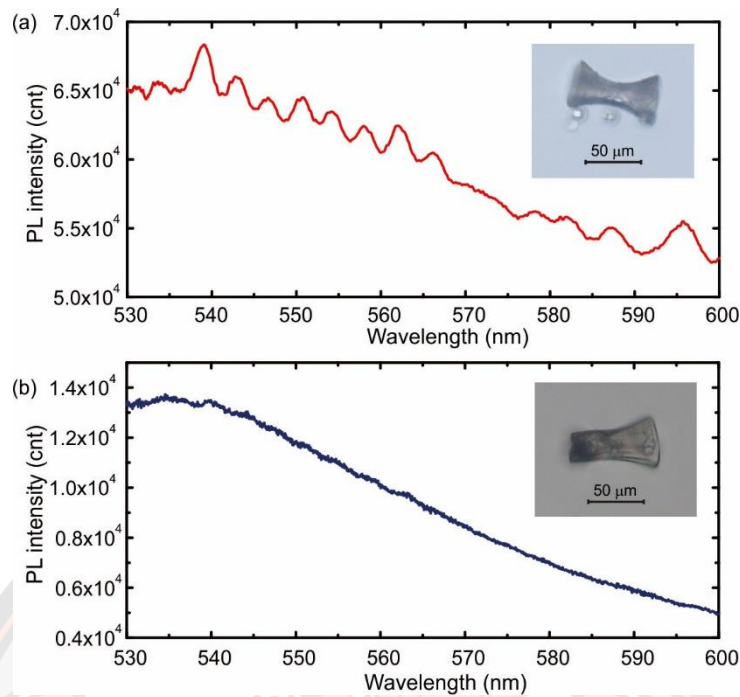


Figure 56 PL spectra of (a) the hyperboloidal microcavity sample and (b) the sample with some structural imperfection.

A typical PL spectrum of a symmetrical hyperboloidal microcavity is shown in Figure 56 (a). An effective refractive index n_{eff} is calculated from this data $n_{eff} \approx (\lambda_m^2 / \Delta\lambda) / \pi D$. The wavelength of interesting mode is λ_m , wavelength of nearby mode is λ_{m+1} and the free spectral range is $\Delta\lambda = \lambda_{m+1} - \lambda_m$. The hyperboloid diameter D at focused position of laser is center of this symmetrical structure is about $20 \mu\text{m}$. $D \approx 20 \mu\text{m}$. Range of effective refractive index approximately 1.15-1.35 is obtained. The Q factor is defined by $Q = \lambda_m / \Delta\lambda_m$. Where $\Delta\lambda_m$ is width of the peak mode. Typically, low quality Q factors of 250-445 are revealed the observed wavelength range of 530-570 nm. For the structure with defect as shown in Figure 56 (b), no resonant modes are observed.

CHAPTER V

CONCLUSION

This thesis presents the investigation of the two photonic structures for improving the solar cells. They are QD structure and optical microcavity. The different QD structures are investigated and comparatively discussed by the electrical characteristics and circuit parameters of hybrid QD solar cells while structures of optical microcavities are investigated for their optical characteristics.

For the hybrid QD solar cells, the improvement can be done by the increase of stacked hybrid QD layers and the differently stacking QD sequence. The DC and AC circuit parameters for type-A and type-B hybrid QD solar cells are extracted and discussed. The type-A hybrid QD solar cell is the hybrid GaSb/GaAs and InAs/GaAs QD solar cell. The type-B hybrid QD solar cell is hybrid InAs/GaAs and GaSb/GaAs QD solar cell. The experimental results are summarized as follows. The extracted DC circuit parameters of hybrid QD solar cells are obtained from the fitting the current-voltage characteristic curves. The reverse saturation current I_o , the diode ideality factor n , the photocurrent I_{PH} , the series resistance R_S and the shunt resistance R_{SH} are obtained. Firstly, DC circuit parameters of 1-pair and 3-pair for type-A hybrid QD solar cells are comparatively discussed. When stacking layer number of hybrid QD layer increases, generated electron-hole pairs in hybrid QD solar cell are increased. Effects to the open-circuit voltage V_{OC} value is also increased. The reverse saturation current I_o and the photocurrent I_{PH} of 3-pair hybrid QD sample are lower than those of 1-pair hybrid QD sample. The DC shunt resistance R_{SH} has always a higher value of the DC series resistance R_S . However, increasing of stacking layer number unavoidably increase the total layer thickness and some defects in the fabrication process. The series resistance R_S increases and the shunt resistance R_{SH} decreases for the thick sample. The 1-pair of type-A QD sample has therefore better solar cell performance and higher fill factor than those of the 3-pair type-A QD sample.

The DC circuit parameters of 1-pair for type-A and type-B hybrid QD solar cells are discussed. The photocurrents I_{PH} of the both hybrid QD solar cells can

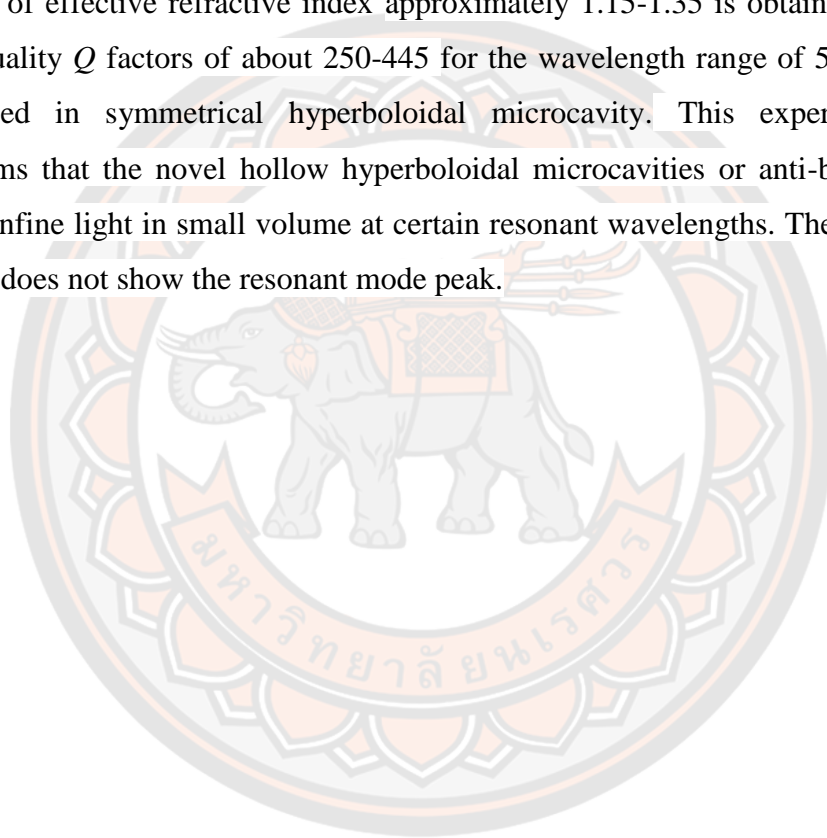
approximately equal to the short circuit current I_{SC} . The dominant recombination current occurs in the space charge region (the diode ideality factor $n = 2$). The correct stacking sequence of type-B hybrid QD solar cell can provide a better performance and fill factor. The reverse saturation current I_O and the photocurrent I_{PH} of the correct stacking sequence have higher values. The series resistance R_S is a lower value and the shunt resistance R_{SH} is a higher value than those of the type-A hybrid QD solar cell.

The AC circuit parameters of hybrid QD solar cells are extracted by the fitting the frequency response under the controlled bias condition at the maximum power point. The diode capacitance C_D , the diode resistance R_D , the AC series resistance R_S^{AC} and the AC shunt resistance R_{SH}^{AC} are obtained. The AC circuit parameters of 1-pair and 3-pair for type-A hybrid QD solar cells are discussed. The increase of stacking layers (3-pair hybrid QD sample) leads to the high AC diode capacitance C_D and high AC diode resistance R_D (higher than those of the 1-pair hybrid QD sample) because of the high number density in the buried QDs. The 1-pair hybrid QD sample has faster AC response and wider frequency bandwidth than those of 3-pair hybrid QD sample. The AC shunt resistance R_{SH}^{AC} , the AC series resistance R_S^{AC} and the capacitance R_D of 3-pair hybrid QD solar cell have higher values. The static resistance R^O of 1-pair hybrid QD sample is higher than that of 3-pair hybrid QD sample.

Then, another photonic structure for enhancing solar cell efficiency is studied. The optical hollow microcavities are investigated. Designed structure of periodic hole array (hollow cylindrical microcavities) and hollow hyperboloid microcavities are presented. For hollow cylindrical optical microcavities, simulations with symmetric and asymmetric domains are performed. Low Q factor modes are observed in symmetric domain. When asymmetric domain is used, the high Q mode is achieved. All relevant electric and magnetic field profiles are presented. The Q factor variation as a function of mode index m relates with spatial field mode pattern and the array holes. Whereas only at $m = N$ can appear the matching between the hole period and the field wavelength. The variation of structural parameters in FDTD simulations provides that the resonant frequency f_C depends on the hole radius r and the waveguide width w . When the hole radius r increases, the resonant frequency

blueshifts. While the width w increases, the resonant frequency redshifts. The Q factor depends on the hole radius r , the width w , the number of holes along vertical and horizontal directions (N and M). When the width w , the hole numbers along column N and row M increase, the Q factor simultaneously increases.

Novel hollow hyperboloid optical microcavities are designed. This new shape is also called anti-bottle resonator. The optical characteristics are investigated by using the PL measurement. The fabricated structures can act as an optical resonator. Range of effective refractive index approximately 1.15-1.35 is obtained. The rather low quality Q factors of about 250-445 for the wavelength range of 530-570 nm are observed in symmetrical hyperboloidal microcavity. This experimental result confirms that the novel hollow hyperboloidal microcavities or anti-bottle resonator can confine light in small volume at certain resonant wavelengths. The structure with defect does not show the resonant mode peak.



REFERENCES



REFERENCES

1. Li, S. S. Solar cells and photodetectors. Netherlands: Springer; 2006:381-457.
2. Abdin Z, Alim MA, Saidur R, Islam MR, Rashmi W, Mekhilef S, Wadi A. Solar energy harvesting with the application of nanotechnology. Renewable and sustainable energy reviews. 2013 Oct 1;26:837-52.
3. Green, M. A. Third Generation Photovoltaics: Advanced Solar Energy Conversion. Springer, Netherlands, 2006.
4. Wikipedia, the free encyclopedia. Czochralski method [Internet]. Florida; [cited 2020 December 28]. Available from http://en.wikipedia.org/wiki/Czochralski_process
5. Manna TK, Mahajan SM. Nanotechnology in the development of photovoltaic cells. Proceedings of IEEE Conference on Clean Electrical Power; 2007 May 21; Capri. Italy: IEEE; 2007. p. 379-86.
6. Solarquotes. Polycrystalline VS Monocrystalline solar panels [Internet]. Australia; [cited 2020 December 28]. Available from <https://www.solarquotes.com.au/panels/photovoltaic/monocrystalline-vs-polycrystalline>
7. Kerschaver EV, Beaucarne G. Back-contact solar cells: A review. Progress in Photovoltaics: Research and Applications. 2006 Mar;14(2):107-23.
8. Staebler DL, Wronski CR. Reversible conductivity changes in discharge-produced amorphous Si. Applied physics letters. 1977 Aug 15;31(4):292-4.
9. El Chaar L, El Zein N. Review of photovoltaic technologies. Renewable and sustainable energy reviews. 2011 Jun 1;15(5):2165-75.
10. Li W, Liang C, Zhou W, Qiu J, Zhou Z, Sun G, et al. Preparation and characterization of multiwalled carbon nanotube-supported platinum for cathode catalysts of direct methanol fuel cells. The Journal of Physical Chemistry B. 2003 Jul 3;107(26):6292-9.

11. Guimard D, Grand PP, Bodereau N, Cowache P, Guillemoles JF, Lincot D, et al. Copper indium diselenide solar cells prepared by electrodeposition. Proceedings of Conference Record of the Twenty-Ninth IEEE Photovoltaic Specialists Conference; 2002 May 19; New Orleans. Los Angeles. USA: IEEE; 2002. p. 692-5.
12. Wikipedia, the free encyclopedia. Cadmium telluride photovoltaics [Internet]. Florida; [cited 2020 December 30], Available from https://en.wikipedia.org/wiki/Cadmium_telluride_photovoltaics
13. Nozik AJ. Nanoscience and nanostructures for photovoltaics and solar fuels. Nano letters. 2010 Aug 11;10(8):2735-41.
14. Sablon KA, Little JW, Olver KA, Wang ZM, Dorogan VG, Mazur YI, et al. Effects of AlGaAs energy barriers on InAs/GaAs quantum dot solar cells. Journal of Applied Physics. 2010 Oct 1;108(7):074305.
15. Los Alamos National Security. News Release: NREL Scientists report first solar cell producing more electrons in photocurrent than solar photons entering cell [Internet]. United States; [cited 2020 December 30], Available from <http://www.nrel.gov/news/press/2011/1667.html>
16. Scavennec A, Sokolich M, Baeyens Y. Semiconductor technologies for higher frequencies. IEEE microwave magazine. 2009 May 2;10(2):77-87.
17. Huang LM, Hu CW, Liu HC, Hsu CY, Chen CH, Ho KC. Photovoltaic electrochromic device for solar cell module and self-powered smart glass applications. Solar Energy Materials and Solar Cells. 2012 Apr 1;99:154-9.
18. Yin Z, Sun S, Salim T, Wu S, Huang X, He Q, et al. Organic photovoltaic devices using highly flexible reduced graphene oxide films as transparent electrodes. ACS nano. 2010 Sep 28;4(9):5263-8.
19. Yang P, Yan R, Fardy M. Semiconductor nanowire: what's next?. Nano letters. 2010 May 12;10(5):1529-36.

20. Schmidt V, Wittemann JV, Gosele U. Growth, thermodynamics, and electrical properties of silicon nanowires. *Chemical reviews*. 2010 Jan 13;110(1):361-88.
21. Yuan G, Aruda K, Zhou S, Levine A, Xie J, Wang D. Understanding the origin of the low performance of chemically grown silicon nanowires for solar energy conversion. *Angewandte Chemie*. 2011 Mar 1;123(10):2382-6.
22. Luque A, Martí A. Increasing the efficiency of ideal solar cells by photon induced transitions at intermediate levels. *Physical Review Letters*. 1997 Jun 30;78(26):5014-7.
23. Okada Y, Ekins-Daukes NJ, Kita T, Tamaki R, Yoshida M, Pusch A, et al. Intermediate band solar cells: Recent progress and future directions. *Applied physics reviews*. 2015 Jun 8;2(2):021302.
24. Guimard D, Morihara R, Bordel D, Tanabe K, Wakayama Y, Nishioka M, et al. Fabrication of InAs/GaAs quantum dot solar cells with enhanced photocurrent and without degradation of open circuit voltage. *Applied Physics Letters*. 2010 May 17;96(20):203507.
25. Mellor A, Luque A, Tobías I, Martí A. The influence of quantum dot size on the sub-bandgap intraband photocurrent in intermediate band solar cells. *Applied Physics Letters*. 2012 Sep 24;101(13):133909.
26. Rakpaises T, Sridumrongsak N, Chevintulak C, Thainoi S, Kiravittaya S, Nuntawong N, et al. Demonstration of photovoltaic effects in hybrid type-I InAs/GaAs quantum dots and type-II GaSb/GaAs quantum dots. *Proceedings of IEEE 7th World Conference on Photovoltaic Energy Conversion*; 2018 Jun 10; Waikoloa, Hawaii, USA: IEEE; 2018. p. 2928-32.
27. Kiravittaya S, Songmuang R, Rastelli A, Heidemeyer H, Schmidt OG. Multi-scale ordering of self-assembled InAs/GaAs (001) quantum dots. *Nanoscale Research Letters*. 2006 Jun;1(1):1-0.
28. Laghumavarapu RB, Moscho A, Khoshakhlagh A, El-Emawy M, Lester LF, Huffaker DL. GaSb/ GaAs type II quantum dot solar cells for enhanced infrared spectral response. *Applied Physics Letters*. 2007 Apr 23;90(17):173125.

29. Stier O, Grundmann M, Bimberg D. Electronic and optical properties of strained quantum dots modeled by 8-band $k \cdot p$ theory. *Physical Review B*. 1999 Feb 15;59(8):5688-5701.
30. Poempool T, Kiravittaya S, Sopitpan S, Thainoi S, Kanjanachuchai S, Ratanathamaphan S, et al. GaSb and InSb quantum nanostructures: morphologies and optical properties. *MRS Advances*. 2016;1(23):1677-82.
31. Ledentsov NN, Böhrer J, Beer M, Heinrichsdorff F, Grundmann M, Bimberg D, et al. Radiative states in type-II GaSb/GaAs quantum wells. *Physical Review B*. 1995 Nov 15;52(19):14058.-66.
32. Liang B, Lin A, Pavarelli N, Reyner C, Tatebayashi J, Nunna K, et al. GaSb/GaAs type-II quantum dots grown by droplet epitaxy. *Nanotechnology*. 2009 Oct 16;20(45):455604.
33. Ji HM, Liang B, Simmonds PJ, Juang BC, Yang T, Young RJ, et al. Hybrid type-I InAs/GaAs and type-II GaSb/GaAs quantum dot structure with enhanced photoluminescence. *Applied Physics Letters*. 2015 Mar 9;106(10):103104.
34. Jordehi AR. Parameter estimation of solar photovoltaic (PV) cells: A review. *Renewable and Sustainable Energy Reviews*. 2016 Aug 1;61:354-71.
35. Suresh MS. Measurement of solar cell parameters using impedance spectroscopy. *Solar Energy Materials and Solar Cells*. 1996 Aug 15;43(1):21-8.
36. González-Pedro V, Xu X, Mora-Sero I, Bisquert J. Modeling high-efficiency quantum dot sensitized solar cells. *ACS nano*. 2010 Oct 26;4(10):5783-90.
37. Deshmukh MP, Kumar RA, Nagaraju J. Measurement of solar cell ac parameters using the time domain technique. *Review of scientific instruments*. 2004 Aug 13;75(8):2732-5.
38. Mandal H, Nagaraju J. GaAs/Ge and silicon solar cell capacitance measurement using triangular wave method. *Solar energy materials and solar cells*. 2007 May 4;91(8):696-700.

39. Cotfas DT, Cotfas PA, Kaplanis S. Methods and techniques to determine the dynamic parameters of solar cells. *Renewable and Sustainable Energy Reviews*. 2016 Aug 1;61:213-21.
40. Ramadan R, Martín-Palma RJ. Electrical characterization of MIS Schottky barrier diodes based on nanostructured porous silicon and silver nanoparticles with applications in solar cells. *Energies*. 2020 Jan;13(9):2165.
41. Han Y, Méès L, Gouesbet G, Wu Z, Gréhan G. Resonant spectra of a deformed spherical microcavity. *JOSA B*. 2006 Jul 1;23(7):1390-7.
42. Aktas O, Ozgur E, Tobail O, Kanik M, Huseyinoglu E, Bayindir M. A new route for fabricating on-chip chalcogenide microcavity resonator arrays. *Advanced Optical Materials*. 2014 Jul;2(7):618-25.
43. Kippenberg TJ, Spillane SM, Vahala KJ. Kerr-nonlinearity optical parametric oscillation in an ultrahigh- Q toroid microcavity. *Physical review letters*. 2004 Aug 19;93(8):083904.
44. Kippenberg TJ, Spillane SM, Min B, Vahala KJ. Theoretical and experimental study of stimulated and cascaded Raman scattering in ultrahigh- Q optical microcavities. *IEEE Journal of selected topics in Quantum Electronics*. 2004 Dec 13;10(5):1219-28.
45. Kippenberg TJ, Spillane SM, Armani DK, Vahala KJ. Fabrication and coupling to planar high- Q silica disk microcavities. *Applied Physics Letters*. 2003 Jul 28;83(4):797-9.
46. Huang GS, Kiravittaya S, Bolaños Quiñones VA, Ding F, Benyoucef M, Rastelli A, et al. Schmidt OG. Optical properties of rolled-up tubular microcavities from shaped nanomembranes. *Applied Physics Letters*. 2009 Apr 6;94(14):141901.
47. Kipp T, Welsch H, Strelow C, Heyn C, Heitmann D. Optical modes in semiconductor microtube ring resonators. *Physical review letters*. 2006 Feb 24;96(7):077403.

48. Wang Y, Wang Y, Huang G, Kong Y, Liu C, Zhao Z, et al. Single whispering gallery mode in mesh-structured tubular microcavity with tunable axial confinement. *Advanced Photonics Research*. 2021 May;2(5):2000163.
49. Ding M, Senthil Murugan G, Brambilla G, Zervas MN. Whispering gallery mode selection in optical bottle microresonators. *Applied Physics Letters*. 2012 Feb 20;100(8):081108.
50. Sumetsky M. Optical bottle versus acoustic bottle and antibottle resonators. *Optics letters*. 2017 Mar 1;42(5):923-6.
51. Sumetsky M, Dulashko Y, Windeler RS. Super free spectral range tunable optical microbubble resonator. *Optics letters*. 2010 Jun 1;35(11):1866-8.
52. Sumetsky M. Optical bottle microresonators. *Progress in Quantum Electronics*. 2019 Mar 1;64:1-30.
53. Ward JM, O'Shea DG, Shortt BJ, Morrissey MJ, Deasy K, Nic Chormaic SG. Heat-and-pull rig for fiber taper fabrication. *Review of scientific instruments*. 2006 Aug 18;77(8):083105.
54. Kim K, Yoon S, Seo M, Lee S, Cho H, Meyyappan M, et al. Whispering gallery modes enhance the near-infrared photoresponse of hourglass-shaped silicon nanowire photodiodes. *Nature Electronics*. 2019 Dec;2(12):572-9.
55. Seo M, Yoon S, Cho H, Lee S, Kim K, Kong BD, et al. Solar cell using hourglass-shaped silicon nanowires for increased light-trapping path. *IEEE Journal of Photovoltaics*. 2020 Jan 21;10(2):475-9.
56. Rastelli A, Kiravittaya S, Wang L, Bauer C, Schmidt OG. Micro-photoluminescence spectroscopy of hierarchically self-assembled quantum dots. *Physica E: Low-dimensional Systems and Nanostructures*. 2006 May 1;32(1-2):29-32.
57. Songmuang R, Rastelli A, Mendach S, Schmidt OG. SiO_x/Si radial superlattices and microtube optical ring resonators. *Applied Physics Letters*. 2007 Feb 26;90(9):091905.

58. Chevuntulak C, Rakpaises T, Sridumrongsak N, Thainoi S, Kiravittaya S, Nuntawong N, et al. Molecular beam epitaxial growth of interdigitated quantum dots for heterojunction solar cells. *Journal of Crystal Growth*. 2019 Apr 15;512:159-63.
59. Chin VJ, Salam Z, Ishaque K. Cell modelling and model parameters estimation techniques for photovoltaic simulator application: A review. *Applied Energy*. 2015 Sep 15;154:500-19.
60. Rhouma MB, Gastli A, Brahim LB, Touati F, Benammar M. A simple method for extracting the parameters of the PV cell single-diode model. *Renewable Energy*. 2017 Dec 1;113:885-94.
61. Jain A, Kapoor A. Exact analytical solutions of the parameters of real solar cells using Lambert W-function. *Solar Energy Materials and Solar Cells*. 2004 Feb 6;81(2):269-77.
62. Sriphan S, Kiravittaya S, Thainoi S, Panyakaew S. Effects of temperature on I-V characteristics of InAs/GaAs quantum-dot solar cells. In *Advanced Materials Research 2015* (Vol. 1103, pp. 129-135).
63. Prasatsap U, Kiravittaya S, Rakpaises T, Sridumrongsak N, Tандаеchanurat A, Yordsri V, et al. Equivalent circuit parameters of hybrid quantum-dot solar cells. *Materials Today: Proceedings*. 2020 Jan 1;23:767-76.
64. Prasatsap U, Kiravittaya S, Thainoi S, Panyakeow S. DC and AC Circuit Parameters of Hybrid InAs/GaAs and GaSb/GaAs Quantum-Dot Solar Cells. *Naresuan University Journal: Science and Technology (NUJST)*. 2020 Aug 18;29(1):111-20.
65. The MathWorks, Inc. lsqcurvefit [Internet]. United States; [cited 2019 February 9], Available from <https://www.mathworks.com/help/optim/ug/lsqcurvefit.html>
66. Lăzureanu C. Spirals on surfaces of revolution. *VisMath*. 2014;16(2):1-10.
67. Nanoscribe GmbH. [Internet]. Photonic Professional (GT). User Manual; 2014 Nanoscribe GmbH [cited 2019 May 23]. <http://cense.engr.uky.edu/sites/cense/files/UserManual.pdf>

68. Nanoscribe GmbH and Co. KG. Company. Nanoscribe acellink company [Internet]. Germany; [cited 2019 July 14], Available from <https://www.nanoscribe.com/en/>
69. Nanoscribe GmbH. NanoGuid [Internet]. Germany; [cited 2019 September 30], Available from <https://support.nanoscribe.com/hc/en-gb>
70. Taflove A, Hagness S.C. Computational electrodynamics: The finite-difference time-domain method. Norwood: Artech; 2005.
71. Oskooi AF, Roundy D, Ibanescu M, Bermel P, Joannopoulos JD, Johnson SG. MEEP: A flexible free-software package for electromagnetic simulations by the FDTD method. *Computer Physics Communications*. 2010 Mar 1;181(3):687-702.
72. Joannopoulos JD, Johnson SG, Winn JN, Meade RD. Photonic crystals: Molding the flow of light. 2nd ed. United states: Princeton university press; 2008.
73. Tian Z, Li S, Kiravittaya S, Xu B, Tang S, Zhen H, Lu W, Mei Y. Selected and enhanced single whispering-gallery mode emission from a mesostructured nanomembrane microcavity. *Nano letters*. 2018 Nov 14;18(12):8035-40.
74. Hosoda M, Shigaki T. Degeneracy breaking of optical resonance modes in rolled-up spiral microtubes. *Applied physics letters*. 2007 Apr 30;90(18):181107.
75. Pierret RF, *Semiconductor Device Fundamentals*. 2nd ed. Addison-Wesley; 1996.
76. Xu Y, Lee RK, Yariv A. Finite-difference time-domain analysis of spontaneous emission in a microdisk cavity. *Physical Review A*. 2000 Feb 14;61(3):033808.
77. Kogelnik H, Shank CV. Coupled-wave theory of distributed feedback lasers. *Journal of applied physics*. 1972 May;43(5):2327-35.
78. Wikipedia. Blueshift [Internet]. Florida; [cited 2020 January 4, 2020], Available from <https://en.wikipedia.org/wiki/Blueshift>
79. Griffiths DJ. *Introduction to quantum mechanics*. 2nd ed. Essex: Pearson; 2014

BIOGRAPHY

Name-Surname	Unchittha Prasatsap
Date of Birth	23 May 1991
Address	12/21 Surasee road , Tambon Nai Muang, Amphoe Muang, Phitsanulok Province 65000, Thailand
Current Workplace	Naresuan University
Current Position	Ph.D. student
Work Experience	2013, Electrical Engineer at Precise System and Project Co. Ltd
Education Background	2013, B.Eng. (Electrical Engineering, first class honor) Naresuan University, Thailand 2017, M.Eng. (Electrical Engineering) Naresuan University, Thailand
Publication	Journal Articles 1. Prasatsap U, Kiravittaya S, Rakpaiset T, Sridumrongsak N, Tандачанурат А, Yordsri V, Thanachayanont C, Chevintulak C, Thainoi S, Panyakeow S. Equivalent circuit parameters of hybrid quantum-dot solar cells. <i>Materials Today: Proceedings</i> . 2020 Jan 1;23:767-76. 2. Prasatsap U, Kiravittaya S, Thainoi S, Panyakeow S. DC and AC Circuit Parameters of Hybrid InAs/GaAs and GaSb/GaAs Quantum-Dot Solar Cells. <i>Naresuan University Journal: Science and Technology (NUJST)</i> . 2020 Aug 18;29(1):111-20. 3. Prasatsap U, Kiravittaya S, Prasertpalichat S, Thornyanadacha N, Thainoi S, Panyakeow S. Light-induced circuit parameter variation in self-assembled quantum-dot photovoltaic cell. <i>Materials Today: Proceedings</i> . 2021 Mar 30. In Press. 4. Prasatsap U, Kiravittaya S. Numerical simulations of single whispering-gallery mode enhancement in hollow cylindrical optical microcavity. <i>Songklanakarin Journal of Science and Technology</i> . Accepted. 5. Zon, Korkerdsantisuk T, Sangpho A, Thainoi S, Prasatsap U, Kiravittaya S, Thornyanadacha N, Tандачанурат А, Nuntawong N, Sopitpan S, Yordsri V, Thanachayanont C. Investigation of hybrid InSb and GaSb quantum nanostructures. <i>Microelectronic Engineering</i> . 2021 Jan 15;237:111494. 6. Prasatsap U, Mayteevarunyoo T, Malomed BA. Three-wave truncated Airy waves and solitons in two dimensions. In draft.

Conference Proceedings

1. Prasatsap U, Kiravittaya S. Important parameters estimation of semiconductor solar cells. The 14th Naresuan University National Research Conference; 2018 Nov 1; Phitsanulok. Thailand; 2018.
2. Prasatsap U, Kiravittaya S, Rakpaises T, Sridumrongsak N, Tandaechanurat A, Yordsri V et al. Equivalent circuit parameters of hybrid quantum-dot solar cells. The 6th Thailand International Nanotechnology Conference. Pathum Thani. Thailand; 2018.
3. Prasatsap U, Kiravittaya S, Thainoi S, Panyakeow S. DC and AC circuit parameters of hybrid InAs/GaAs and GaSb/GaAs quantum-dot solar cells program. The 2nd Materials Research Society of Thailand International Conference. Pattaya. Thailand; 2019.

